Alma Mater Studiorum · University of Bologna

School of Science
Department of Physics and Astronomy
Master's Degree in Physics

Development of a Frequency Mixing Protocol on a Short-Wave Infrared Multiphoton Microscope

Supervisor:
Prof. Francesco Minardi

Co-supervisor:
Prof. Luigi Bonacina

Candidate:
Riccardo Fabbri

Academic Year 2024/2025

Abstract

This thesis presents the implementation and first testing of a frequency-mixing acquisition scheme in a short-wave infrared multiphoton microscope. The project aims to extend conventional harmonic imaging with additional signals produced by nonlinear mixing between two synchronized excitation beams, improving the optical selectivity in complex samples. After the installation of the new components, the characterization of the system and measurements on representative test samples confirmed that the upgraded microscope can generate and detect mixing signals alongside standard harmonics. The new signals will permit the extraction of more information from the samples, allowing one to differentiate between structures that normally would have produced indistinguishable responses.

Contents

Introduction

The discovery and subsequent control of nonlinear optical phenomena have profoundly shaped many areas of applied physics. In microscopy, more specifically, the deliberate use of nonlinear light–matter interactions enabled the emergence of many multiphoton techniques, in which signals arise predominantly from the high-intensity focal volume. This intrinsic spatial confinement provides strong optical sectioning and improved background rejection without the need for a confocal pinhole, while also introducing a degree of intrinsic structure selectivity in complex samples. As a result, multiphoton microscopy has become a central platform in modern high-resolution, high-selectivity optical imaging and remains at the frontier of ongoing advances in contemporary microscopy.

This Master's thesis presents the work carried out over a six month period in the laboratory of the Department of Applied Physics of the University of Geneva. The laboratory's research focuses primarily on the development of next-generation multiphoton microscopes for biological and biomedical applications, with the objective of improving the speed, resolution and overall capabilities of these imaging systems. To do so, it hosts several research and prototype microscopy platforms that are continuously improved and upgraded in order to push the limits of modern multiphoton techniques.

The specific objective of this thesis project was to develop a frequency mixing protocol and to implement it on one of the multiphoton microscopes present in the laboratory. This required several steps. First, a delay line, necessary to permit the interaction between the frequency components, was designed and integrated into the existing system. Subsequently, the modified system was characterized at its new operating frequencies and with the upgraded optical components. In addition, a new detection module was designed and constructed to integrate with the existing platform. This module incorporates a tunable monochromator, thereby enabling the detection of the wide range of

signals generated by frequency-mixing processes.

Finally, the upgraded system was evaluated using various samples available in the laboratory, demonstrating the proper functioning of the newly developed acquisition protocol. However, due to the limited range of samples available during the project and to the time constraints of this thesis, it was not possible to develop and test a complete analysis protocol for the new signals introduced. This task is therefore proposed as the main direction for future work.

This thesis opens with a theoretical overview of nonlinear optics, with particular attention on its application to microscopy. The first chapter provides a general introduction to the fundamental principles and derivations underlying nonlinear optical phenomena, loosely following the exposition presented by Robert W. Boyd in the book *Nonlinear Optics* [1]. The second chapter then offers an extensive description of the principal parametric nonlinear processes employed for imaging, namely harmonic generation and frequency mixing, and highlights their distinguishing features with respect to other nonparametric nonlinear effects.

In the third chapter, the complete microscopy setup used in this work is described in detail, including its characterization, together with an in-depth presentation of the modifications developed and implemented during the course of the project. Finally, the fourth chapter reports and discusses images acquired using the newly implemented frequency-mixing capability of the system and introduces a novel data-analysis methodology that can be used to exploit the obtained additional signals to further enhance the overall selectivity of the microscope.

In writing this thesis, generative artificial intelligence tools (OpenAI, *ChatGPT* version 5.2, 2025) were occasionally used for text review and optimization to improve its clarity and coherence.

1. Fundamentals of Nonlinear Optics

Nonlinear optics studies the response of material systems to intense laser light. Indeed, at sufficiently high optical intensities the response of many media becomes nonlinear, giving rise to a variety of phenomena and enabling the production of new radiation components oscillating at frequencies non present in the original optical stimulus.

This first chapter will focus on expressing the nonlinear optical response of a material in terms of its optical susceptibility and on deriving said susceptibility, particularly its nonlinear contributions, at both the macroscopic and microscopic levels, starting from the atomic-scale charges behavior. In addition, it will describe how the various radiative components of the total field become coupled to one another through nonlinear effects. These phenomena will first be studied for the case of unfocused light, and then the additional effects introduced by the presence of a focal point, as is typical in microscopy applications, will be examined.

1.1 Nonlinear Optical Response

It is convenient to express the response of a system to an incident electromagnetic field as the polarization P of that system with respect to the intensity of the field. In conventional *linear* optics, this dependence is linear

$$\mathbf{P}(t) = \epsilon_0 \chi \mathbf{E}(t) \tag{1.1}$$

where ϵ_0 is the free space permittivity and χ is a second-rank tensor known as the optical susceptibility, which acts as a proportionality constant between stimulus and material response.

In *nonlinear* optics, the light is intense enough to introduce nonlinearity in

the material response; the polarization can thus be expressed as a power series:

$$\mathbf{P}(t) = \epsilon_0[\chi^{(1)}\mathbf{E}(t) + \chi^{(2)}\mathbf{E}^2(t) + \chi^{(3)}\mathbf{E}^3(t) + \dots] \tag{1.2}$$

$$\equiv \mathbf{P}^{(1)}(t) + \mathbf{P}^{(2)}(t) + \mathbf{P}^{(3)}(t) + \dots \tag{1.3}$$

where $\chi^{(1)}$, $\chi^{(2)}$, $\chi^{(3)}$ are the linear and the second- and third order nonlinear susceptibilities, respectively, second-, third- and fourth-rank tensors [1]. These tensors decrease dramatically as their order increases, meaning that high-order nonlinear processes are quite weak and require high intensity lasers to be detectable [2].

The assumption that the material responds instantaneously to the field leads to a polarization that depends only on the instantaneous value of the field intensity and to a susceptibility that behaves as a constant. Due to the Kramers-Kronig relations, this assumption is equivalent to a lossless and dispersionless medium [3].

Considering instead the more general case of a material with both dispersion and absorption, the nonlinear susceptibility becomes a complex quantity that depends on the frequency of the applied field and that relates the complex amplitude of the polarization to that of the field itself. A substantial portion of the studies of nonlinear optics are concerned with deriving the various components of the nonlinear susceptibility tensor, which enable quantitative predictions of the optical response of a given system.

To obtain a first formal definition of nonlinear susceptibility, the electric field vector of the incident optical wave is expressed as a sum over a discrete number of frequency components ω_n

$$\mathbf{E}(\mathbf{r}, t) = \sum_n \mathbf{E}_{\omega_n}(\mathbf{r}) e^{-i(w_n t)} \tag{1.4}$$

where

$$\mathbf{E}_{\omega_n}(\mathbf{r}) = \mathbf{A}_{\omega_n} e^{i(\mathbf{k}_n \cdot \mathbf{r})} \tag{1.5}$$

and $\mathbf{A}_{\omega_n}$ represents the vectorial spatial field amplitude of the component oscillating at frequency ω_n. It can be noted that in Eq. 1.4 it is not necessary to explicitly include the complex-conjugate factors, because the summation

extends over both positive and negative frequencies and the relation $\mathbf{E}_{-\omega_n} = \mathbf{E}^*_{\omega_n}$ holds.

Using the same notation, the nonlinear polarization is expressed as

$$\mathbf{P}^{(2)}(\mathbf{r}, t) = \sum_n \mathbf{P}^{(2)}_{\omega_n} e^{-i(w_n t)} \tag{1.6}$$

In treating the second-order nonlinear effects, it is convenient to consider the simplest form of the electric field vector which still allows for such behaviors, meaning a field composed of just two components oscillating at frequencies ω_n and ω_m. We can then define the components of the second-order nonlinear susceptibility tensor as a constant of proportionality between the nonlinear polarization and the product of the field amplitudes [1]

$$P^{(2)}_{\omega_n+\omega_m,i} = \epsilon_0 \sum_{jk} \sum_{(nm)} \chi^{(2)}_{ijk}(\omega_n + \omega_m; \omega_n, \omega_m) E_{\omega_n,j} E_{\omega_m,k} \tag{1.7}$$

where the indices ijk reflect the Cartesian components of the fields, and the notation (nm) indicates that the sum $\omega_n + \omega_m$ must be fixed while performing the summation over ω_n and ω_m. The notation $\chi^{(2)}_{ijk}(\omega_n + \omega_m; \omega_n, \omega_m)$ for the susceptibility components explicitly emphasizes their dependence on frequency, with the semicolon indicating that the first argument, which corresponds to the generated output frequency, is functionally determined by the last two, which represent the input frequencies.

It can be seen from Eqs. 1.4 and 1.7 that since the amplitudes $\mathbf{E}_{\omega_n}$ and $\mathbf{E}_{\omega_m}$ are associated with the factors $e^{-i(\omega_n t)}$ and $e^{-i(\omega_m t)}$, respectively, their product has a time dependency $e^{-i(\omega_n+\omega_m)t}$, so the factor $\mathbf{E}_{\omega_n}\mathbf{E}_{\omega_m}$ in Eq. 1.7 introduces a contribution to the total nonlinear polarization at a frequency $\omega_n + \omega_m$, following the expression in Eq. 1.6.

The summation $\sum_{(nm)}$ over the field frequencies in Eq. 1.7 must be evaluated to obtain the final result. However, before continuing with the general case, it is insightful to consider two simpler examples that are among the most relevant nonlinear second-order phenomena for applied microscopy.

Sum-frequency generation

The input field frequencies are set to ω_1 and ω_2, and the third generated frequency becomes $\omega_3 = \omega_1 + \omega_2$. In this case, the summation over the frequencies in Eq. 1.7 gives

$$P^{(2)}_{\omega_3,i} = \epsilon_0 \sum_{jk} \left[\chi^{(2)}_{ijk}(\omega_3; \omega_1, \omega_2) E_{\omega_1,j} E_{\omega_2,k} + \chi^{(2)}_{ijk}(\omega_3; \omega_2, \omega_1) E_{\omega_2,j} E_{\omega_1,k} \right] \quad (1.8)$$

It can be demonstrated [1] that the nonlinear susceptibility possesses intrinsic permutation symmetry, as

$$\chi^{(2)}_{ijk}(\omega_n + \omega_m; \omega_n, \omega_m) = \chi^{(2)}_{ikj}(\omega_n + \omega_m; \omega_m, \omega_n) \quad (1.9)$$

and the indices j and k of the field amplitude can be swapped without affecting the physical description, so Eq. 1.8 reduces to

$$P^{(2)}_{\omega_3,i} = 2\epsilon_0 \sum_{jk} \chi^{(2)}_{ijk}(\omega_3; \omega_1, \omega_2) E_{\omega_1,j} E_{\omega_2,k} \quad (1.10)$$

Second-harmonic generation

Only one input frequency ω_1 is considered and the generated frequency is $\omega_3 = 2\omega_1$. Performing the summation again over the frequencies in Eq. 1.7 gives

$$P^{(2)}_{\omega_3,i} = \epsilon_0 \sum_{jk} \chi^{(2)}_{ijk}(\omega_3; \omega_1, \omega_1) E_{\omega_1,j} E_{\omega_1,k} \quad (1.11)$$

if second-harmonic generation is interpreted as a degenerate case of sum-frequency generation, the absence in this expression of the factor 2 present in Eq. 1.10 may appear counterintuitive. In reality, the two expressions in Eqs. 1.10 and 1.11 remain distinct even as ω_2 approaches ω_1. This behavior is justified by the fact that the nonlinear polarization produced by two distinct fields is expected to be larger than that produced by a single field, because the total light intensity is higher in the first case [1].

In general, the summation $\sum_{(nm)}$ over the field frequencies in Eq. 1.7 can

be evaluated to obtain a result of the form

$$P^{(2)}_{\omega_n+\omega_m,i} = \epsilon_0 D \sum_{jk} \chi^{(2)}_{ijk}(\omega_n + \omega_m; \omega_n, \omega_m) E_{\omega_n,j} E_{\omega_m,k} \tag{1.12}$$

where D is a degeneracy factor equal to the number of distinct permutations of the input field frequencies components.

The same reasoning can be applied to third-order (or any higher-order) effects. For convenience, a field with just three components at frequencies ω_n, ω_m and ω_o is considered and the components of the third-order nonlinear susceptibility are defined as the constants of proportionality between the nonlinear polarization and field amplitudes

$$P^{(3)}_{\omega_n+\omega_m+\omega_o,i} = \epsilon_0 \sum_{jkl} \sum_{(nmo)} \chi^{(3)}_{ijkl}(\omega_n+\omega_m+\omega_o; \omega_n, \omega_m, \omega_o) E_{\omega_n,j} E_{\omega_m,k} E_{\omega_o,l} \tag{1.13}$$

and again the summation over the frequencies can be evaluated to obtain the expression

$$P^{(3)}_{\omega_n+\omega_m+\omega_o,i} = \epsilon_0 D \sum_{jkl} \chi^{(3)}_{ijkl}(\omega_n + \omega_m + \omega_o; \omega_n, \omega_m, \omega_o) E_{\omega_n,j} E_{\omega_m,k} E_{\omega_o,l} \tag{1.14}$$

where, this time, the degeneracy factor D represents the number of distinct permutations of the field frequencies ω_n, ω_m and ω_o.

1.2 Time-Domain Derivation of Optical Susceptibility

Until now, we have described nonlinear polarization as a discrete summation of frequency components and defined nonlinear susceptibility by relating the frequency components $\mathbf{P}_\omega$ of the nonlinear polarization to those $\mathbf{E}_{\omega'}$ of the applied field. However, it is also possible to make the derivation in the time-domain by directly considering the polarization $\mathbf{P}(t)$ that is produced by the applied field $\mathbf{E}(t)$ [1].

For a material that has a purely linear response, the induced polarization

can be expressed as

$$\mathbf{P}^{(1)}(t) = \epsilon_0 \int_0^\infty R^{(1)}(\tau)\mathbf{E}(t-\tau)d\tau \tag{1.15}$$

where $R^{(1)}(\tau)$ is the linear response function that relates the polarization at time t to the electric field at an earlier time $t-\tau$. Thus, the total polarization is obtained by integrating over all previous times.

The Fourier transforms of the field intensity are of the form

$$\mathbf{E}(\omega) = \int_{-\infty}^\infty \mathbf{E}(t)e^{i(\omega t)}dt \tag{1.16}$$

$$\mathbf{E}(t) = \frac{1}{2\pi}\int_{-\infty}^\infty \mathbf{E}(\omega)e^{-i(\omega t)}d\omega \tag{1.17}$$

where $\mathbf{E}(\omega)$ is equivalent to the notation $\mathbf{E}_\omega$ used before. Substituting the term $\mathbf{E}(t-\tau)$ in Eq. 1.15 with its Fourier transform gives

$$\mathbf{P}^{(1)}(t) = \epsilon_0 \int_0^\infty \left[\int_{-\infty}^\infty R^{(1)}\mathbf{E}(\omega)e^{-i\omega(t-\tau)}\frac{d\omega}{2\pi}\right] d\tau \tag{1.18}$$

$$= \epsilon_0 \int_{-\infty}^\infty \left[\int_0^\infty R^{(1)}\mathbf{E}(\omega)e^{-i\omega(t-\tau)}d\tau\right]\frac{d\omega}{2\pi} \tag{1.19}$$

The linear susceptibility can now be defined as

$$\chi^{(1)}(\omega;\omega) = \int_0^\infty R^{(1)}(\tau)e^{i(\omega\tau)} \tag{1.20}$$

and Eq. 1.19 reduced to the form

$$\mathbf{P}^{(1)}(t) = \epsilon_0 \int_{-\infty}^\infty \chi^{(1)}(\omega;\omega)\mathbf{E}(\omega)e^{-i(\omega t)}\frac{d\omega}{2\pi} \tag{1.21}$$

which, as done in the previous section, expresses the time-varying polarization in terms of the frequency-dependent susceptibility and the frequency components of the applied field.

The same approach can be used to describe nonlinear responses. In partic-

ular, the second-order nonlinear susceptibility is defined as

$$\chi^{(2)}(\omega_n + \omega_m; \omega_n, \omega_m) = \int_0^\infty \int_0^\infty R^{(2)}(\tau_1, \tau_2) e^{i(\omega_n \tau_1 + \omega_m \tau_2)} d\tau_1 d\tau_2 \tag{1.22}$$

where $R^{(2)}(\tau_1, \tau_2)$ is now the nonlinear response function that relates the polarization at time t to the product of the electric field at time $t - \tau_1$ and $t - \tau_1$. The second-order nonlinear polarization is thus expressed as

$$\mathbf{P}^{(2)}(t) = \epsilon_0 \int_0^\infty \int_0^\infty R^{(2)}(\tau_1, \tau_2) \mathbf{E}(t - \tau_1) \mathbf{E}(t - \tau_2) d\tau_1 d\tau_2 \tag{1.23}$$

$$= \epsilon_0 \int_{-\infty}^\infty \int_{-\infty}^\infty \frac{d\omega_n}{2\pi} \frac{d\omega_m}{2\pi} \int_0^\infty \int_0^\infty d\tau_1 d\tau_2 R^{(2)}(\tau_1, \tau_2) \times \mathbf{E}(\omega_n) e^{-i\omega_n (t - \tau_1)} \mathbf{E}(\omega_m) e^{-i\omega_m (t - \tau_2)} \tag{1.24}$$

$$= \epsilon_0 \int_{-\infty}^\infty \int_{-\infty}^\infty \chi^{(2)}(\omega_n + \omega_m; \omega_n, \omega_m) \mathbf{E}(\omega_n) \mathbf{E}(\omega_m) e^{-i(\omega_n + \omega_m)t} \frac{d\omega_n}{2\pi} \frac{d\omega_m}{2\pi} \tag{1.25}$$

where, as before, the two field intensities were written in the Fourier transform using Eq. 1.17.

The third-order nonlinear response can be represented in a similar manner; setting for convenience $\omega_\sigma = \omega_n + \omega_m + \omega_o$. The third-order nonlinear susceptibility and polarization are

$$\chi^{(3)}(\omega_\sigma; \omega_n, \omega_m, \omega_o) = \int_0^\infty \int_0^\infty \int_0^\infty R^{(3)}(\tau_1, \tau_2, \tau_3) \times e^{i(\omega_n \tau_1 + \omega_m \tau_2 + \omega_o \tau_3)} d\tau_1 d\tau_2 d\tau_3 \tag{1.26}$$

$$\mathbf{P}^{(3)}(t) = \epsilon_0 \int_{-\infty}^\infty \int_{-\infty}^\infty \int_{-\infty}^\infty \chi^{(3)}(\omega_\sigma; \omega_n, \omega_m, \omega_o) \times \mathbf{E}(\omega_n) \mathbf{E}(\omega_m) \mathbf{E}(\omega_o) e^{-i(\omega_\sigma t)} \frac{d\omega_n}{2\pi} \frac{d\omega_m}{2\pi} \frac{d\omega_o}{2\pi} \tag{1.27}$$

where the third-order nonlinear response function behaves analogously as before.

In the previous section, the optical susceptibility components were defined as proportionality constants between the frequency components of, respectively, the polarization and the applied field. Here, specifically in Eqs. 1.20, 1.22, and

1.26, the frequency-dependent susceptibility tensors have been defined directly as the Fourier transform of a time-domain response function of the same order.

1.3 Symmetry of Susceptibility Tensor

The form and symmetries of the susceptibility tensor are constrained by the symmetry properties of the medium itself, which means that the symmetry group of the optical response must contain the point group of the material, a rule known as the Neumann principle [4].

In this account, one symmetry property that is particularly important for microscopy is centrosymmetry, also known as inversion symmetry. This arises from the fact, which will be examined in greater detail in the following section, that the second-order nonlinear susceptibility must identically vanish for centrosymmetric materials.

This statement may seem surprising and a bit extreme, especially because it holds for any medium [1]. In the following section, a formal and extensive description of the phenomenon will be developed. However, for the particular case of a lossless and dispersionless material, it is possible to construct an easy and qualitative proof, useful to get an initial intuition.

From Eq. 1.2 the second-order nonlinear polarization, considering for convenience the scalar form, can be expressed as

$$P^{(2)}(t) = \epsilon_0 \chi^{(2)} E^2(t) \tag{1.28}$$

if the sign of the applied field changes, the sign of the induced polarization must also change, as the assumption was of a medium with inversion symmetry. Therefore, Eq. 1.28 becomes

$$-P^{(2)}(t) = \epsilon_0 \chi^{(2)} [-E(t)]^2 = \epsilon_0 \chi^{(2)} E^2(t) \tag{1.29}$$

Comparing Eqs. 1.28 and 1.29 gives $P(t) = -P(t)$, so the polarization must vanish identically. This can be the case only if

$$\chi^{(2)} = 0 \tag{1.30}$$

The same result holds for every even-order susceptibility component, which means that a centrosymmetric material can only have odd-order nonlinear effects [1].

This result suggests that second- and third-order nonlinear optical processes, even if superficially similar, are, in fact, intrinsically distinct and tend to arise from different classes of physical systems. In the context of microscopy, these distinctions can be exploited to selectively probe specific characteristics of the system. The microscopic applications of second- and third-order nonlinear processes will be discussed in detail in the following sections.

1.4 Optical Susceptibility from Atomic Model

Up to this point, the optical response has been described at a macroscopic level, in terms of the total polarization induced in a material by an applied electromagnetic field. However, in order to analyze in greater detail the differences between the optical behavior of centrosymmetric and non-centrosymmetric media, it is advantageous to adopt a microscopic description of the optical phenomena, modeled at the atomic scale and based on the response of the individual charges within the material, with the aim of expressing the susceptibility via these contributions.

The Lorentz oscillator model describes bound charges, such as electrons in each atom, as harmonic oscillators and traditionally gives good results in describing linear optical properties [1]. The same model can be extended to nonlinear responses by allowing nonlinearities in the restoring force that acts on the electrons.

Being a classical model, it considers only one resonating frequency for each charge, in contrast to quantum mechanical theory that allows multiple energy eigenvalues and thus multiple resonating frequencies. Nevertheless, it remains reliable in cases where the optical frequencies are small compared to the lowest electron resonance frequency in the material [1].

In the following, the case of a non-centrosymmetric material will be addressed first, and subsequently that of a centrosymmetric material, to show how the symmetry properties of the medium affect the derivation.

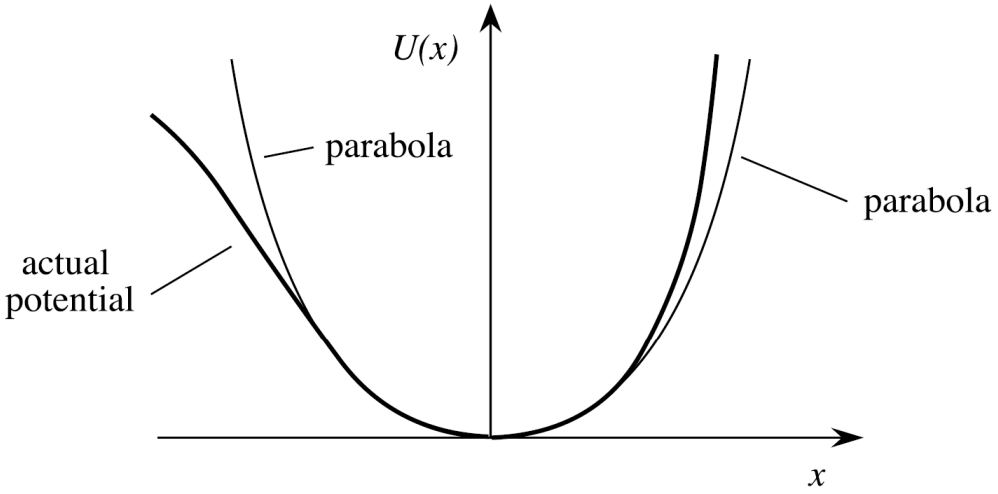

Figure 1: Potential energy function for a non-centrosymmetric medium. [1]

1.4.1 Non-centrosymmetric Media

A bound charge in an electric field feels a restoring force dependent on the displacement x from its equilibrium position caused by the field. Unlike the standard Lorentz model, the restoring force chosen has a nonlinear dependence of the form

$$F_R(x) = -m\omega_0^2 x - max^2 \tag{1.31}$$

where a is a parameter that characterized the strength of nonlinearity. The corresponding potential energy is

$$U(x) = -\int F_R(x)dx = \frac{1}{2}m\omega_0^2 x^2 + \frac{1}{3}max^3 \tag{1.32}$$

where the first term corresponds to an harmonic potential and the second to an anharmonic correction term. The form of the potential energy function is shown in Fig. 1 As the potential energy contains both even and odd powers, it can describe only a non-centrosymmetric medium, as in the presence of inversion symmetry $U(x) = U(-x)$ must hold.

The equation of motion of an electron with displacement x, considering a

scalar field for convenience, takes the form

$$\ddot{x} + 2\gamma\dot{x} + \omega_0^2 x + ax^2 = -\frac{e}{m}E(t) \tag{1.33}$$

The applied field is assumed to be of the form

$$E(t) = E_{\omega_1}e^{-i(\omega_1 t)} + E_{\omega_2}e^{-i(\omega_2 t)} + c.c. \tag{1.34}$$

because having two distinct frequency components is the most general case that allows for second-order interactions between the field and the material.

In the case of a weak applied field the nonlinear term ax^2 will be much smaller than the linear term $\omega_0^2 x$ for any displacement introduced by the field, and Eq. 1.33 can be solved by employing the perturbation expansion method, where $E(t)$ is replaced with $\lambda E(t)$ and λ is a parameter between zero and one that expresses the strength of the interaction, that will eventually be set to unity. The solution is in the form of a power series expansion in λ such as

$$x = \lambda x^{(1)} + \lambda^2 x^{(2)} + \lambda^3 x^{(3)} + \cdots \tag{1.35}$$

Substituting this into 1.33, each term that is proportional to λ, λ^2, λ^3, etc., must satisfy the equation independently, leading to the equations

$$\ddot{x}^{(1)} + 2\gamma\dot{x}^{(1)} + \omega_0^2 x^{(1)} = -\frac{e}{m}E(t) \tag{1.36}$$

$$\ddot{x}^{(2)} + 2\gamma\dot{x}^{(2)} + \omega_0^2 x^{(2)} + a[x^{(1)}]^2 = 0 \tag{1.37}$$

$$\ddot{x}^{(3)} + 2\gamma\dot{x}^{(3)} + \omega_0^2 x^{(3)} + 2ax^{(1)}x^{(2)} = 0 \tag{1.38}$$

$$\cdots$$

The first-order linear contribution $x^{(1)}$ in Eq. 1.36 follows the same equation as that of the conventional, linear, Lorentz model, and its steady-state solution is given by [1]

$$x^{(1)}(t) = x_{\omega_1}^{(1)}e^{-i(\omega_1 t)} + x_{\omega_2}^{(1)}e^{-i(\omega_2 t)} + c.c. \tag{1.39}$$

where the amplitudes $x^{(1)}_{\omega_j}$ for each frequency have the form

$$x^{(1)}_{\omega_j} = -\frac{e}{m}\frac{E_{\omega_j}}{D(\omega_j)} \tag{1.40}$$

and where it is introduced the complex denominator function

$$D(\omega_j) = \omega_0^2 - \omega_j^2 - 2i\omega_j\gamma \tag{1.41}$$

This expression for $x^{(1)}(t)$ can be substituted into Eq. 1.37 to obtain the first correction term $x^{(2)}$, noting that the presence of the square of $x^{(1)}(t)$ introduces contributions at the frequencies $2\omega_1$, $2\omega_2$, $(\omega_1+\omega_2)$ and $(\omega_1-\omega_2)$. The response amplitudes at each frequency can be determined independently. For example, considering the frequency $2\omega_1$, Eq. 1.37 gives

$$\ddot{x}^{(2)} + 2\gamma\dot{x}^{(2)} + \omega_0^2 x^{(2)} = -a\frac{e^2}{m^2}\frac{E^2_{\omega_1}}{D^2(\omega_1)}e^{-2i(\omega_1 t)} \tag{1.42}$$

where a steady-state solution is needed in the form

$$x^{(2)}(t) = x^{(2)}_{2\omega_1}e^{-2i(\omega_1 t)} \tag{1.43}$$

that substituted into Eq. 1.42 leads to the result

$$x^{(2)}_{2\omega_1} = -a\frac{e^2}{m^2}\frac{E^2_{\omega_1}}{D(2\omega_1)D^2(\omega_1)} \tag{1.44}$$

Following the same approach, the amplitudes of the responses at the other frequencies are found to be

$$x^{(2)}_{2\omega_2} = -a\frac{e^2}{m^2}\frac{E^2_{\omega_2}}{D(2\omega_2)D^2(\omega_2)} \tag{1.45}$$

$$x^{(2)}_{(\omega_1+\omega_2)} = -2a\frac{e^2}{m^2}\frac{E_{\omega_1}E_{\omega_2}}{D(\omega_1+\omega_2)D(\omega_1)D(\omega_2)} \tag{1.46}$$

$$x^{(2)}_{(\omega_1-\omega_2)} = -2a\frac{e^2}{m^2}\frac{E_{\omega_1}E_{-\omega_2}}{D(\omega_1-\omega_2)D(\omega_1)D(-\omega_2)} \tag{1.47}$$

were according to the convention used $E_{-\omega_2} = E^*_{\omega_2}$.

To go from the microscopic back to a macroscopic description, these results can be expressed in terms of the linear susceptibilities $\chi^{(1)}$ and the nonlinear susceptibility $\chi^{(2)}$. As seen before, macroscopically, the linear polarization is linked to the applied field by the linear susceptibility

$$P^{(1)}_{\omega_j} = \epsilon_0 \chi^{(1)}(\omega_j) E_{\omega_j} \tag{1.48}$$

while, microscopically, the linear atomic contribution to the polarization is expressed as

$$P^{(1)}_{\omega_j} = -Nex^{(1)}_{\omega_j} \tag{1.49}$$

where N is the density of atoms.

By comparing Eqs. 1.48 and 1.49, and recalling the expression for the linear amplitude $x^{(1)}_{\omega_j}$ given in Eq. 1.40, the following expression for the linear susceptibility is obtained

$$\chi^{(1)}(\omega_j) = \frac{Ne^2}{\epsilon_0 m D(\omega_j)} = \frac{Ne^2}{\epsilon_0 m(\omega_0^2 - \omega_j^2 - 2i\omega_j\gamma)} \tag{1.50}$$

The nonlinear susceptibility for each frequency is calculated in an analogous manner. For example, the nonlinear susceptibility at frequency $2\omega_1$, which described second-harmonic generation, is defined by the macroscopical relation between polarization and applied field

$$P^{(2)}_{2\omega_1} = \epsilon_0 \chi^{(2)}(2\omega_1; \omega_1, \omega_1) E^2_{\omega_1} \tag{1.51}$$

where $P^{(2)}_{2\omega_1}$ is the amplitude of the component of the nonlinear polarization oscillating at frequency $2\omega_1$, and microscopically it is given by the atomic contribution

$$P^{(2)}_{2\omega_1} = -Nex^{(2)}_{2\omega_1} \tag{1.52}$$

Comparing the two expressions for $P^{(2)}_{2\omega_1}$ and using Eq. 1.44 for the nonlinear

amplitude $x^{(2)}_{2\omega_1}$ at frequency $2\omega_1$ leads to

$$\chi^{(2)}(2\omega_1;\omega_1,\omega_1) = \frac{aNe^3}{\epsilon_0 m^2 D(2\omega_1)D^2(\omega_1)} \tag{1.53}$$

that, recalling the result obtained in Eq. 1.50 for $\chi^{(1)}$, can also be written in terms of the product of linear susceptibilities as

$$\chi^{(2)}(2\omega_1;\omega_1,\omega_1) = \frac{a\epsilon_0^2 m}{N^2 e^3}\chi^{(1)}(2\omega_1)\left[\chi^{(1)}(\omega_1)\right]^2 \tag{1.54}$$

The second-order susceptibility is therefore proportional to the product of three linear susceptibilities evaluated at the frequencies ω_1 and $2\omega_1$. In the case of second-harmonic generation at frequency ω_2, the nonlinear susceptibility can be obtained from the same equations simply by substituting ω_1 with ω_2.

The nonlinear susceptibility for the frequency $(\omega_1+\omega_2)$, which describes the sum-frequency generation process, can be obtained by means of a similar calculation, again starting with the macroscopical and microscopical expressions for the polarization induced at that frequency

$$P^{(2)}_{(\omega_1+\omega_2)} = 2\epsilon_0\chi^{(2)}(\omega_1+\omega_2;\omega_1,\omega_2)E_{\omega_1}E_{\omega_2} \tag{1.55}$$

and

$$P^{(2)}_{(\omega_1+\omega_2)} = -Nex^{(2)}_{(\omega_1+\omega_2)} \tag{1.56}$$

Note that this time the macroscopical expression defining the nonlinear susceptibility, in Eq. 1.55, contains a factor 2 because the two input fields are distinct, as discussed before. By comparison of Eqs. 1.55 and 1.56, the nonlinear susceptibility is seen to be given by

$$\chi^{(2)}(\omega_1+\omega_2;\omega_1,\omega_2) = \frac{aNe^3}{\epsilon_0 m^2 D(\omega_1+\omega_2)D(\omega_1)D(\omega_2)} \tag{1.57}$$

which, again recalling Eq. 1.50, can be expressed in terms of the product of

linear susceptibilities as

$$\chi^{(2)}(\omega_1+\omega_2;\omega_1,\omega_2)=\frac{a\epsilon_0^2 m}{N^2e^3}\chi^{(1)}(\omega_1+\omega_2)\chi^{(1)}(\omega_1)\chi^{(1)}(\omega_2) \tag{1.58}$$

It can be seen by comparison of Eqs. 1.54 and 1.57 that as ω_2 approaches ω_1, $\chi^{(2)}(\omega_1+\omega_2;\omega_1,\omega_2)$ approaches $\chi^{(2)}(2\omega_1;\omega_1,\omega_1)$ [1].

The nonlinear susceptibility for the frequency $(\omega_1-\omega_2)$, associated with the other second-order effect, difference-frequency generation, is derived in a similar way and can be written as

$$\begin{aligned}\chi^{(2)}(\omega_1-\omega_2;\omega_1,-\omega_2)&=\frac{aNe^3}{\epsilon_0 m^2 D(\omega_1-\omega_2)D(\omega_1)D(-\omega_2)}\\&=\frac{a\epsilon_0^2 m}{N^2e^3}\chi^{(1)}(\omega_1-\omega_2)\chi^{(1)}(\omega_1)\chi^{(1)}(-\omega_2)\end{aligned} \tag{1.59}$$

This analysis demonstrates that, for a non-centrosymmetric medium, the lowest-order nonlinear contribution to the polarization is second-order in the amplitude of the applied electric field. This reasoning can be straightforwardly generalized to account for higher-order nonlinearities. In particular, the solution of Eq. 1.38 gives rise to a third-order susceptibility $\chi^{(3)}$, and, more generally, terms proportional to λ^n in the perturbative expansion defined by Eq. 1.35 correspond to a nth-order susceptibility $\chi^{(n)}$.

1.4.2 Centrosymmetric Media

For the case of a centrosymmetric medium, the assumed restoring force is not given by Eq. 1.31 as before, but rather by

$$F_R(x)=-m\omega_0^2 x+mbx^3 \tag{1.60}$$

where b is a parameter that characterizes the strength of the nonlinearity and x is again the displacement of the charge from its equilibrium position. This restoring force corresponds to the potential energy function

$$U(x)=-\int F_R(x)\,dx=\frac{1}{2}m\omega_0^2x^2-\frac{1}{4}mbx^4. \tag{1.61}$$

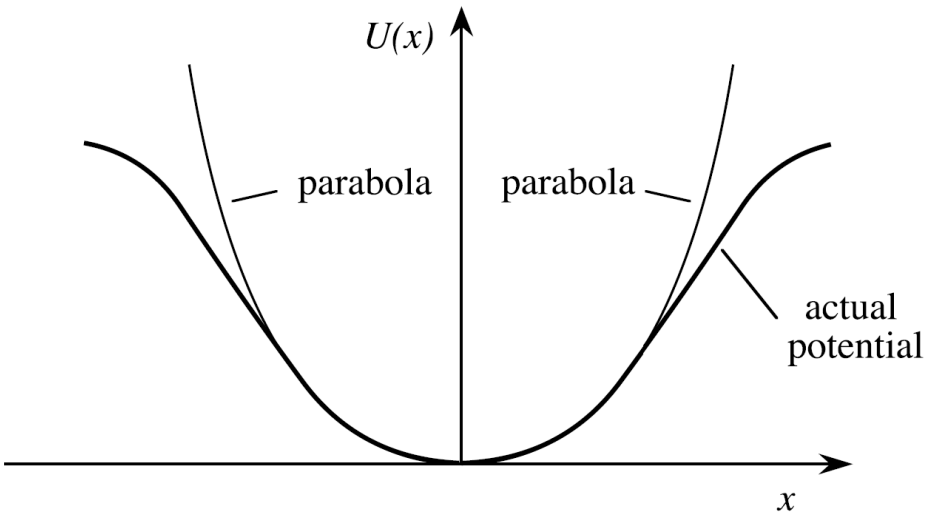

Figure 2: Potential energy function for a centrosymmetric medium. [1]

characterized by a harmonic potential and a correction term that, this time, are both even-order powers of the displacement. This potential function is illustrated in Fig. 2 and is symmetric under inversion $U(x) = U(-x)$, so that it can describe the behavior of a centrosymmetric material.

By employing a derivation analogous to that used for non-centrosymmetric media, it is possible to verify that the lowest-order nonlinear contribution to the polarization arising from the restoring force in Eq. 1.60 is a third-order term in the applied electric field, which can be described by a third-order susceptibility $\chi^{(3)}$. In this analysis, the scalar-field approximation used before is abandoned to explicitly account for the tensorial nature of the susceptibility. Consequently, a full derivation would, in general, require a detailed understanding of the internal symmetries of the material. Therefore, a material that is isotropic as well as centrosymmetric is assumed. Taking into account all these circumstances, the expression for restoring force becomes

$$\mathbf{F}_R(\mathbf{r}) = -m\omega_0^2\mathbf{r} + mb(\mathbf{r}\cdot\mathbf{r})\mathbf{r} \tag{1.62}$$

where the displacement from equilibrium is now represented by the vector

r. Consequently, the second term in the restoring force must have the form shown because it is the only form that is at the same time third-order in the displacement **r** and directed in the **r** direction, which is the only possible direction for an isotropic medium.

The equation of motion for an electron with displacement **r** from equilibrium is thus

$$\ddot{\mathbf{r}} + 2\gamma\dot{\mathbf{r}} + \omega_0^2\mathbf{r} - b(\mathbf{r}\cdot\mathbf{r})\mathbf{r} = -\frac{e}{m}\mathbf{E}(t) \tag{1.63}$$

The most general form for a field that allows for third-order interactions contains three distinct frequency components, so the applied field is taken in the form of

$$\mathbf{E}(t) = \mathbf{E}_{\omega_1}e^{-i(\omega_1 t)} + \mathbf{E}_{\omega_2}e^{-i(\omega_2 t)} + \mathbf{E}_{\omega_3}e^{-i(\omega_3 t)} + c.c. \tag{1.64}$$

$$= \sum_n \mathbf{E}_{\omega_n}e^{-i(\omega_n t)} \tag{1.65}$$

where the summation form is introduced to keep the algebra more readable.

As before, Eq. 1.63 is solved by means of the perturbation expansions method, seeking a solution having the form of a power series in the parameter λ:

$$\mathbf{r}(t) = \lambda\mathbf{r}^{(1)}(t) + \lambda^2\mathbf{r}^{(2)}(t) + \lambda^3\mathbf{r}^{(3)}(t) + \cdots \tag{1.66}$$

Inserting Eq. 1.66 into Eq. 1.63 and requiring that the terms proportional to λ^n satisfy the expression for each value of n lead to the equations

$$\ddot{\mathbf{r}}^{(1)} + 2\gamma\dot{\mathbf{r}}^{(1)} + \omega_0^2\mathbf{r}^{(1)} = -\frac{e}{m}\mathbf{E}(t) \tag{1.67}$$

$$\ddot{\mathbf{r}}^{(2)} + 2\gamma\dot{\mathbf{r}}^{(2)} + \omega_0^2\mathbf{r}^{(2)} = 0 \tag{1.68}$$

$$\ddot{\mathbf{r}}^{(3)} + 2\gamma\dot{\mathbf{r}}^{(3)} + \omega_0^2\mathbf{r}^{(3)} - b(\mathbf{r}^{(1)}\cdot\mathbf{r}^{(1)})\mathbf{r}^{(1)} = 0 \tag{1.69}$$

for $n = 1, 2, 3$, respectively. Eq. 1.67 is simply the vector version of Eq. 1.36 encountered before; its steady-state solution is

$$\mathbf{r}^{(1)}(t) = \sum_n \mathbf{r}^{(1)}_{\omega_n}e^{-i(\omega_n t)} \tag{1.70}$$

where

$$\mathbf{r}_{\omega_n}^{(1)} = -\frac{e}{m}\frac{\mathbf{E}_{\omega_n}}{D(\omega_n)} \tag{1.71}$$

and the denominator function is again $D(\omega_n) = \omega_0^2 - \omega_n^2 - 2i\omega_n\gamma$.

As before, the polarization at frequency ω_n given by the individual contribution of charges is

$$\mathbf{P}_{\omega_n}^{(1)} = -Ne\mathbf{r}_{\omega_n}^{(1)} \tag{1.72}$$

while, macroscopically, the Cartesian components of the polarization can be described using the susceptibility through the relation

$$P_{\omega_n,i}^{(1)} = \epsilon_0 \sum_j \chi_{ij}^{(1)}(\omega_n) E_{\omega_n,j} \tag{1.73}$$

where, due to the assumption of an isotropic medium, the linear susceptibility tensor is diagonal and its components are given by

$$\chi_{ij}^{(1)}(\omega_n) = \chi^{(1)}(\omega_n)\delta_{ij} \tag{1.74}$$

Comparing the two Eqs. 1.72 and 1.73 for the polarization gives the same linear susceptibility already derived in Eq. 1.11 for the non-centrosymmetric case

$$\chi^{(1)}(\omega_n) = \frac{Ne^2}{\epsilon_0 m D(\omega_n)} \tag{1.75}$$

The system's second-order response is governed by Eq. 1.68. Because this equation includes damping but no driving term, its steady-state solution vanishes, that is

$$\mathbf{r}^{(2)} = 0 \tag{1.76}$$

meaning that the system shows no second-order response.

To calculate the third-order response, we substitute the expression for $\mathbf{r}^{(1)}(t)$ given by Eq. 1.70 into Eq. 1.69, which becomes

$$\ddot{\mathbf{r}}^{(3)} + 2\gamma\dot{\mathbf{r}}^{(3)} + \omega_0^2\mathbf{r}^{(3)} = -\frac{be^3}{m^3}\sum_{nmo}\frac{[\mathbf{E}_{\omega_n}\cdot\mathbf{E}_{\omega_m}]\,\mathbf{E}_{\omega_o}}{D(\omega_n)D(\omega_m)D(\omega_o)}e^{-i(\omega_n+\omega_m+\omega_o)t} \tag{1.77}$$

where every one of the indices n, m, o in the summation spans over the three frequencies $\omega_1, \omega_2, \omega_3$ expressed in Eq. 1.64. The summation introduces many different frequencies as parts of the third-order interaction that, for convenience, are expressed as $\omega_\sigma = \omega_n + \omega_m + \omega_o$ for every possible combination of the three fundamental frequencies.

Eq. 1.77 requires a solution in the form

$$\mathbf{r}^{(3)}(t) = \sum_\sigma \mathbf{r}^{(3)}_{\omega_\sigma} e^{-i(\omega_\sigma t)} \tag{1.78}$$

that substituted into the equation itself gives the expression for $\mathbf{r}^{(3)}_{\omega_\sigma}$ as

$$\mathbf{r}^{(3)}_{\omega_\sigma} = -\frac{be^3}{m^3} \sum_{(nmo)} \frac{[\mathbf{E}(\omega_n) \cdot \mathbf{E}(\omega_m)]\, \mathbf{E}(\omega_o)}{D(\omega_\sigma) D(\omega_n) D(\omega_m) D(\omega_o)} \tag{1.79}$$

where (n, m, o) indicates that the summation is to be carried out on the frequencies ω_n, ω_m, and ω_o while keeping ω_σ fixed.

Microscopically, the magnitude of the polarization contribution arising from electrons oscillating at the frequency ω_σ can be expressed as

$$P^{(3)}_{\omega_\sigma} = -Ne\mathbf{r}^{(3)}_{\omega_\sigma} \tag{1.80}$$

while in Eq. 1.13 the third-order nonlinear susceptibility has been defined via its components as

$$P^{(3)}_{\omega_\sigma, i} = \epsilon_0 \sum_{jkl} \sum_{(mno)} \chi^{(3)}_{ijkl}(\omega_\sigma; \omega_n, \omega_m, \omega_o) E_{\omega_n, j} E_{\omega_m, k} E_{\omega_o, l} \tag{1.81}$$

By comparing Eqs. 1.80 and 1.81 the third-order nonlinear susceptibility con be expressed as

$$\chi^{(3)}_{ijkl}(\omega_\sigma; \omega_n, \omega_m, \omega_o) = \frac{bNe^4 \delta_{jk} \delta_{il}}{\epsilon_0 m^3 D(\omega_\sigma) D(\omega_n) D(\omega_m) D(\omega_o)} \tag{1.82}$$

however, because it is arbitrary which field and frequency is labeled as $E_j(\omega_n)$, which as $E_k(\omega_m)$, and which as $E_l(\omega_o)$, there exist multiple expressions for

this susceptibility, equivalent to the one in Eq. 1.82. Specifically, there are six different permutations between the field directions j, k, l and the frequencies $\omega_n, \omega_m, \omega_o$. It is possible to choose a representation of $\chi^{(3)}$ that explicitly exhibits this intrinsic permutation symmetry [1]

$$\chi^{(3)}_{ijkl}(\omega_\sigma; \omega_n, \omega_m, \omega_o) = \frac{bNe^4 \left[\delta_{ij}\delta_{kl} + \delta_{ik}\delta_{jl} + \delta_{il}\delta_{jk}\right]}{3\epsilon_0 m^3 D(\omega_\sigma) D(\omega_n) D(\omega_m) D(\omega_o)} \tag{1.83}$$

As before, this expression can be rewritten in terms of the linear susceptibilities at the four different frequencies $\omega_\sigma, \omega_n, \omega_m$, and ω_o using Eq. 1.75 to eliminate the resonance denominator factors $D(\omega)$

$$\begin{aligned}\chi^{(3)}_{ijkl}(\omega_\sigma; \omega_n, \omega_m, \omega_o) = \frac{bm\epsilon_0^3}{3N^3e^4}\chi^{(1)}(\omega_\sigma)\chi^{(1)}(\omega_n)\chi^{(1)}(\omega_m)\chi^{(1)}(\omega_o) \\ \times \left[\delta_{ij}\delta_{kl} + \delta_{ik}\delta_{jl} + \delta_{il}\delta_{jk}\right]\end{aligned} \tag{1.84}$$

In contrast to the previous case, it has been shown that for a centrosymmetric medium the lowest-order nonlinear contribution to the polarization is third-order in the amplitude of the applied electric field, since the second-order steady state solution vanishes identically in the presence of inversion symmetry, as stated in Eq. 1.76. However, it is important to note that the presence of interfaces and nanoscale defects is often associated with sizable second-order nonlinear effects even in centrosymmetric material. This is due to the fact that surfaces, interfaces, and local defects are indeed spatial regions in which the inversion symmetry is removed [4].

1.5 Nonlinear Optical Interactions as Coupled-Waves

Up to this point, the polarization induced in a system subjected to a strong external electric field has been characterized; noting that, under these conditions, the polarization itself develops new frequency components that are absent in the original field. The significance of this phenomenon lies in the fact that a time-varying polarization can act as a source of new components

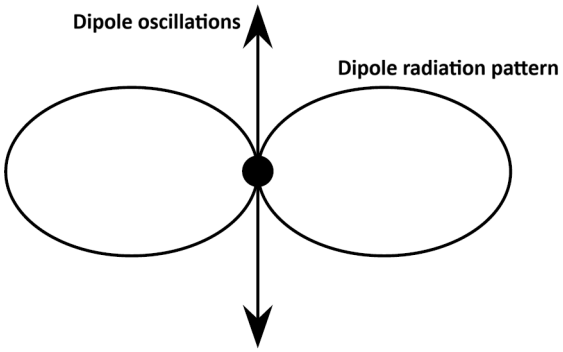

Figure 3: Schematics of the dipole radiation pattern. [1]

of the electromagnetic field, components that oscillate at the new frequencies introduced by the nonlinear response of the system [1]. Even more importantly for microscopy application, the radiation produced in this manner by nonlinear effects is usually highly directional and coherent.

To see why, it is useful to start from a single atom that, under laser light, develops a polarization dipole that oscillates both at the frequency of the external field and, if the field is intense enough, at new frequencies introduced by the nonlinearity. If the atom is isolated, it radiates at these frequencies in both the forward and backward directions, following a dipole radiation pattern schematically depicted in Fig. 3. However, in a material there are millions of atoms with dipoles that oscillate with a phase determined by the incident field. If the phasing of these dipoles is just right, the new field they radiate will interfere constructively in the forward direction and destructively in the backward direction, behaving like the emission of a coherent beam [2]. The phase-matching condition for this to happen will be discussed at the end of this section.

Using wave equations formalism, the generation of these new field components can be described to see how they are coupled by the nonlinear interaction. It is convenient to start from Maxwell's equations in the context of light that propagates through a nonlinear medium, so no free charges and no free

currents are considered

$$\nabla \cdot \mathbf{D} = 0 \tag{1.85}$$

$$\nabla \cdot \mathbf{B} = 0 \tag{1.86}$$

$$\nabla \times \mathbf{E} = -\frac{\partial \mathbf{B}}{\partial t} \tag{1.87}$$

$$\nabla \times \mathbf{H} = \frac{\partial \mathbf{D}}{\partial t} \tag{1.88}$$

the material is assumed nonmagnetic, so

$$\mathbf{B} = \mu_0 \mathbf{H} \tag{1.89}$$

but it is allowed to be nonlinear in the sense that the displacement field $\mathbf{D}$ and the electric field $\mathbf{E}$ follow the relation

$$\mathbf{D} = \epsilon_0 \mathbf{E} + \mathbf{P} \tag{1.90}$$

where the polarization vector $\mathbf{P}$ depends nonlinearly on the local value of the electric field strength $\mathbf{E}$, as discussed in previous sections.

The optical wave equation can be derived in the usual manner; without reporting all the algebra, from Maxwell's equations one obtains

$$\nabla^2 \mathbf{E} - \nabla(\nabla \cdot \mathbf{E}) - \frac{1}{\epsilon_0 c^2} \frac{\partial^2 \mathbf{D}}{\partial t^2} = 0 \tag{1.91}$$

where the term $\nabla(\nabla \cdot \mathbf{E})$ is usually small, especially for the case of a slowly varying electric field's amplitude, so it can be neglected and the wave equation becomes

$$\nabla^2 \mathbf{E} - \frac{1}{\epsilon_0 c^2} \frac{\partial^2 \mathbf{D}}{\partial t^2} = 0 \tag{1.92}$$

It is convenient to split the polarization into its linear and nonlinear parts as

$$\mathbf{P} = \mathbf{P}^{(1)} + \mathbf{P}^{NL} \tag{1.93}$$

where $\mathbf{P}^{(1)}$ is the part of the polarization that depends linearly on the electric

field. Recalling Eq. 1.90, the displacement field $\mathbf{D}$ can be similarly divided into its linear and nonlinear parts as

$$\mathbf{D} = \mathbf{D}^{(1)} + \mathbf{P}^{NL} \tag{1.94}$$

where

$$\mathbf{D}^{(1)} = \epsilon_0 \mathbf{E} + \mathbf{P}^{(1)} \tag{1.95}$$

In terms of these quantities, Eq. 1.92 can be written as

$$\nabla^2 \mathbf{E} - \frac{1}{\epsilon_0 c^2} \frac{\partial^2 \mathbf{D}^{(1)}}{\partial t^2} = \frac{1}{\epsilon_0 c^2} \frac{\partial^2 \mathbf{P}^{NL}}{\partial t^2} \tag{1.96}$$

For the case of a lossless and dispersionless medium, the relation in Eq. 1.95 becomes

$$\mathbf{D}^{(1)} = \epsilon_0 \epsilon^{(1)} \mathbf{E} \tag{1.97}$$

where $\epsilon^{(1)}$ is a frequency-independent dielectric tensor that, in the case of an isotropic medium, becomes a scalar constant. For this simple example, Eq. 1.96 takes the form of a driven wave equation

$$\nabla^2 \mathbf{E} - \frac{\epsilon^{(1)}}{c^2} \frac{\partial^2 \mathbf{E}}{\partial t^2} = \frac{1}{\epsilon_0 c^2} \frac{\partial^2 \mathbf{P}^{NL}}{\partial t^2} \tag{1.98}$$

where the nonlinear response of the medium, that appears on the right-hand side of the expression, acts as a source term . In the absence of this source term, the equation describes free waves propagating with velocity c/n, where n is the linear index of refraction that satisfies $n^2 = \epsilon^{(1)}$.

For the more general case of a dispersive medium, each frequency component of the field must be treated separately. As before, the electric field, the linear displacement field, and the nonlinear polarization are expressed as the sums

of their various frequency components

$$\mathbf{E}(\mathbf{r},t) = \sum_n \mathbf{E}_{\omega_n}(\mathbf{r}) e^{-i(\omega_n t)} \tag{1.99}$$

$$\mathbf{D}^{(1)}(\mathbf{r},t) = \sum_n \mathbf{D}^{(1)}_{\omega_n}(\mathbf{r}) e^{-i(\omega_n t)} \tag{1.100}$$

$$\mathbf{P}^{NL}(\mathbf{r},t) = \sum_n \mathbf{P}^{NL}_{\omega_n}(\mathbf{r}) e^{-i(\omega_n t)} \tag{1.101}$$

where $\mathbf{E}_{\omega_n}, \mathbf{D}^{(1)}_{\omega_n}$ and $\mathbf{P}^{NL}_{\omega_n}$ are complex amplitudes.

In this situation, the dielectric tensor is a complex, frequency-dependent quantity that relates the complex amplitudes of the displacement field to the one of the electric field and Eq. 1.97 becomes

$$\mathbf{D}^{(1)}_{\omega_n}(\mathbf{r}) = \epsilon_0 \epsilon^{(1)}(\omega_n) \mathbf{E}_{\omega_n}(\mathbf{r}) \tag{1.102}$$

An expression of the wave equation, analogous to Eq. 1.98 and valid for each frequency component of the field, is obtained

$$\nabla^2 \mathbf{E}_{\omega_n}(\mathbf{r}) + \frac{\omega_n^2}{c^2} \epsilon^{(1)}(\omega_n) \mathbf{E}_{\omega_n}(\mathbf{r}) = -\frac{\omega_n^2}{\epsilon_0 c^2} \mathbf{P}^{NL}_{\omega_n}(\mathbf{r}) \tag{1.103}$$

This is equivalent to the general wave equation in Eq. 1.92, but expressed with respect to the frequency components.

To show the coupling between the different components of the field, such wave equation can be applied to the already studied case of sum-frequency generation. As before, two components with frequencies ω_1 and ω_2, which generate a third component with frequency $\omega_3 = \omega_1 + \omega_2$ by interacting inside the nonlinear medium, are considered. The fields are treated as scalars for convenience and the waves are set to propagate only along the z-direction.

The wave equation must hold for every frequency component of the field. Considering the one oscillating at frequency ω_3 and ignoring for now the presence of the nonlinear source term, Eq. 1.103 leads to a solution in the form of

a plane wave with the spatial component expressed as [1]

$$E_{\omega_3}(z) = A_{\omega_3} e^{i(k_3 z)} \tag{1.104}$$

where A_{ω_3} is a constant, $k_3 = n_3\omega_3/c$ and $n_3^2 = \epsilon^{(1)}(\omega_3)$, with n_3 refractive index for ω_3 in the material. If the nonlinear source term in the right side of Eq. 1.103 is then reintroduced, this solution remains valid, but the amplitude A_{ω_3} starts to (slowly) varying with respect to the z-direction.

Recalling Eq. 1.10, the nonlinear polarization for the second-order sum-frequency generation can be expressed as

$$P_{\omega_3}^{NL}(z) = 2\epsilon_0 \chi^{(2)}(\omega_3; \omega_1, \omega_2) E_{\omega_1}(z) E_{\omega_2}(z) \tag{1.105}$$

where the summation over the Cartesian components was dropped, as the fields are now considered scalar. The applied field components can be represented for $i = 1, 2$ as

$$E_{\omega_i}(z) = A_{\omega_i} e^{i(k_i z)} \tag{1.106}$$

so Eq. 1.105 becomes

$$P_{\omega_3}^{NL}(z) = 2\epsilon_0 \chi^{(2)}(\omega_3; \omega_1, \omega_2) A_{\omega_1}(z) A_{\omega_2}(z) e^{i(k_1+k_2)z} \tag{1.107}$$

By substituting Eqs. 1.104 and 1.107 into the wave equation in Eq. 1.103 and restricting the derivation to the z-direction, one obtains, after some simplifications, the expression

$$\frac{d^2 A_{\omega_3}}{dz^2} + 2ik_3 \frac{dA_{\omega_3}}{dz} = -\frac{2\chi^{(2)}\omega_3^2}{c^2} A_{\omega_1} A_{\omega_2} e^{i(k_1+k_2-k_3)z} \tag{1.108}$$

where the arguments of the susceptibility are omitted for convenience. Under the slowly varying amplitude approximation it is possible to drop the first term of Eq. 1.108 as it is much smaller than the second [1], so the expression becomes

$$\frac{dA_{\omega_3}}{dz} = i\frac{\chi^{(2)}\omega_3}{n_3 c} A_{\omega_1} A_{\omega_2} e^{i(\Delta k z)} \tag{1.109}$$

where $\Delta k = k_1 + k_2 - k_3$ is defined as the wavevector mismatch.

Eq. 1.109 is known as *coupled-amplitude equation* and expresses how the amplitude of the ω_3 component changes as a consequence of its coupling to the other two components. Repeating the same derivation, it is possible to obtain analogous equations for the other two components

$$\frac{dA_{\omega_1}}{dz} = i\frac{\chi^{(2)}\omega_1}{n_1 c} A_{\omega_3} A_{-\omega_2} e^{-i(\Delta k z)} \tag{1.110}$$

$$\frac{dA_{\omega_2}}{dz} = i\frac{\chi^{(2)}\omega_2}{n_2 c} A_{\omega_3} A_{-\omega_1} e^{-i(\Delta k z)} \tag{1.111}$$

The coupled-amplitude equation in Eq. 1.109 shows that, when $\Delta k = 0$ and under the assumption that A_{ω_1} and A_{ω_2} remain constant, the amplitude A_{ω_3} of the sum-frequency field grows linearly with z. The condition $\Delta k = 0$ is known as *perfect phase matching* and, when met, the generated field maintains a constant phase relation to the nonlinear polarization, leading to maximally efficient energy transfer between the coupled frequency components. On a microscopic level, when $\Delta k = 0$ the individual atomic dipoles are phased so that their radiation is added coherently in the forward direction in the most effective way. When the phase matching condition is not satisfied, the intensity of the emitted radiation is smaller than in the phase matched case [1].

Continuing with the sum-frequencies generation example, it is possible to express the amplitude A_{ω_3} at the exit plane of a nonlinear medium of length L by integrating Eq. 1.109 between $z = 0$ and $z = L$

$$A_{\omega_3}(L) = i\frac{\chi^{(2)}\omega_3}{n_3 c} A_{\omega_1} A_{\omega_2} \int_0^L e^{i\Delta k z} dz = i\frac{\chi^{(2)}\omega_3}{n_3 c} A_{\omega_1} A_{\omega_2} \left(\frac{e^{i\Delta k L} - 1}{i\Delta k} \right) \tag{1.112}$$

Noting that the intensity of a wave is given by

$$I_{\omega_i} = 2 n_i \epsilon_0 c |A_{\omega_i}|^2 \tag{1.113}$$

the intensity of the generated field is given by

$$I_{\omega_3} = \frac{2\epsilon_0 [\chi^{(2)}]^2 \omega_3^2 |A_{\omega_1}|^2 |A_{\omega_2}|^2}{n_3 c} \left| \frac{e^{i\Delta k L} - 1}{\Delta k} \right|^2 \tag{1.114}$$

and with a bit of algebra it can be shown that

$$\left|\frac{e^{i\Delta kL}-1}{\Delta k}\right|^2 = L^2\mathrm{sinc}^2\left(\frac{\Delta kL}{2}\right) \tag{1.115}$$

Taking this into account and using Eq. 1.113 to express the amplitudes as intensities, Eq. 1.114 becomes

$$I_{\omega_3} = \frac{[\chi^{(2)}]^2\omega_3^2 I_1 I_2}{2n_1 n_2 n_3 \epsilon_0 c^3} L^2\mathrm{sinc}^2\left(\frac{\Delta kL}{2}\right) \tag{1.116}$$

The effect of phase matching on the intensity is governed by the factor $\mathrm{sinc}^2(\Delta kL/2)$, which is plotted in Fig. 4. In general, the efficiency of the process decreases sharply as $|\Delta k|L$ increases from zero. This is not surprising because, when L is larger than $\pi/\Delta k$, the generated field has time to go out of phase with the driving polarization and the power can flow back from the ω_3 component to the other two. Consequently, the *coherence length* of the interaction is defined as

$$l_c = \frac{\pi}{\Delta k} \tag{1.117}$$

that is the spatial extent for which the generated radiation remains in phase with the driving polarization.

In most cases, satisfying the phase-matching condition is challenging because many materials exhibit normal dispersion, meaning that the refractive index increases with frequency. As a result, perfect phase matching for collinear beams is generally unattainable, since this would require

$$n_1\omega_1 + n_2\omega_2 = n_3\omega_3 \tag{1.118}$$

that cannot be achieved with normal dispersion for $\omega_3 = \omega_1 + \omega_2$.

In practical implementations, phase matching is typically achieved through the use of birefringent crystals, crystals with the refractive index dependent on the polarization of the incident light. In such cases, the highest-frequency field is polarized along the directions with the lowest refractive index.

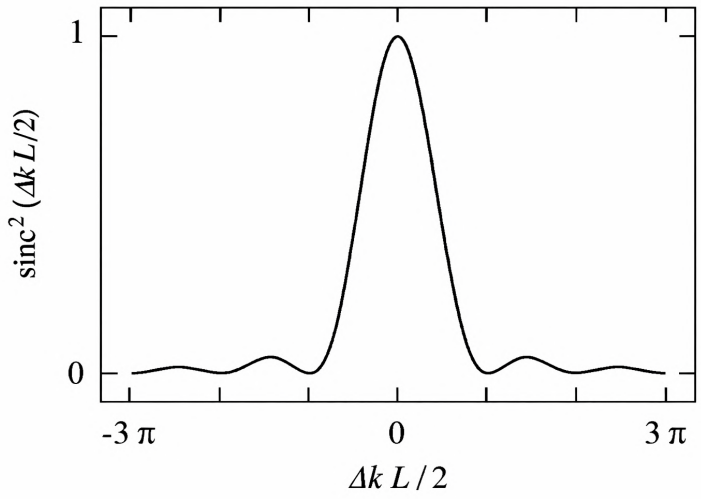

Figure 4: Effects of wavevector mismatch on the efficiency of sum-frequency generation. [1]

1.6 Peculiarities of Focused Gaussian Beams

Until now the considered fields were in the form of infinite plane waves; however, especially in microscopy, the light is usually focused into the nonlinear medium of interest.

To extend the previous analysis to focused beams, the first step is to express the electric field and the polarization for each frequency component as

$$\mathbf{E}_{\omega_n}(\mathbf{r},t) = \mathbf{A}_{\omega_n}(\mathbf{r})e^{i(k_n z-\omega_n t)} \tag{1.119}$$

$$\mathbf{P}_{\omega_n}(\mathbf{r},t) = \mathbf{p}_{\omega_n}(\mathbf{r})e^{i(k_n' z-\omega_n t)} \tag{1.120}$$

where the z-direction is still the propagation direction, but the plane wave representation is surpassed by allowing $\mathbf{A}_{\omega_n}(\mathbf{r})$ and $\mathbf{p}_{\omega_n}(\mathbf{r})$ to vary in space. These expressions are inserted into the driven wave equation already obtained in Eq. 1.98 to give

$$2ik_n\frac{\partial \mathbf{A}_{\omega_n}}{\partial z} + \nabla_T^2 \mathbf{A}_{\omega_n} = -\frac{\omega_n^2}{\epsilon_0 c^2}\mathbf{p}_{\omega_n} e^{i(k_n'-k_n)z} \tag{1.121}$$

where the factor $\partial^2 \mathbf{A}_{\omega_n}/\partial z^2$ is dropped for the second time due to the fact that it is small compared to $\partial \mathbf{A}_{\omega_n}/\partial z$. Since the z-direction is the dominant propagation direction of the field, it is convenient to divide the Laplacian between the parallel $\partial^2/\partial z^2$ and transverse $\nabla_T^2 = \partial^2/\partial x^2 + \partial^2/\partial y^2$ components so that $\nabla^2 = \partial^2/\partial z^2 + \nabla_T^2$.

The solution for Eq. 1.121 for a free propagating optical wave, that is, for the case in which the driving term on the right side vanishes, is in the form of a beam with a gaussian transverse intensity distribution [5]. Considering the fields scalar for convenience, the beam's amplitude can be expressed as

$$A(r,z) = \frac{\mathcal{A}}{1+i\varsigma} e^{-\frac{r^2}{\omega_0^2(1+i\varsigma)}} \tag{1.122}$$

where

$$\varsigma = \frac{2z}{k\omega_0^2} \tag{1.123}$$

and where ω_0 represents the beam waist radius, which is the lowest value of the beam radius, found at the focal point $z = 0$. In general, the beam radius $\omega(z)$ is defined as the distance at which the amplitude decreases by a factor $1/e$ and its distribution along the z-direction is given by

$$\omega(z) = \omega_0 \sqrt{1 + \left(\frac{\lambda z}{\pi \omega_0^2}\right)^2} \tag{1.124}$$

Other figures of merit for the gaussian beam, shown in Fig. 5, are the radius of curvature of the optical wavefront

$$R(z) = z\left[1 + \left(\frac{\pi\omega_0^2}{\lambda z}\right)^2\right] \tag{1.125}$$

and the confocal parameter

$$b = k\omega_0^2 \tag{1.126}$$

that is a measure of the longitudinal extent of the focal region.

It is now possible to study the excitations generated in a nonlinear material by a gaussian beam like the one just depicted. Specifically, starting from a

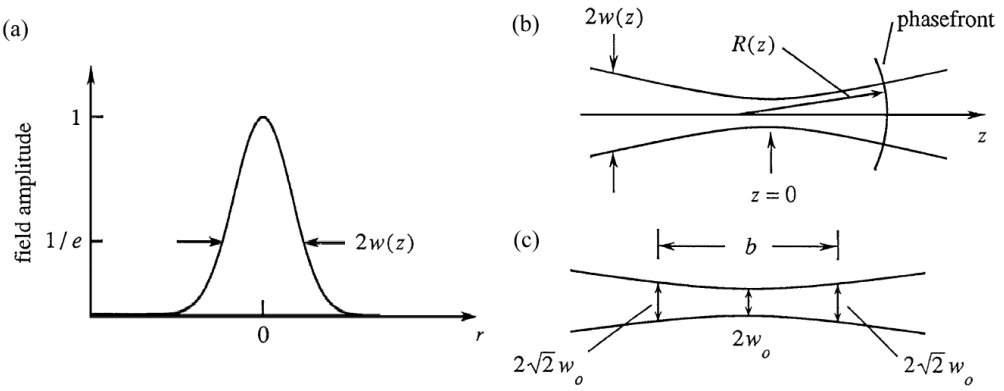

Figure 5: (a) Field amplitude distribution of a Gaussian beam. (b) Variation of the beam radius ω and wavefront curvature R with position z. (c) Relation between the beam waist radius and the confocal parameter b. [1]

fundamental beam of frequency ω_1, the generation of the q-order harmonic component with frequency $\omega_q = q\omega_1$ is considered. The complex amplitude of the fundamental wave follows Eq. 1.122 as

$$A_{\omega_1}(r,z) = \frac{\mathcal{A}_{\omega_1}}{1+i\varsigma} e^{-\frac{r^2}{\omega_0^2(1+i\varsigma)}} \tag{1.127}$$

where the fundamental beam is assumed not depleted, so $\mathcal{A}_{\omega_1}$ is constant, while the amplitude A_{ω_q} of the harmonic component must obey Eq. 1.121 as

$$2ik_q \frac{\partial \mathbf{A}_{\omega_q}}{\partial z} + \nabla_T^2 \mathbf{A}_{\omega_q} = -\frac{\omega_q^2}{\epsilon_0 c^2} \mathbf{p}_{\omega_q} e^{i(qk_1' - k_q)z} \tag{1.128}$$

where this time the complex amplitude of the nonlinear polarization that acts as a source term does not vanish but is taken equal to $p_{\omega_q} = \epsilon_0 \chi^{(q)} A_{\omega_1}^q$ and the q-order nonlinear susceptibility is $\chi^{(q)} = \chi^{(q)}(\omega_q; \omega_1, \ldots, \omega_1)$, so Eq. 1.128 becomes

$$2ik_q \frac{\partial \mathbf{A}_{\omega_q}}{\partial z} + \nabla_T^2 \mathbf{A}_{\omega_q} = -\frac{\omega_q^2}{c^2} \chi^{(q)} A_{\omega_1}^q e^{i(qk_1 - k_q)z} \tag{1.129}$$

It makes sense to consider a solution with the same radial dependence of the

source term in Eq. 1.127, but where $\mathcal{A}_{\omega_q}$ now varies along the z-direction

$$A_{\omega_q}(r,z) = \frac{\mathcal{A}_{\omega_q}(z)}{1+i\varsigma} e^{-\frac{qr^2}{\omega_0^2(1+i\varsigma)}} \tag{1.130}$$

that inserted in Eq. 1.129 gives

$$\frac{d\mathcal{A}_{\omega_q}}{dz} = \frac{iq\omega_1}{2n_q c}\chi^{(q)}\mathcal{A}_1^q \frac{e^{i(qk_1-k_q)z}}{(1+i\varsigma)^{q-1}} \tag{1.131}$$

It is important to note from Eq. 1.130 that the solutions for the harmonic components correspond to gaussian beams with the same confocal parameter b as the fundamental one, which is expected since nonlinear phenomena generate radiation coherently with the excitation. As a consequence of this, and due to the fact that $\omega_q = q\omega_1$ and that

$$b = k\omega_0^2 = \frac{n\omega}{c}\omega_0 \tag{1.132}$$

the beam waist radius for the q-order harmonic beam is $\sqrt{q}$ times smaller than the one of the fundamental field.

Eq. 1.131 can be integrated starting from the entrance of the nonlinear medium set at z_0 to obtain

$$\mathcal{A}_{\omega_q}(z) = \frac{iq\omega_1}{2n_q c}\chi^{(q)}\mathcal{A}_1^q \int_{z_0}^{z} \frac{e^{i(qk_1-k_q)z'}}{\left(1+\frac{2iz'}{b}\right)^{q-1}} dz' \tag{1.133}$$

and the integral term can be evaluated for the case of a tight focus $b << z$, resulting in

$$\int_{z_0}^{z} \frac{e^{i(qk_1-k_q)z'}}{\left(1+\frac{2iz'}{b}\right)^{q-1}} dz' = \begin{cases} 0 & \Delta k \leq 0 \\ \dfrac{b}{2}\dfrac{2\pi}{(q-2)!}\left(\dfrac{b\Delta k}{2}\right)^{q-2} e^{-\frac{b\Delta k}{2}} & \Delta k > 0 \end{cases} \tag{1.134}$$

where the wavevector mismatch is $\Delta k = qk_1 - k_q$.

Interestingly, Eq. 1.134 shows that the efficiency of harmonic generation

vanishes for the case of perfect phase matching $\Delta k = 0$. This is the opposite of what happens in the plane waves case discussed earlier, where perfect phase matching corresponds to maximum efficiency. The cause of this discrepancy lies in the negative phase shift that every beam experiences when passing through its focus, called Gouy shift from the physicist who first studied the phenomenon [6].

In nonlinear optics this effect is particularly critical, as in general the q-order nonlinear polarization experiences a phase shift q times larger than the one experienced by the fundamental beam [1]. Because of this, in contrast with the plane waves case, to efficiently couple the induced polarization with the generated radiation, it is necessary to have a positive wavevector mismatch that compensates for the Gouy phase shift caused by the focusing. This behavior plays a particularly important role in third-order (and, more generally, any odd-order) nonlinear effects and will be examined in detail in the next chapter.

2. Main Nonlinear Processes used in Microscopy

A key advantage of exploiting nonlinear effects in microscopy is to provide enhanced transverse and longitudinal resolution. The resolution increases because nonlinear interactions occur more efficiently in the region of highest intensity, meaning that in a tightly focused laser beam the signal is produced almost entirely in the focal volume [1]. Microscopy that relies on nonlinear radiation generation also benefits from the fact that the detected signal is well separated in frequency from unwanted background light produced by linear scattering of the incident beam. In addition, harmonic generation shifts the signal to higher frequencies, allowing one to illuminate the sample with light of a sufficiently long wavelength to avoid damage to biological tissue while still attaining a resolution that would usually require a much shorter wavelength. Nonlinear microscopy can also take advantage of the inherent nonlinear optical properties of biological specimens to increase selectivity, as different signals are preferentially produced by specific components of the sample, eliminating the need to use labels that can disrupt the biological processes under study.

The most commonly used nonlinear effects for non-invasive optical investigation of matter are the lower-order ones that involve only three or four photons. This is because of the relatively large magnitudes of the associated second- and third-order nonlinear susceptibilities, $\chi^{(2)}$ and $\chi^{(3)}$, compared to the higher-order terms, that make their signals experimentally accessible. [4].

The $\chi^{(2)}$ process most widely used in microscopy is Second Harmonic Generation (SHG), where two incident photons of identical energy interact with a medium and coherently produce a third photon at twice the energy. When instead photons of different frequencies interact, the energy of the generated photon can correspond to either the algebraic sum or the algebraic difference of the initial energies. These processes are known as Sum-Frequency Generation

(SFG) and Difference-Frequency Generation (DFG) and can also collectively be referred to as Three Wave Mixing (TWM).

In contrast, $\chi^{(3)}$ nonlinear effects involve the interaction of four photons. When three incoming photons of identical energy generate a fourth photon with three times that energy, the process is called Third Harmonic Generation (THG), the third-order equivalent of SHG. In general, lifting the energy degeneracy of the incoming photons, a range of mixing phenomena can occur, collectively referred to as Four Wave Mixing (FWM). Representative examples of these processes include two incident photons that produce two new photons with different energies and three incoming photons that combine into a single outgoing photon [4].

Microscopy based on second-harmonic generation was first demonstrated in 1972 by Hellwarth and Christensen [7] and, during the following decades, numerous techniques have been developed exploiting nonlinear effects to improve both spatial resolution and signal strength [8] [9] [10].

This second chapter will focus on the most important second- and third-order nonlinear effects, since they are the most widely used in microscopy, describing their peculiarities and differences in the context of biological imaging applications.

2.1 Parametric and Nonparametric Processes

Processes like SHG, THG and Wave Mixing are consider parametric and can be modeled simply as an exchange of photons between the different frequency components of the field. The case for second harmonic generation is illustrated in Fig. 6, where the solid lines represent energy levels, like the atomic ground states, while dashed lines represent virtual levels. The virtual levels are not energy eigenstates of the system, but rather represent the combined energy of one eigenstate of the atom and one or more photons [1]. The picture shows how two photons at frequency ω are destroyed and one photon at frequency 2ω is created in the same quantum mechanical process, without changing the eigenstate of the atomic system. This is the main property that distinguishes parametric processes from nonparametric ones.

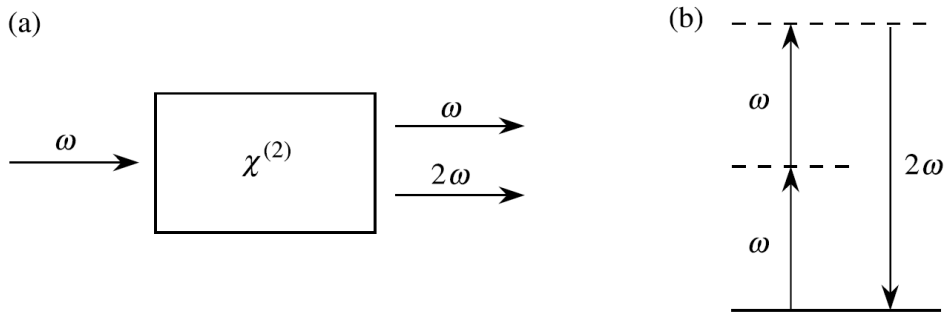

Figure 6: (a) Schematic of second harmonic generation. (b) Energy-level diagram describing the process. [1]

A parametric process is a process in which the initial and final quantum mechanical states of the system are identical. During these processes the interaction removes the population from the ground states only for brief instants, where it interacts in a virtual state without reaching the next energy eigenstate. Due to the uncertainty principle, a virtual level can be occupied only for a time of the order $\hbar/\delta E$ where δE is the energy difference from the nearest energy eigenstate [3]. In contrast, nonparametric processes involve transfer from one energy eigenstate to another, thus changing the quantum mechanical state of the system.

Parametric processes conserve photon energy and can be described using real susceptibility; meaning that they are scattering-based processes where no absorption is involved. This gives them some peculiar characteristics compared to other optical processes, such as the absence of stokes shift. On the other hand, nonparametric processes require complex susceptibility and do not conserve photon energy. The interaction with the medium is based on absorption and re-emission and energy is transferred between the photons and the material [1].

One notable example of a nonparametric process used in microscopy is Two-Photon Excited Fluorescence (TPEF), where two photons are absorbed by the material in the transition from the ground state to an excited one. A photon with frequency higher than the initial two is then emitted during relaxation. SHG and TPEF may appear similar, as both involve the interaction between

the sample and two photons, and indeed present many technical similarities that allow one to easily integrate them into the same system. However, the two processes are fundamentally different. In SHG, being parametric, frequency conversion is achieved through virtual states without a net transfer of energy to the system, whereas in TPEF the photons are absorbed, moving the system to a new energetic eigenstate [11]. Due to the fact that in parametric processes there is ideally no energy transferred to the medium, they lead to substantially reduced photo-bleaching and photo-toxicity compared to nonparametric fluorescence methods such as TPEF [12]. In addition, SHG emission is sensitive to fine structural characteristic, like the ones found in collagen and myosin, and shows high coherence with the fundamental beam and emission directionality. TPEF emission, on the other hand, originating from spontaneous relaxation of excited energy states, is an incoherent and isotropic emission process.

Although many other nonparametric processes are important both for microscopy and nonlinear optics in general, the rest of the dissertation will focus specifically on parametric processes applied to microscopy.

2.2 Second Harmonic Generation

In SHG, two incident photons at frequency ω are instantaneously combined interacting via the nonlinear polarization of the material to generate a single coherent photon at frequency 2ω. This process, as with all second-order nonlinear processes, is governed by the second-order nonlinear susceptibility tensor $\chi^{(2)}$ which, recalling Eq. 1.2, can be used to express the second-order component of the nonlinear polarization as

$$P^{(2)}(t) = \epsilon_0 \chi^{(2)} E^2(t) \tag{2.1}$$

The nonlinear susceptibility $\chi^{(2)}$ is a bulk property of the material that microscopically arises from the interaction between the molecular dipole and the field. Specifically, the molecular dipole moment can be expressed as

$$\mathbf{p} = \mathbf{p}^{(0)} + \alpha \mathbf{E} + \beta \mathbf{E}^2 + \gamma \mathbf{E}^3 + \dots \tag{2.2}$$

where $\mathbf{p}^{(0)}$ is the permanent dipole of the molecule, α is the (linear) polarizability of the molecule and β, γ are the first and second (nonlinear) hyperpolarizabilities, respectively [11].

Molecules capable of emitting SHG are characterized by a high hyperpolarizability β, which strongly depends on their symmetry. Indeed, in the case of a molecule that has a center of symmetry, the elements that contribute to the hyperpolarizability cancel each other out, preventing the formation of SHG. Thus, as demonstrated before, the generation of even harmonics is possible only in non-centrosymmetric materials. Moreover, the coherent nature of SHG implies that the total signal is the result of interferences between the individual contributions of each molecule. When the electric fields emitted by the dipole moments are in phase and thus constructively interfere, the resulting SHG emissions are coherently added. In contrast, there is destructive interference when the dipole moments have random directions and the SHG signal vanishes. [1]

On a macroscopic scale, the non-linear susceptibility $\chi^{(2)}$ results from the coherent sum of the individual hyperpolarizabilities of all molecules within a volume. The relation between molecular dipoles and macroscopic susceptibility is given by [11]

$$\chi^{(2)} = N < \beta > \tag{2.3}$$

where N is the density of the molecules and $< \beta >$ refers to the orientational average of the hyperpolarizability.

To have a second-order nonlinear response from the sample, it must present a non-centrosymmetric structure at the molecular scale so that $\beta \neq 0$, and the dipoles must be arranged in a nonrandom fashion so that $< \beta > \neq 0$. In biological samples, the predominant structures that respect these conditions are type I and II collagen and myosin, present in muscles [12].

The magnitude of β, and thus the SHG signal, can be increased by resonant enhancement, which means that, when the SHG excitation energy is close to the transition energy between two energy eigenstates of the system, resonance with the transition process will greatly increase the intensity of the SHG. This can be seen from the dependence of the hyperpolarizability on the excitation

frequency ω [2]

$$\beta \sim \frac{\Delta\omega f \Delta\mu}{(\Delta\omega^2 - \omega^2)(\Delta\omega^2 - 4\omega^2)} \tag{2.4}$$

where $\Delta\omega$ is the difference in frequency between the ground state and the excited state considered, f is the a factor that describes the optical transition and $\Delta\mu$ is the change in dipole moment upon the transition. When the frequency of the two impinging photons matches the difference between the two real states $2\omega = \Delta\omega$, maximal hyperpolarizability is achieved. It is important to note that, when resonant enhanced SHG occurs, TPEF occurs simultaneously, leading to increased photo-bleaching and photo-toxicity.

The nature of a biological system also affects the emission direction of the SHG signal. In contrast to perfect crystals, where the SHG signal can be perfectly phase matched and so the emission is totally forward directed, in a biological environment phase matching is never fully satisfied and this causes a distribution of forward and backward components [12]. However, it is important to take into account how the difference in coherence length between the forward and backward emitted radiation affects the real emission direction distribution. Recalling Eq. 1.117, the coherence length of a nonlinear interaction is

$$l_c = \frac{\pi}{\Delta k} \tag{2.5}$$

This is a few microns for the forward SHG signal in most materials, which is enough for a consistent phase-matching within a focal volume. However, the wavevector mismatch Δk in the backward direction is much larger, and thus the coherence length for backward emitted radiation is only a few tens of nanometers at most, which means that the backward signal is always poorly phase matched. For this reason, the pure backward SHG signal is always very weak [11]. Importantly, since the backward SHG signal is usually weak, it should not be confused with the scattered forward SHG signal. Indeed, since most biological samples are highly scattering, a significant part of the forward signal will get scattered or reflected towards the backward direction after its generation. This is what makes epidetection possible even with highly coherent and directional signals such as SHG.

Considering now a laser beam whose electric field strength is

$$E(t) = E_\omega e^{-i(\omega t)} + c.c. \tag{2.6}$$

with just one frequency component oscillating at ω, Eq. 2.1 becomes

$$P^{(2)}(t) = 2\epsilon_0 \chi^{(2)} E_\omega E_{-\omega} + \left[\epsilon_0 \chi^{(2)} E_\omega^2 e^{-i(2\omega t)} + c.c.\right] \tag{2.7}$$

where complex conjugates are expressed as before as $E_{-\omega} = E_\omega^*$.

The first term in Eq. 2.7 is a contribution at zero frequency that does not generate electromagnetic radiation but leads to a process called *optical rectification*, where a static electric field is created across the nonlinear medium. The second term is a contribution at frequency 2ω that according to the driven wave expression in Eq. 1.98 can generate a new field component at the second harmonic frequency, that is, the SHG signal.

The electric field inside the material is therefore now composed of two frequency components, dependent on the penetration depth z inside the material

$$E(z,t) = E_{\omega_1}(z) e^{-i(\omega_1 t)} + E_{\omega_2}(z) e^{-i(\omega_2 t)} + c.c. \tag{2.8}$$

where the frequencies were renamed as $\omega = \omega_1$ and $2\omega = \omega_2$ and where

$$E_{\omega_j}(z) = A_{\omega_j}(z) e^{i(k_j z)} \tag{2.9}$$

The polarization can be expressed in the same manner

$$P(z,t) = P_{\omega_1}(z) e^{-i(\omega_1 t)} + P_{\omega_2}(z) e^{-i(\omega_2 t)} + c.c. \tag{2.10}$$

while the polarization amplitudes can be derived using Eq. 1.12 as

$$P_{\omega_1}(z) = 2\epsilon_0 \chi^{(2)}(\omega_1; \omega_2, -\omega_1) A_{\omega_2} A_{-\omega_1} e^{i(k_2 - k_1)z} \tag{2.11}$$

$$P_{\omega_2}(z) = \epsilon_0 \chi^{(2)}(\omega_2; \omega_1, \omega_1) A_{\omega_1}^2 e^{i(2k_1 z)} \tag{2.12}$$

where Eq. 2.11 represents the process opposite to second harmonic generation, for which a photon at frequency $\omega_2 = 2\omega_1$ is destroyed and two photons at fre-

quency ω_1 are created. This process is possible because after some distance z both field components are present inside the material and the ω_1 photons can stimulate the transition, transferring energy from the harmonic field back to the fundamental one. In practice, the balance between these two processes depends on the phase between the radiation and the driving polarization for each point in the material that, in turn, depends on the wavevector mismatch. Note that the constant pump approximation is lifted, so both A_{ω_1} and A_{ω_2} change within the material. For convenience, the medium is considered dispersionless, so the nonlinear susceptibility behaves like a constant for both frequencies and its arguments can be dropped.

Applying the driven wave equation from Eq. 1.98 to both components gives the coupled-amplitude equations

$$\frac{dA_{\omega_1}}{dz} = \frac{i\omega_1^2\chi^{(2)}}{k_1c^2}A_{\omega_2}A_{-\omega_1}e^{-i\Delta kx} \tag{2.13}$$

$$\frac{dA_{\omega_2}}{dz} = \frac{i\omega_2^2\chi^{(2)}}{2k_2c^2}A_{\omega_1}^2e^{i\Delta kx} \tag{2.14}$$

where $\Delta k = 2k_1 - k - 2$ is the wavevector mismatch.

From the assumption of a lossless medium, the total field intensity expressed as

$$I = I_{\omega_1} + I_{\omega_2} \tag{2.15}$$

is expected to remain constant throughout the interaction, as the energy is transferred between the two frequency components but is not absorbed by the medium. The intensity of each component is linked to its amplitude as

$$I_{\omega_j} = 2\epsilon_0 n_j c|A_{\omega_j}|^2 \tag{2.16}$$

In this case, it is convenient to define a normalized version of the field amplitudes $u_{\omega_1}(z)$ and $u_{\omega_2}(z)$, which, due to the conservation of the intensity, satisfy the relation

$$u_{\omega_1}^2(z) + u_{\omega_2}^2(z) = 1 \tag{2.17}$$

everywhere in the material.

The coupled-amplitude equations in Eqs. 2.13 and 2.14 must be solved simultaneously, as the coupling inside the material influences both amplitudes. Solving those equations requires some tedious algebra [13], but for the case of perfect phase matching $\Delta k = 0$ leads to a simple solution

$$u_{\omega_1}(\zeta) = \operatorname{sech}(\zeta) \tag{2.18}$$

$$u_{\omega_2}(\zeta) = \tanh(\zeta) \tag{2.19}$$

where the initial conditions are of only the fundamental component present, $u_{\omega_1}(0) = 1$ and $u_{\omega_2}(0) = 0$, and ζ is a normalized distance parameter defined as

$$\zeta = \frac{z}{l} \tag{2.20}$$

where

$$l = \sqrt{\frac{n_1^2 n_2 \epsilon_0 c}{2I}} \frac{2c}{\omega_1 \chi^{(2)}} \tag{2.21}$$

is the characteristic length over which the fields exchange energy.

The solutions in Eqs. 2.18 and 2.19, valid for perfect phase matching, are shown graphically in Fig. 7. Under these conditions, in the limit $\zeta \to \infty$, all incident radiation is converted to the harmonic field.

The coupled-amplitude equations that describe second harmonic generation can also be solved for arbitrary wavevector mismatch $\Delta k \neq 0$ via even more tedious algebra [13], which is not reported. However, the results are summarized graphically in Fig. 8. For a non-zero wavevector mismatch, the energy alternates back and forth between the two components, leading to an oscillatory solution. As Δk increases, the coherence length of the interaction decreases, leading to an increase in the spatial frequency of these oscillations. An increase in Δk also reduces the overall efficiency of the process, lowering the maximum intensity reached by the generated harmonic field.

2.3 Third Harmonic Generation

This process is in many ways similar to second harmonic generation and in many others profoundly different. In fact, because of these differences, SHG

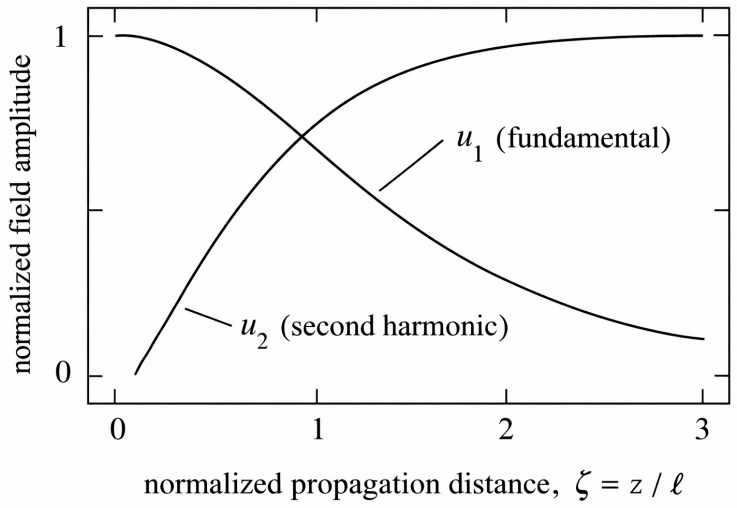

Figure 7: Spatial variations of the fundamental and second-harmonic field amplitudes for the case of perfect phase matching. [1]

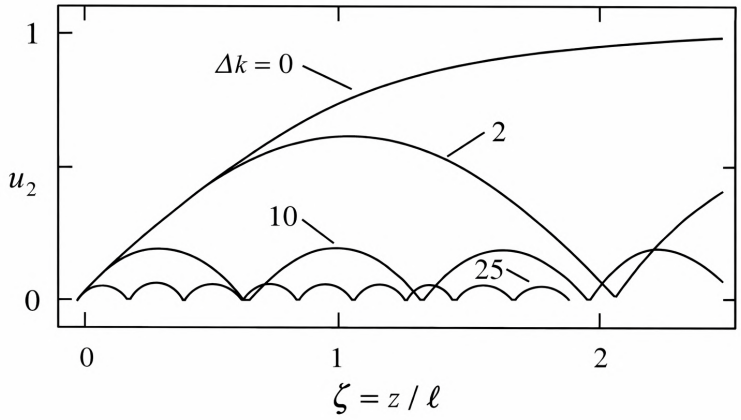

Figure 8: Effect of wavevector mismatch on the efficiency of second-harmonic generation. [1]

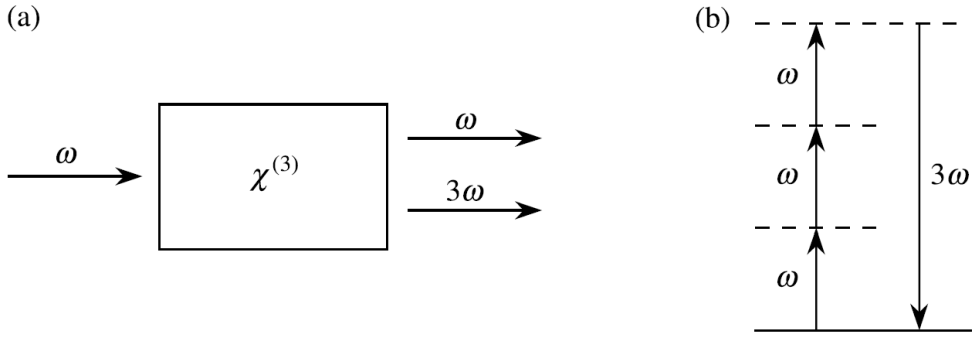

Figure 9: (a) Schematic of third harmonic generation. (b) Energy-level diagram describing the process. [1]

and THG images are usually both distinct and complementary, so THG techniques are often an excellent addition to standard SHG microscopy [14]. This is again a parametric process in which three photons at frequency ω interact with the nonlinear medium up to a virtual level, producing a new photon at frequency 3ω that is scattered coherently, as shown schematically in Fig. 9.

As highlighted before, THG signal is not sensitive to centrosymmetry, so its generation is not limited to organized structures, as for the case of SHG. However, because of the Gouy phase shift at the focus, it tends to vanish for homogeneous media. Some discontinuity in the refractive index inside the focal volume is required to balance the effect of the shift and produce an effective THG signal. Thus, this technique is highly sensitive to membranes and interfaces, as well as to any heterogeneity at the scale of the focus. A common structure in biological samples that is efficient in generating a THG signal is lipid droplets diffused in water, as they have sub-focal dimensions and high third-order optical susceptibility. A similarity between the first-order (linear) and third-order (or any odd-order) effects can be noted here, as both are preferentially sensitive to changes in the refractive index.

Following the same derivation proposed before for SHG, from Eq. 1.2, the expression for the third-order nonlinear polarization is recalled as

$$P^{(3)}(t) = \epsilon_0 \chi^{(3)} E^3(t) \tag{2.22}$$

and considering a monochromatic laser beam whose electric field oscillates at frequency ω, like in Eq. 2.6, the expression becomes

$$P^{(3)}(t) = \epsilon_0 \chi^{(3)} \left[E_\omega^3 e^{-i(3\omega t)} + 3E_\omega^2 E_{-\omega} e^{-i(\omega t)} \right] \tag{2.23}$$

where the first term is a contribution at frequency 3ω that generates a new field component, the THG signal, at the third harmonic frequency in accordance with the driven wave equation. The second term instead describes a contribution to the polarization that oscillates at the same frequency ω of the fundamental field. This is a novel third-order process, different from the optical rectification encountered at second-order, and leads to a nonlinear contribution to the refractive index experienced by the wave at frequency ω [1]. This nonlinearity in the refractive index can lead to many interesting effects, like self focusing, that are however outside the scope of this thesis.

The aim is now to understand more in depth why the presence of the Gouy phase shift in focused beam leads the THG signal to vanish inside homogeneous media. As seen before, the Gouy shift is a negative phase shift of π radiant that a beam encounters when passing through its focus. This effect can be seen in Fig. 10, where the intensity and phase profile of a beam near the focus are reported.

The frequencies components of the field can be initially expressed as plain waves

$$E_\omega(z) = A_\omega e^{i(k_\omega z)} \tag{2.24}$$

$$E_{3\omega}(z) = A_{3\omega}(z) e^{i(k_{3\omega} z)} \tag{2.25}$$

where the fundamental beam is assumed to be undepleted in the constant pump approximation, so that its amplitude A_ω is constant. The field inside the material is thus expressed as

$$E(z,t) = E_\omega(z) e^{-i(\omega t)} + E_{3\omega}(z) e^{-i(3\omega t)} + c.c. \tag{2.26}$$

As before, the driven wave equation in Eq. 1.98 is used to obtain the coupling

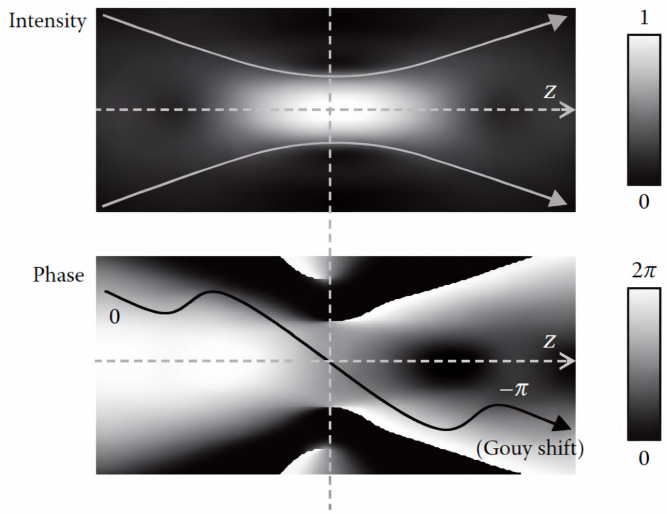

Figure 10: Intensity and phase distribution of a focused Gaussian beam near the focus. [14]

between the amplitudes of the fundamental and harmonic component

$$\frac{dA_{3\omega}}{dz} \propto A_{\omega}^{3} e^{i(\Delta k z)} \tag{2.27}$$

where $\Delta k = k_{3\omega} - 3k_{\omega}$. This dependence can be integrated between $z = 0$ and $z = L$ to obtain the dependence of the amplitude $A_{3\omega}$ on the propagation distance L within the sample. The solution is identical to the one already obtained for the case of sum-frequency generation

$$A_{3\omega} \propto A_{\omega}^{3} L \mathrm{sinc}\left(\frac{\Delta k L}{2}\right) \tag{2.28}$$

In the presence of non-zero wavevector mismatch, $\Delta k \neq 0$, the amplitude of the harmonic component, and therefore its intensity, oscillates as a function of L with a characteristic spatial period of $\pi/\Delta k$ [14]. Thus, the THG signal starts to decrease when the length L of the interaction gets larger than this period, which is identified as the coherence length of the interaction

$$l_c = \frac{\pi}{\Delta k} = \frac{\pi}{|k_{3\omega} - 3k_{\omega}|} \tag{2.29}$$

From this expression it can also be seen why the backward emitted signal is always weaker than the forward one, as said in the previous section for SHG. That is because, for backward emission of the harmonic wave, the wavevector changes sign $k_{3\omega} \rightarrow -k_{3\omega}$, and so Eq. 2.29 becomes

$$l_c^{Back} = \frac{\pi}{|k_{3\omega} + 3k_\omega|} \tag{2.30}$$

that is clearly a shorter coherence length compared to the forward emission case, meaning that the THG signal emitted in the backwards direction is poorly phase matched and oscillates with a small spatial period and a low maximum intensity, resulting in a faint signal compared to the forward direction. The same reasoning applies for the SHG case.

The Gouy phase shift of π radiant, introduced by the focus, effectively changes the phase matching condition for the THG process as [14]

$$\Delta k = k_{3\omega} - 3(k_\omega + k_G) \tag{2.31}$$

where k_G is the negative mismatch introduced by the Gouy phase shift. This changes the coherence length of the interaction

$$l_c = \frac{\pi}{|k_{3\omega} - 3(k_\omega + k_G)|} \approx \frac{\pi}{|3k_G|} \tag{2.32}$$

where the approximation is valid for the limit of thigh focusing. In that case, the dominant factor defining the wavevector mismatch and the coherence length is no longer the material dispersion, but rather the Gouy phase.

Using this model, the critical size of the inhomogeneities that can give rise to THG can be studied. A spherical object of diameter d, with third-order susceptibility, is considered to be located at the focus of the beam. The harmonic signal detected in the forward direction $z > 0$ is denoted as F-THG and the harmonic signal detected in the backward direction $z < 0$ as B-THG.

The solution is achieved computationally [14] and Figure 11 reports how the F-THG and B-THG signals vary with the sphere diameter. When the sphere size increases from zero, both F-THG and B-THG initially grow coherently, with their intensities scaling quadratically with the sphere volume. However,

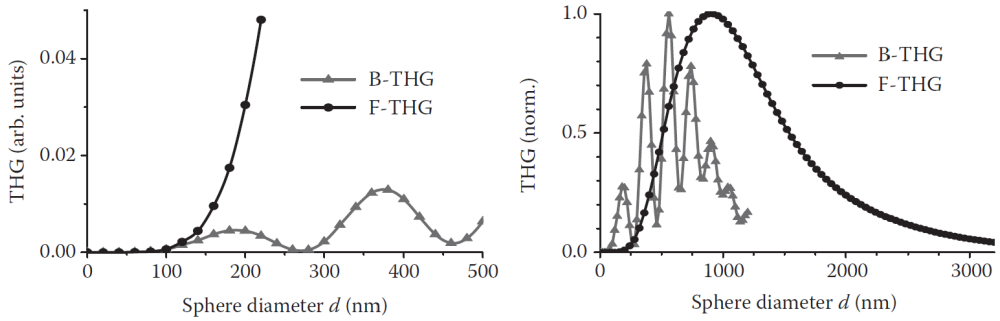

Figure 11: Forward (F-THG) and backward (B-THG) emitted THG signal generated in a sphere centered in the focus point, depending on the sphere diameter. [14]

as the diameter continues to grow, destructive interference begins to occur in the backward direction, leading to a reduction of the backward signal [2]. This effect is caused by the larger phase mismatch experienced in that direction, as just discussed. As a result, the B-THG signal displays damped oscillations with a period equal to twice the backward coherence length given by Eq. 2.30.

The behavior of the F-THG signal follows a simpler trend; it increases with the diameter of the sphere until the destructive interference arising from the Gouy phase shift becomes significant. For larger spheres, the F-THG generated at the sphere center then drops to zero as the sphere effectively behaves like a homogeneous medium on the scale of the excitation volume. No noticeable oscillations appear in the F-THG signal for the tight focus limit, as the forward coherence length is long enough so that the position $z = 2l_c$ is already outside the focal region where the excitation intensity is negligible compared to its value at the focus. Nevertheless, in strongly dispersive media where the coherence length is shorter than the focal dimension, oscillations would also be observable in the forward direction.

Thus, the THG signal can be obtained from heterogeneities close in size to the coherence length, that itself depends on the axial extent of the Gouy phase shift, as expressed in Eq. 2.32. However, the extend of the Gouy shift is itself influenced by the excitation Numerical Aperture (NA). In optical microscopy, the numerical aperture is a dimensionless number that characterizes the range

of angles over which an objective can accept or emit light, and it is defined as

$$NA = n\sin(\theta) \tag{2.33}$$

where n is the index of refraction between the lens and the sample and θ is the half-angle of the maximum cone of light that can enter or exit the lens. The relation between NA and coherence length can be expressed as [14]

$$l_c \propto \frac{1}{NA^2} \tag{2.34}$$

so changing the NA effectively changes the size of the objects that can generate the THG signal. For example, reducing the NA results in an increased visibility of large structures relative to small structures.

2.4 Wave Mixing Processes

In contrast with the harmonic generation processes just seen, wave mixing, also known as frequency mixing, arises from the interaction between different frequency components, which means between photons with different energy. The same derivation used for the harmonic case is proposed, but this time starting from an optical field with two distinct frequency components oscillating at frequencies ω_1 and ω_2

$$E(t) = E_{\omega_1} e^{-i(\omega_1 t)} + E_{\omega_2} e^{-i(\omega_2 t)} + c.c. \tag{2.35}$$

From Eq. 1.2 the second-order nonlinear polarization can be expressed as

$$\begin{aligned} P^{(2)}(t) =& 2\epsilon_0 \chi^{(2)} \left[E_{\omega_1} E_{-\omega_1} + E_{\omega_2} E_{-\omega_2}\right] \\ &+ \epsilon_0 \chi^{(2)} \left[E_{\omega_1}^2 e^{-i(2\omega_1 t)} + E_{\omega_2}^2 e^{-i(2\omega_2 t)} + c.c.\right] \\ &+ \epsilon_0 \chi^{(2)} \left[2E_{\omega_1} E_{\omega_2} e^{-i(\omega_1+\omega_2)t} + 2E_{\omega_1} E_{-\omega_2} e^{-i(\omega_1-\omega_2)t} + c.c.\right] \end{aligned} \tag{2.36}$$

where the first line represents optical rectification, the second represents second harmonic generation at frequencies $2\omega_1$ and $2\omega_2$ and the third line represents frequency mixing at frequency $(\omega_1 + \omega_2)$, called sum-frequency generation, and

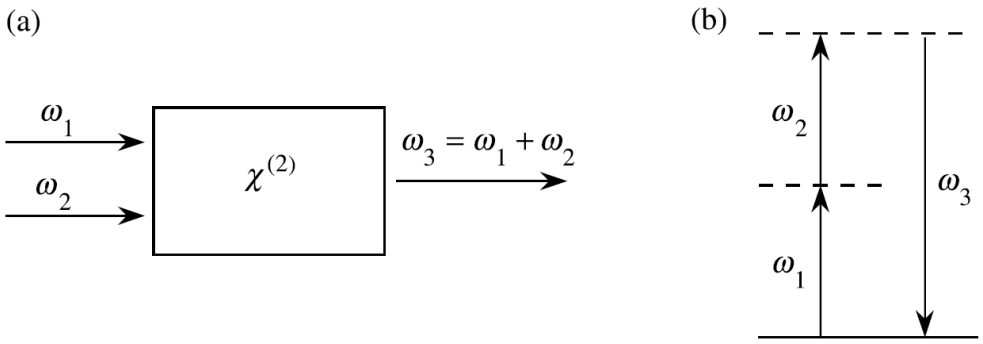

Figure 12: (a) Schematic of sum-frequency generation. (b) Energy-level diagram describing the process. [1]

frequency mixing at frequency $\omega_1 - \omega_2$, called difference-frequency generation.

The second-order SFG process shown in Fig. 12 is described by the nonlinear polarization

$$P^{(2)}_{(\omega_1+\omega_2)} = 2\epsilon_0\chi^{(2)}E_{\omega_1}E_{\omega_2}e^{-i(\omega_1+\omega_2)t} \tag{2.37}$$

that acts as a source of electromagnetic radiation that oscillates at frequency $\omega_3 = \omega_1 + \omega_2$. This is a parametric process where two photons with different frequencies interact in a nonlinear medium up to a virtual level and are converted into a new photon with a frequency that is the sum of the initial two.

Similarly, the second-order DFG process shown in Fig. 13 responds to the nonlinear polarization

$$P^{(2)}_{(\omega_1-\omega_2)} = 2\epsilon_0\chi^{(2)}E_{\omega_1}E_{-\omega_2}e^{-i(\omega_1.\omega_2)t} \tag{2.38}$$

that act as a source for electromagnetic radiation that oscillates at frequency $\omega_3 = \omega_1 - \omega_2$. As noted before, these expressions for the nonlinear polarization present a factor 2 that is absent in the SHG case. This is because, in frequency mixing, the interaction is between two distinct field components and is thus more intense compared to the harmonic case, where only one component is involved.

Intuitively, SFG and DFG can be regarded as two closely related nonlinear

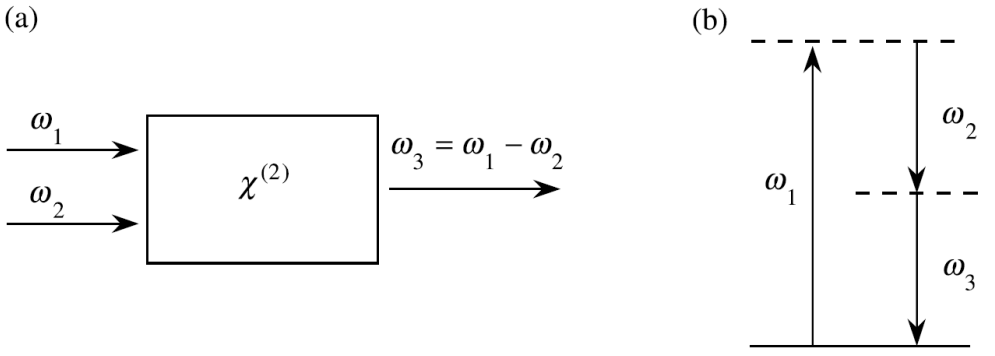

Figure 13: (a) Schematic of difference-frequency generation. (b) Energy-level diagram describing the process. [1]

optical processes. However, as illustrated in Fig. 13 for the case of DFG, there is a crucial distinction to be made. In difference-frequency generation, the creation of a photon at the new frequency $\omega_3 = \omega_1 - \omega_2$ occurs through the annihilation of a photon at frequency ω_1 and the simultaneous emission of a photon at frequency ω_2. The field component oscillating at frequency ω_2 stimulates the emission and is therefore amplified by the nonlinear interaction. This behavior is fundamentally different from that of sum-frequency generation, in which both components of the fundamental field are depleted by the interaction. This peculiarity of DFG is at the core of the development of optical parametric oscillators and optical parametric amplifiers [15].

Following the same approach, it is possible to express the third-order nonlinear polarization. Again, considering the field expressed in Eq. 2.35, Eq. 1.2 gives

$$\begin{aligned} P^{(3)}(t) = \epsilon_0\chi^{(3)}\big[&(3E_{\omega_1}E_{-\omega_1} + 6E_{\omega_2}E_{-\omega_2})E_{\omega_1}e^{-i(\omega_1 t)} \\ &+ (6E_{\omega_1}E_{-\omega_1} + 3E_{\omega_2}E_{-\omega_2})E_{\omega_2}e^{-i(\omega_2 t)} + c.c.\big] \\ +\epsilon_0\chi^{(3)}&\left[E_{\omega_1}^3 e^{-i(3\omega_1 t)} + E_{\omega_2}^3 e^{-i(3\omega_2 t)} + c.c.\right] \\ +\epsilon_0\chi^{(3)}&\left[3E_{\omega_1}^2 E_{\omega_2} e^{-i(2\omega_1+\omega_2)} + 3E_{\omega_1}E_{\omega_2}^2 e^{-i(\omega_1+2\omega_2)} + c.c.\right] \\ +\epsilon_0\chi^{(3)}&\left[3E_{\omega_1}^2 E_{-\omega_2} e^{-i(2\omega_1-\omega_2)} + 3E_{\omega_2}^2 E_{-\omega_1} e^{-i(2\omega_2-\omega_1)} + c.c.\right] \end{aligned} \tag{2.39}$$

where the first two lines represent the nonlinear contribution to the refractive index for frequencies ω_1 and ω_2, as seen in the previous section, the third line represents the third harmonic generation for these same frequencies, and the last two lines express the third-order wave mixing processes. These are analogous to the second order ones and lead to the generation of photons at frequencies $(2\omega_1 + \omega_2)$ and $(\omega_1 + 2\omega_2)$ for SFG and at frequencies $(2\omega_1 - \omega_2)$ and $(2\omega_2 - \omega_1)$ for DFG.

3. Experimental Setup: Design and Characterization

The microscopy system used for this thesis is located in the laboratory of the department of applied physics at the University of Geneva and has been developed over the last five years as part of the European FairCharm project. This EU-funded project involves many different institutions across Europe and aims to develop novel microscopy systems suitable for pursuing new therapeutic strategies for different types of diseases.

The system is a prototype and is still being developed to this day. As expressed in the introduction, the aim of this work was to implement and test a frequency mixing protocol on the already existing platform.

In this chapter, the main components of the system will be extensively described, along with the characterization conducted on them. After that, the new components and modifications introduced to achieve frequency mixing will be presented.

3.1 Laser Source and Beam Properties

As seen in the previous chapters, high instantaneous intensity is needed to produce detectable nonlinear signals, as the nonlinear response scales with powers of the illumination intensity. However, even when using focused beams, the power densities obtainable by conventional lasers are generally insufficient to produce signals adequate for practical imaging applications. An additional mechanism for increasing power density is required. This is achieved by focusing the light stimulus not only in space but also in time via the use of pulsed excitation. The development of ultra-fast, robust, and user-friendly pulsed laser sources has, in this context, been fundamental to the rapid diffusion of many nonlinear microscopy techniques.

It is now useful to describe the nonlinear processes via a more general approach compared to what was done in the previous chapters, considering only the power emitted from the nonlinear interaction with respect to the illumination intensity incident to the material and the cross-section σ of the process itself. Due to the pulsed nature of the light source, it is necessary to consider the time averages of these quantities [16]. For a generic second order nonlinear process, the power emitted is expressed as

$$\langle \Phi_2 \rangle = \sigma_2 \langle I^2 \rangle \tag{3.1}$$

It is usually more convenient to express this in terms of the average excitation intensity $\langle I \rangle$, rather than its second power, since it can be easily measured in practice. However, since the intensity varies over time due to the pulsed nature of the excitation, then $\langle I^2 \rangle \neq \langle I \rangle^2$. To account for this, the second-order temporal coherence factor of the illumination beam is introduced as [16]

$$g_2 = \frac{\langle I^2 \rangle}{\langle I \rangle^2} \tag{3.2}$$

so that Eq. 3.1 can be rewritten as

$$\langle \Phi_2 \rangle = \sigma_2 g_2 \langle I \rangle^2 \tag{3.3}$$

The advantage of using pulsed excitation rather than a continuous laser is expressed by the fact that $g_2 = 1$ for a continuous excitation and $g_2 > 1$ for a pulsed one. In particular, if the laser intensity arrives in short bursts of duration τ_p at regular intervals of period τ_l, the temporal coherence factor can be expressed as

$$g_2 = \frac{\tau_l}{\tau_p} \tag{3.4}$$

so that Eq. 3.3 can be expressed as

$$\langle \Phi_2 \rangle = \sigma_2 \frac{\tau_l}{\tau_p} \langle I \rangle^2 \tag{3.5}$$

Typical lasers employed in nonlinear microscopy possess second-order temporal

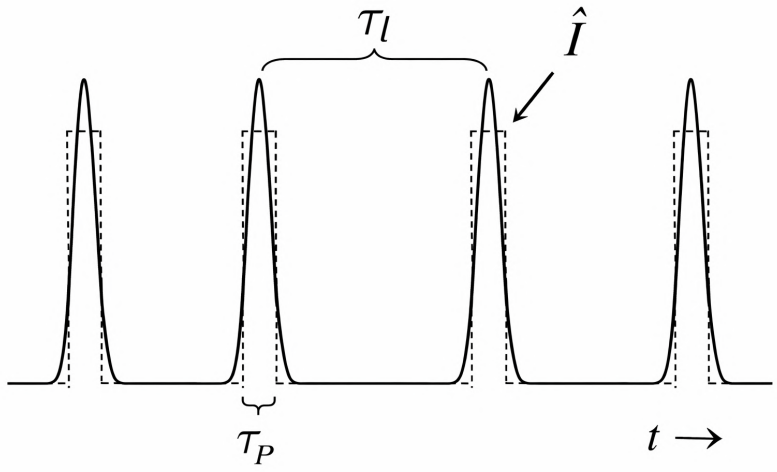

Figure 14: Pulsed laser intensity as a function of time, the dashed line represent the square function approximation of the pulses. [16]

coherence factors of the order of $g_2 \sim 10^4 - 10^5$, increasing the signal generated by several orders of magnitude compared to a continuous laser with the same average power [16].

The characteristic peak pulse intensity of the excitation can be defined as

$$\hat{I} = \frac{\tau_l}{\tau_p}\langle I \rangle \tag{3.6}$$

while the duty cycle of the laser is defined as

$$DC = \frac{\tau_p}{\tau_p + \tau_l} \tag{3.7}$$

and the parameters τ_p and $\hat{I}$ are sufficient to fully characterize the laser pulses for standard imaging applications, as shown in Fig. 14. Another important difference between pulsed and continuous lasers is that a pulsed laser can never be truly monochromatic. Indeed, for a laser to function in pulsed mode, its output must exhibit a spectral bandwidth at least on the order of $\Delta\omega = 1/\tau_p$ [1].

The same reasoning used for second-order nonlinear processes can also be

generalized for any n-order; in this case, the power emitted by the process in Eq. 3.1 becomes

$$\langle \Phi_n \rangle = \sigma_n \langle I^n \rangle = \sigma_n \left(\frac{\tau_l}{\tau_p} \right)^{n-1} \langle I \rangle^n \tag{3.8}$$

where the nonlinear cross-section σ_n decreases sharply with the order n of the nonlinearity. The easiest option to obtain higher-order signals efficiently and compensate for the reduced cross-section is to increase the average intensity $\langle I \rangle$ of the excitation. However, biological samples tend to be quite sensitive to this, limiting the maximum intensity that can be used before incurring photo-damage.

A more optimal approach is to reduce the laser duty cycle, increasing the ratio τ_l/τ_p by increasing the time between pulses τ_l or by decreasing the pulse duration τ_p. However, this approach has limitations as well. On the one hand, decreasing the pulse duration beyond a certain limit leads to a very broad laser bandwidth, introducing dispersion problems, as different wavelengths travel through the optical element at different speeds. On the other hand, due to the fact that in scanning microscopy the minimum number of pulse excitations per pixel is one, increasing the time between pulses reduces the maximum image acquisition speed. Specifically, the maximum pixel acquisition rate is τ_l^{-1}, which is the laser pulse repetition rate.

The microscope system used for this thesis employs the Cronus-3P laser developed by Light Conversion as the light source. This is an ultra-fast, infrared, pulsed laser that utilizes a pump beam operating at 1030 nm and an optical parametric amplifier (OPA) to produce tunable 50 fs pulses in the wavelength range $1250 - 1800$ nm.

An OPA is an optical system that utilizes difference frequency generation to produce a wavelength-tunable output starting from a fixed input [15]. In the case considered here, the 1030 nm pump beam, composed of pulses approximately 200 fs long, is fed into the OPA together with a second beam of the desired final wavelength. The nonlinear interaction then amplifies this second beam, along with the generation of a third new wavelength, following the process described in the previous chapter for DFG and partially depleting the pump. The new wavelength, in the mid-wavelength infrared region, is then

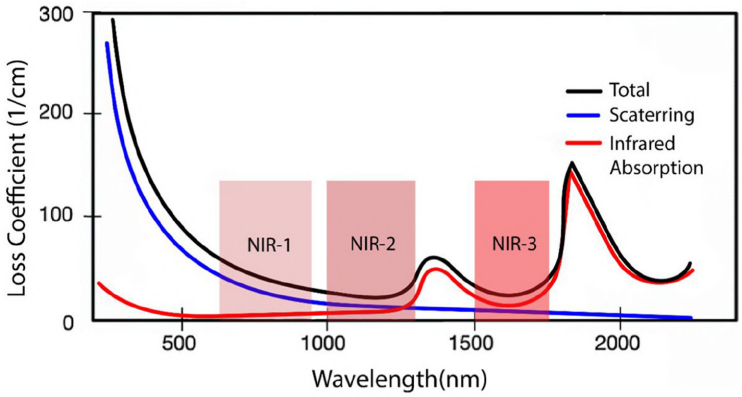

Figure 15: Extinction spectrum of water with the three near-infrared transparency windows highlighted. [11]

discarded, while the second beam, now amplified, passes through a compressor to reach the final duration of 50 fs.

Biological microscopy must account for the extinction coefficient of water, which is naturally present in almost all biological samples. The spectral profile of this coefficient presents different local minima, called water transparency windows, localized in the near infrared (NIR) domain. Biological multi-photon applications usually operate in the spectral range of the first transparency window NIR-I ($650 - 950$ nm). However, the wavelength range of the Cronus-3P laser is suitable for exploiting the next two transparency windows, which are located deeper in the infrared, specifically the NIR-II ($1100 - 1350$ nm) and NIR-III ($1600 - 1870$ nm). Although water absorption in these regions is comparatively higher than in NIR-I, the scattering efficiency is significantly reduced, and thus the overall light penetration in tissue is favored [4], as shown in Fig. 15.

Moreover, the repetition rate of the Cronus-3P laser is set to 1 MHz, which is an order of magnitude lower compared to standard microscopy applications. As previously stated, this allows for an increase in signal generation efficiency by reducing the duty cycle of the laser. This, together with the very short pulse duration of just 50 fs, gives a significant advantage to this system compared to other commercially available microscopy light sources.

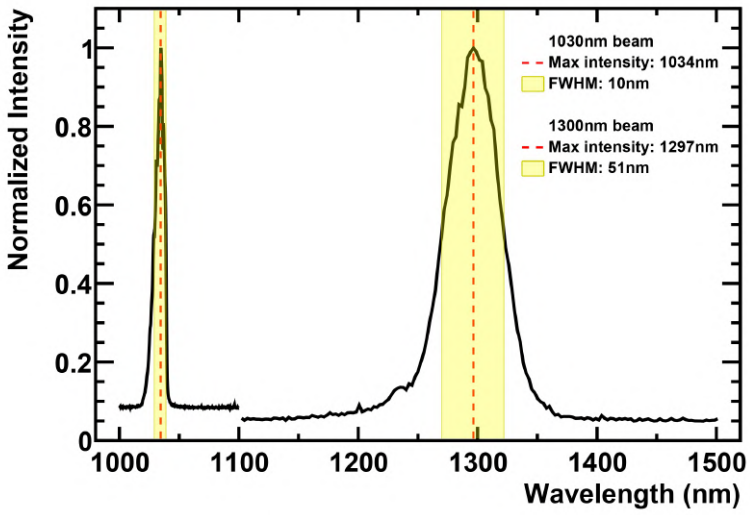

Figure 16: Spectra of the two laser beams used in the system, the dashed lines indicated the wavelength of maximum intensity and the highlighted area the FWHM spectral range.

Finally, crucial for the implementation of a frequency mixing protocol, this light source allows the extraction of part of the pump beam before it enters the OPA, effectively providing two compatible 1 MHz outputs: one fixed at 1030 nm with a $\sim$ 200 fs pulse length and the other tunable between 1250 − 1800 nm with a 50 fs pulse length. During the work on this thesis, the tunable output was always set to 1300 nm, at the center of the NIR-II transparency window, to best utilize the optical filters already present in the laboratory.

Before continuing with the description of the rest of the microscopy apparatus, it is appropriate to characterize the main properties of the two beams just introduced, namely their spectral and temporal profiles.

Spectral characterization

The spectral characterization of the two beams was conducted using a standard portable spectrometer and is reported in Fig. 16.

As stated before, the two pulses are expected to have a bandwidth inversely proportional to their duration. This is indeed the case, as the 1030 nm pulse

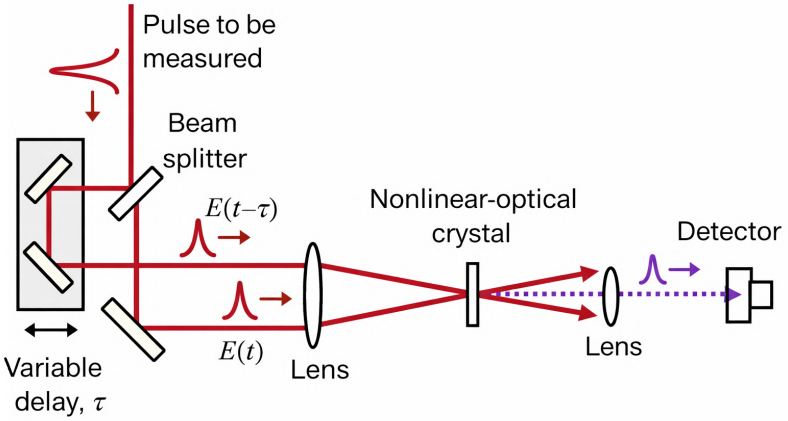

Figure 17: Schematic of the optical setup for an intensity autocorrelator. [17]

has a spectral full width at half maximum (FWHM) of (10 ± 5) nm, while the shorter 1300 nm pulse has a FWHM of (51 ± 5) nm. For both pulses, the maximum intensity was measured at a wavelength compatible with their nominal wavelength, namely (1034 ± 3) nm and (1297 ± 3) nm.

Temporal characterization

The temporal characterization of an ultra-fast pulse is not as easy as the spectral one. The common approach in this case is to perform an autocorrelation measurement.

The basic principle of operation of an autocorrelator for pulse duration measurement is to check the correlation of the temporal pulse trace with itself. To achieve this, a beam splitter creates two copies of the incoming pulses. These copies are then focused and superimposed in a medium with some χ^2 nonlinearity, where they interact, leading to an output with a shorter wavelength, provided that they reach the medium at the same time. The temporal overlap of the beam copies is adjusted by varying the path length of one of the two optical paths, usually via a tunable delay line. A schematic of the autocorrelation optical setup is shown in Fig. 17.

If the relative time delay is increased so that the overlap of the two pulses

in the crystal is reduced, the nonlinear mixing product becomes weaker. Obviously, that overlap is lost sooner if the pulses are rather short. To measure the pulse duration, the power of the mixing product is recorded as a function of the difference in arm length. The dependence of the autocorrelation signal on the temporal delay is given by [17]

$$A(\tau) = \int_{-\infty}^{+\infty} I(t)I(t+\tau)dt \tag{3.9}$$

where I(t) is the instantaneous optical intensity of the non delayed pulse copy at time t, and $I(t+\tau)$ is the same for the copy delayed by τ. Assuming a Gaussian pulse, the autocorrelation trace is also of Gaussian shape, with a width $\sqrt{2}$ times larger than the real temporal envelope of the pulse. An autocorrelation measurement requires many different pulses from a regular pulse train, since at least one pulse is needed for every time delay setting, and a range of those must be scanned. For this reason, it is assumed that all the pulses are identical and equally spaced.

The result of the autocorrelation measurement for the 1030 nm pulses is reported in Fig. 18 and gives a pulse duration of (199 ± 2) fs, which is compatible with the specifications declared by the laser manufacturer. Unfortunately, the 1030 nm pulse was outside the wavelength detection range of the detectors available for autocorrelation. For this pulse, the duration of 50 fs declared by the constructor is assumed to be true.

3.1.1 Group-delay dispersion compensation

Group-delay dispersion (GDD) quantifies the rate at which the group delay of optical wave packets changes as a function of frequency. When a laser pulse propagates through lenses, objectives, or other dispersive elements of the optical setup, each frequency component experiences a slightly different transit time due to the frequency-dependence of dispersion, so different spectral components do not arrive at the output simultaneously. This frequency-dependent delay turns the initially symmetrical pulse into a chirped one and typically stretches it in time, lowering the peak intensity even if the optical spectrum

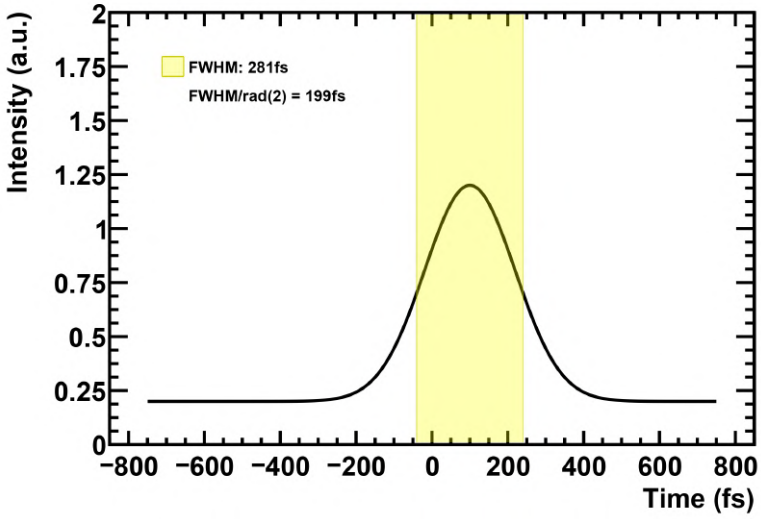

Figure 18: Autocorrelation plot for the 1030 nm pulse, the highlighted area indicates the FWHM that must be divided by $\sqrt{2}$ to obtain the real pulse duration.

remains essentially unchanged. The overall impact on the pulse duration grows rapidly with pulse bandwidth, so broadband femtosecond pulses are especially sensitive and tend to be dilated more. To preserve the pulse peak intensity at the sample plane, an initial negative GDD can be imposed to pre-compensate for the dispersion accumulated along the system, placing the most dispersed frequencies "in front" of the least dispersed ones before starting the propagation. In this way, the least dispersed frequency components can "catch up" with the others during propagation, due to the dispersion introduced by the system, allowing all frequency components to arrive at the sample simultaneously. This allows for the recovery of a shorter pulse at the sample plane, where the maximum peak intensity is needed to generate the signal.

Optical components capable of generating negative GDD are generally called compressors. The Cronus-3P laser utilized in this system has a tunable internal compressor just before the main tunable output, which can be used to pre-compensate for the dispersion from the rest of the optical system. The optimal value for GDD compensation is the one that gives the highest signal from

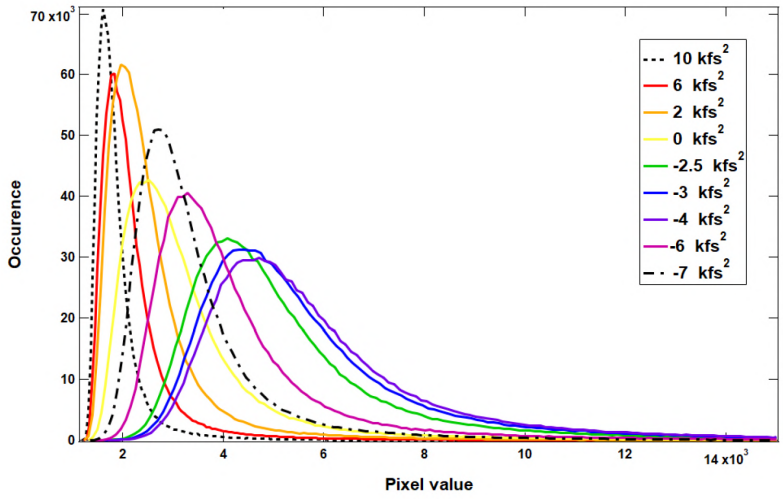

Figure 19: Pixel intensity histograms of SHG images of $BiFeO_3$ nanoparticles on coverslip from 1300 nm excitation for different GDD compression values, the highest signal intensity is obtained near $-4\,\mathrm{kfs}^2$ compression. Figure created by Alexandra Latshaw, courtesy of Bonacina Group at University of Geneva.

the sample, since it corresponds to the highest peak intensity at the sample plane.

The tuning of the GDD compression was already completed before the start of this thesis work by another member of the research group. The calibration was performed using the SHG and THG signals obtained from $BiFeO_3$ nanoparticles on coverslips excited with the 1300 nm beam. The images thus obtained for different GDD values are reported in Fig. 20. To find the GDD pre-compensation corresponding to the highest signal, it is useful to consider the pixel intensity histogram of each image. The histograms for the SHG signal are reported in Fig. 19 and show that the maximum intensity is obtained for GDD values between $-3\,\mathrm{kfs}^2$ and $-4\,\mathrm{kfs}^2$. In the end, the compression was set to $-3.6\,\mathrm{kfs}^2$.

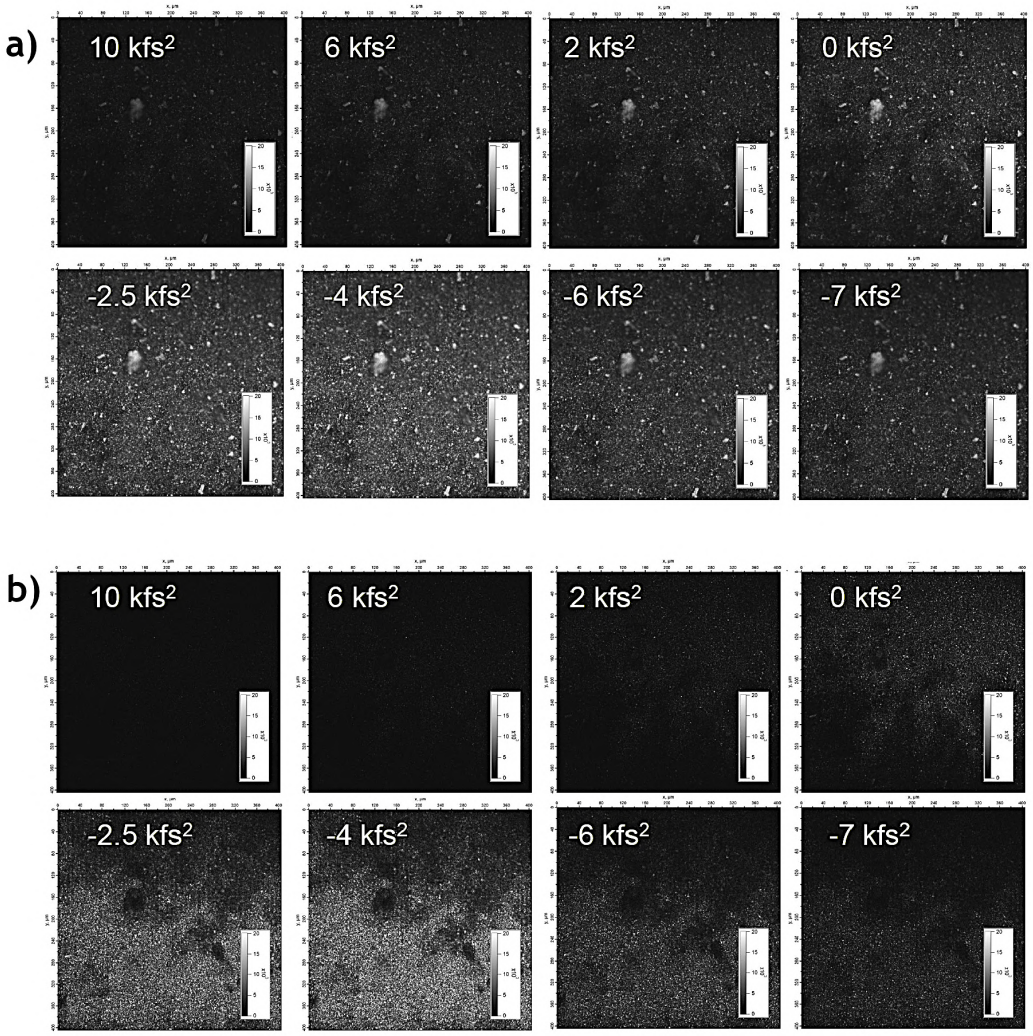

Figure 20: Images of $BiFeO_3$ nanoparticles on coverslip from 1300 nm excitation for different GDD compression values: (a) SHG signal at 650 nm, (b) THG signal at 433 nm. Images acquired by Alexandra Latshaw, courtesy of Bonacina Group at University of Geneva.

3.2 Optical Microscope System

Multi-photon nonlinear microscopes are a generalization of two-photon microscopes, first developed by Denk and Webb in 1989 [18]. Prior to the advent of nonlinear microscopy, confocal microscopes were the standard tool for three-dimensional imaging. From a technical standpoint, a multi-photon microscope is simpler than a confocal microscope, as it does not require a detection pinhole. This simplification arises because, owing to the nonlinear excitation process, the 3D voxel size in multi-photon microscopy is determined exclusively by the illumination optics of the microscope, whereas in confocal microscopy it depends on both the illumination and detection optics.

Also, these kinds of microscopes are usually scanning microscopes, meaning that the 3D image is acquired a voxel at a time by moving the focus position to scan the entire region of interest. For each scanning step, only the overall signal intensity is registered, so simpler single-pixel detectors can be used instead of full sensors with many pixels.

The advantages of nonlinear scanning microscopy become especially clear when imaging scattering samples, such as biological tissues. When laser light is focused into the tissue, some portion of it is inevitably scattered before it reaches the focal point. In conventional single-photon confocal microscopy, this scattered excitation light induces a signal outside the focal region of interest. Although most of this out-of-focus signal is blocked by the confocal pinhole, a fraction still reaches the detector, again aided by scattering, and thus increases the background signal. In contrast, in multi-photon microscopy, the background is largely suppressed because the scattered excitation light has a very low power density and is typically too weak to produce substantial out-of-focus signals. The higher the order of the nonlinear process, the smaller this unwanted background becomes.

Moreover, scattering does more than just increase background. Once signal light is generated within the focal volume, it too undergoes scattering as it travels through and exits the sample. In standard confocal microscopy, such scattering is problematic because it diverts photons away from the geometric path leading to the pinhole, preventing them from being collected and thereby

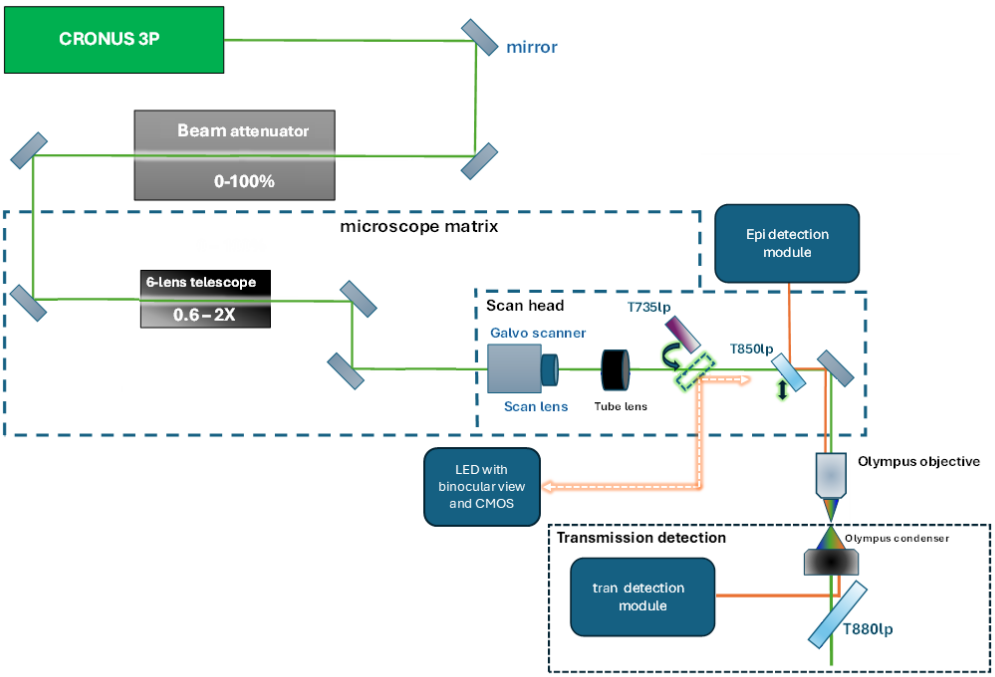

Figure 21: Schematic representation of the microscopy optical system used for this thesis, the green line represent the excitation beam while the orange one the signal light.

reducing the detected signal. By contrast, in multi-photon microscopy, this scattering has only a minor impact on the detected signal since no pinhole is used and the detector can collect almost all the light generated in the sample at each scanning step.

The schematic of the multi-photon nonlinear microscope used for this thesis, prior to the implementation of the frequency mixing protocol, is reported in Fig. 21. As for the light source, this system was also developed as a prototype within the framework of the FairCharm project in the laboratory of the University of Geneva.

As expressed in the previous section, the tunable beam, represented as a green line in the figure, exits the laser main output already GDD compensated, so it can reach the sample while maintaining its 50 fs duration. After exiting the laser, it passes through an attenuator to regulate power and a 6-lens telescope

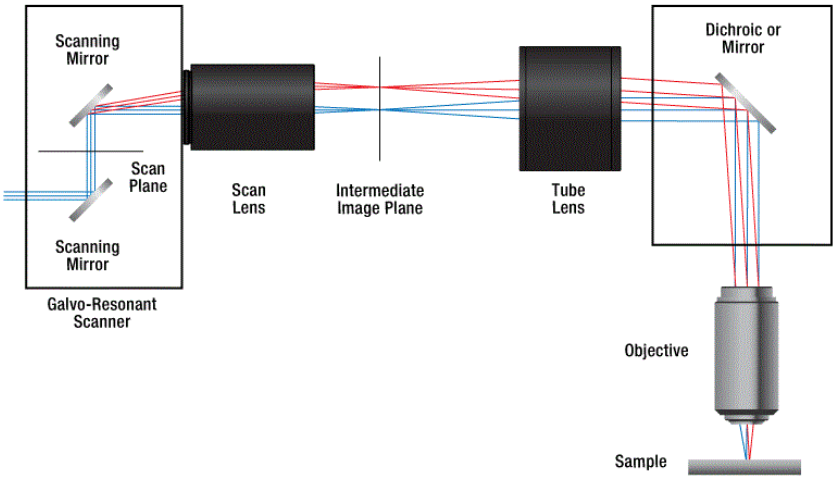

Figure 22: Schematic representation of the galvo scanner working principle, by turning the scanning mirrors is possible to move the position of the focus in the sample plane (blue and red lines).

that can change both its diameter and divergence. After that, it enters the scan head of the microscope, where a galvo scanner is responsible for the x-y plane scanning.

A galvo-scanner, reported schematically in Fig. 22, is a two-axis beam-steering module that uses two galvanometer-driven mirrors to deflect the laser beam in orthogonal directions. This allows the beam to be moved across the sample plane, thereby performing the scan. Scanning in the z direction is instead achieved by physically lowering or lifting the objective via a servo motor.

After the scan head, the beam enters the objective, where it is focused on the sample. The objective used in this microscope is an Olympus 25x infinity-corrected objective with a 1.05 NA, intended for use while submerged in water.

Inside the scan head, a 735 nm long-pass filter can be mechanically inserted into the beam line, allowing the injection of light from a secondary LED light source and the collection of the generated signal on a CMOS camera sensor or binocular view window. This is convenient during the placement of the sample, as it allows one to see the microscope view directly, bypassing the laser and the scanning module.

After the excitation, the signal light produced in the sample is separated from the laser light in both the forward and backward directions using two long-pass filters, 880 nm and 850 nm respectively. It is then collected by two detection modules: one for epi detection in the backward direction and one for tran detection in the forward direction. These modules are described extensively in the next section.

3.3 Detection Modules and Signal Acquisition

As stated above, in a scanning microscope, the image is formed by illuminating one point of the sample at a time and recording the intensity of the signal generated by each point as the beam is moved. The detectors typically used in this application are single-point detectors with no spatial resolution, and pixel values are created by synchronizing the registered scalar intensity with the scan position. This is different from classical non-scanning widefield microscopes, where the entire region of interest is illuminated in parallel, and the signal is detected simultaneously from many spatial locations using a camera sensor.

The microscope system used for this thesis is equipped with photomultiplier tubes (PMTs) as single-point light intensity detectors. PMTs convert the light signal into an electric signal by the photoemission of electrons inside a crystal window. The signal is then amplified by accelerating those electrons inside the tubes via a strong electric field, causing an avalanche emission of secondary electrons that are finally collected and measured as a current. The intensity of the final current is proportional to the number of original photoelectrons and therefore to the intensity of the initial light signal [19]. PMTs easily achieve high sensitivity with relatively low background noise, even at room temperature, making them particularly suitable for biological microscopy applications. The detectors used in this system are the H12056 modules produced by Hamamatsu, compact modules composed of both the PMT and its high voltage driving circuit.

Regarding the placement of such detectors, the fact that the nonlinear signal is predominantly forward directed, as shown in the preceding chapters, suggests that placing the detector after the sample, in the forward direction, is

generally optimal for measuring the coherent nonlinear signal. Unfortunately, this acquisition geometry restricts the technique to relatively thin and transparent samples. However, in thick or turbid samples, the initially forward-propagating nonlinear signal can be redirected backward by random linear scattering events within the medium. Remarkably, this redirection of the nonlinear signal is one of the few cases where scattering becomes advantageous for imaging, as the detector can now be positioned in the backward direction as well, thereby enabling coherent nonlinear imaging even in thick samples [16].

The system under study here is equipped with two macro detection modules, as shown in Fig. 21. The first is for epi detection, capable of detecting signals in the backward direction with respect to the laser beam, and it is schematically illustrated in Fig. 23. The signal light going back from the sample, at a shorter wavelength compared to the excitation beam due to the nonlinear effects, passes back through the objective and is filtered out from the laser line using a 850 nm long-pass filter. Due to the numerous nonlinear signals produced by the nonlinear interaction, four distinct PMTs modules are present inside the detection module. A series of filters and mirrors separate the signals and route each of them to a specific PMT. The filters can be manually swapped to change the set of detectable wavelengths, depending on the nonlinear interaction under study.

The second macro detection module is for transmission detection, in the forward direction, and is schematically depicted in Fig. 24. As this time the signal does not pass back through the objective, a condenser, manufactured by Olympus, is placed after the sample to de-focus and collimate the signal light that is initially generated coherently with the excitation beam. The remaining laser light is then filtered out using a 850 nm long-pass filter, and the signal light is separated into the wavelength components of interest, as in the epi detection case, and finally routed to two PMTs modules.

All PMTs in the system can be used simultaneously. Thus, depending on the characteristics of the samples, it is possible to detect up to six different nonlinear signals per acquisition: four in epi detection and two in transmission. This is particularly important for the frequency mixing implementation, as compared to standard harmonic microscopy, frequency mixing produces many

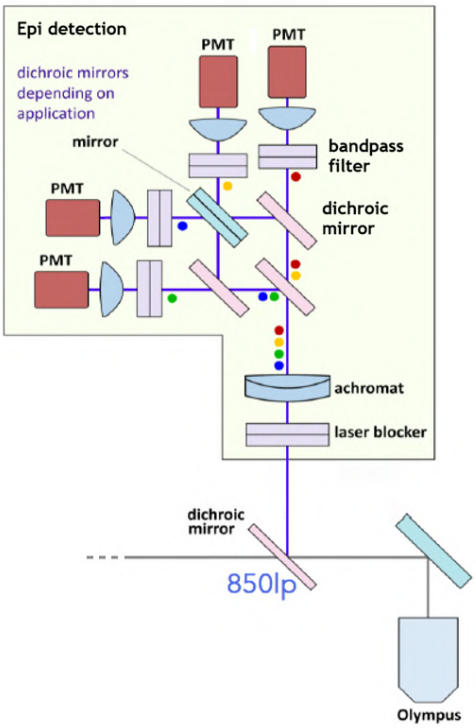

Figure 23: Schematic representation of the epi detection module used in the microscope for the detection of backward-propagating signal.

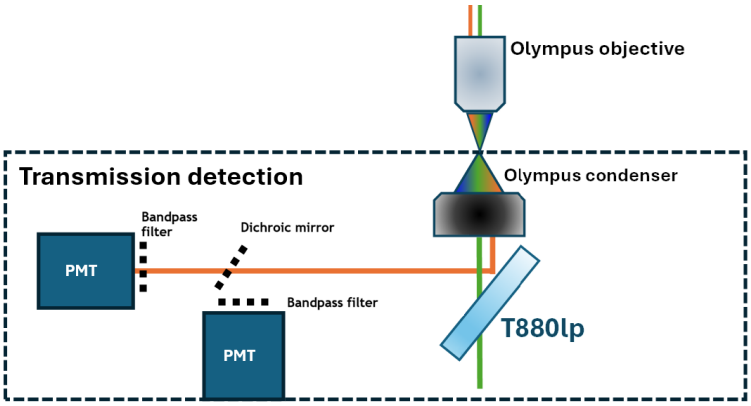

Figure 24: Schematic representation of the transmission detection module used in the microscope for the detection of forward-propagating signal, the green line represent the excitation beam while the orange one the signal light.

more signals at distinct wavelengths.

3.3.1 Monochromator Detector Module

Before the implementation of frequency mixing, the microscope was designed to work mainly with harmonic signals, SHG and THG, generated by the main tunable laser output. To account for the many new signals introduced by the frequency mixing, a new PMT detection module was design to integrate a manually tunable monochromator before the PMT, and was manufactured using a 3D printer. This new module, mounted inside the epi detection macro module in place of one of the already present PMTs, allows for changing the wavelength detected by the PMT on the fly, without the need to stop the acquisition to change the filters mounted on the microscope.

The possibility of acquiring all the generated signals on the same PMT, one by one, by manually operating the monochromator during a single acquisition is fundamental to characterizing all the signals obtained from the frequency mixing in a comparable manner.

The Monochromator used is a manual Mini-Chrom Monochromator produced by Edmund Optics, with a 1800 grooves/mm groove density and a 7.16 nm/mm linear dispersion. The monochromator operates with a $300 - 800$ nm range and a 30 nm bandwidth, perfect for detecting the nonlinear signals from the 1300 nm and 1030 nm beams. The design of the detection module is reported in Fig. 25.

3.4 Delay Line and Temporal Synchronization

As stated before, the purpose of this thesis is to implement a frequency mixing protocol into the pre-existing microscope system, which, up to this point, has mainly been used for harmonic nonlinear imaging. The aim was to combine the secondary 1030 nm fixed output of the laser, which was initially unutilized, with the main tunable output set to 1300 nm.

Due to the fact that the secondary beam is, in fact, part of the pump that generates the main one, it is guaranteed that both beams have the same pulse

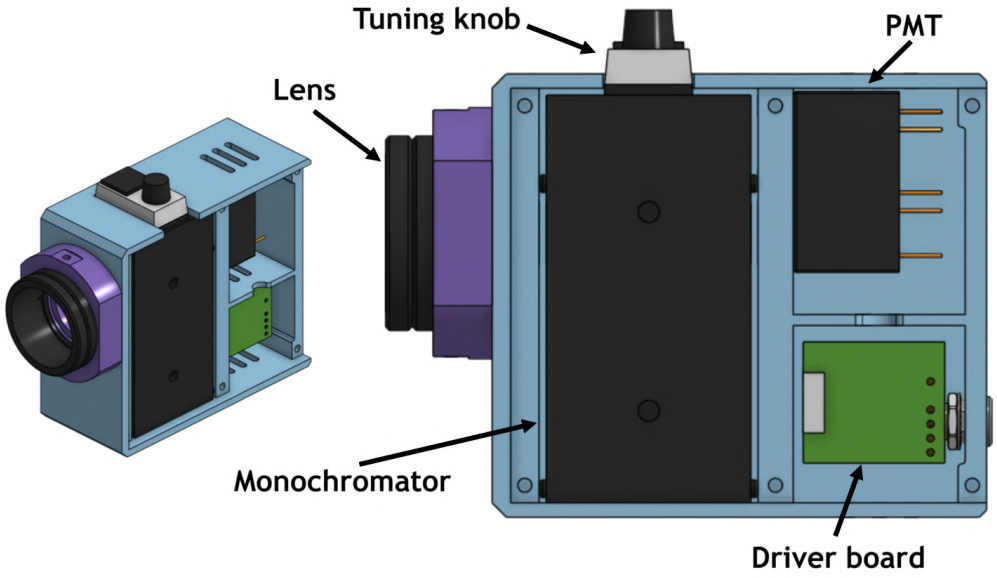

Figure 25: Design of the Monochromator-PMT detection module, the grating in the monochromator can be manually tuned to decide which wavelength reaches the PMT active area.

repetition rate. However, to have a nonlinear interaction between the two beams, it is necessary to superimpose their focus spots in the sample and to synchronize their pulses so that they arrive at the focus simultaneously.

The spatial overlap is easily obtained by merging the two laser lines before the scan head of the microscope using an appropriate long-pass filter. The temporal overlap is, however, more challenging, as the two pulses must arrive at the sample with at most $100fs$ between each other to have an efficient mixing interaction. Since the secondary beam exits the laser before the main one, it must be delayed to allow the other beam to catch up.

Before starting the design of the delay line, a rough estimate of the delay between the two beams as they exit the laser was taken using a photodiode connected to an oscilloscope. The measured delay was (19 ± 1) ns, meaning that the delay line for the fixed beam should be around (5.70 ± 0.30) m long. Moreover, to allow fine tuning of the delay, it is necessary to include in the delay path a tunable segment that allows for adjustment of its length.

The fixed part of the delay line was obtained by routing the beam multiple

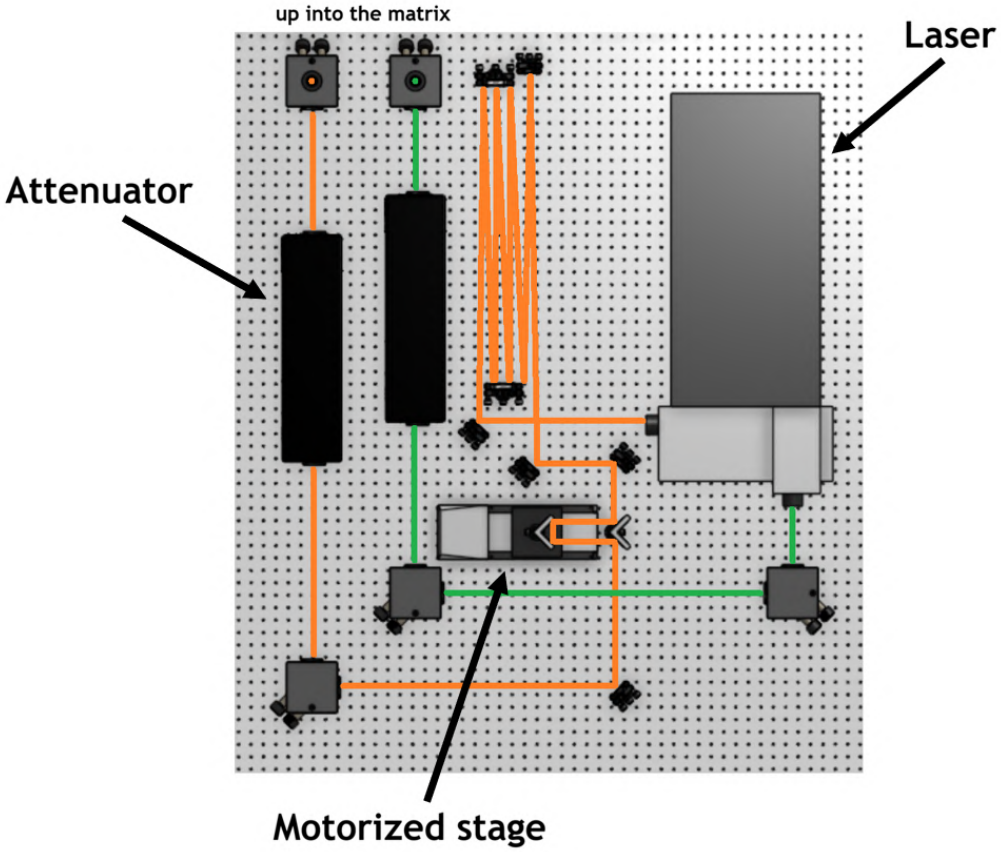

Figure 26: Schematic model of the optical table with the realized delay line, the orange line represent the secondary beam while the green one represent the main beam.

times across the optical table using a series of laser-line mirrors. The mirrors were selected to preserve as much of the beam power as possible. The tunable part was instead realized using a motorized stage with two right-angle mirrors mounted on top, forming a simple retro-reflector. A schematic model of the realized delay line is reported in Fig. 26, showing the path of both the main and secondary beams.

The motorized stage is a linear positioning stage produced by Physik Instrumente, with a 10 cm range and a 0.25 µm step resolution, which means that it allows control of the delay between the two beams with a sub 2 fs resolution.

After the delay line, the secondary beam passes through an attenuator, as

is the case for the main beam. The two distinct attenuators allow independent control of the power of the two beams, making it possible to match their intensity at the sample. After the attenuators, both beams are routed into the matrix, where the two lines are spatially overlapped before going through the scan head to be focused onto the sample.

3.4.1 Frequency mixing cross-correlation

Once the installation of the delay line was completed, and after careful tuning of the pulse synchronization to obtain the mixing interaction, it was possible to test the workings of this new detection protocol by acquiring the new signals introduced by frequency mixing.

To do this, a test sample of a strong nonlinear medium deposited on a coverslip was used. All signals were acquired from the same isolated nanoparticle using the monochromator detection module, described in the previous section, to keep them comparable. The wavelength passing through the monochromator was changed on the fly during the acquisition to collect all signals in rapid succession and without changing other parameters. To verify the mixing nature of the signals, a scan of the linear stage was performed, thus changing the delay between the two beams and acquiring images at fixed delay steps.

The mixing signals considered are the second- and third-order sum frequency generations, at 575 nm and 399 nm respectively. The third-order mixing specifically refers to the signal obtained by the combination of two photons at 1300 nm and one at 1030 nm. Ideally, many other third-order signals could be obtained, both for sum frequency and difference frequency generation, with wavelengths in the UV or IR; however, the optics transmittance and detector sensitivity drop significantly in those regimes, making those signals difficult to detect. Therefore, for now, only the two aforementioned signals were considered for the mixing. In addition to the mixing signals, some standard harmonic signals were acquired, specifically the SHG and THG from the 1300 nm beam, respectively at 650 nm and 433 nm, and the SHG from the 1030 nm beam at 515 nm. As before, the THG signal from the 1030 nm beam was not considered as its wavelength is too short to be efficiently detected by the system.

The images acquired using this protocol are reported in Fig. 27. From them, it is possible to see how the mixing signals tend to vanish when the temporal delay between the two pulses increases over 100 fs, as expected, while the harmonic signals remain constant as they originate only from one beam and are therefore not influenced by the delay.

It is possible to plot the intensity of the signals depending on the delay between the beams, as reported in Fig. 28. The intensity difference between second- and third-order signals depends on the nature of the sample and is not interesting for current analysis. However, recalling the notions of the first chapter, specifically Eqs 1.10 and 1.11, the mixing signal is expected to be four times more intense than the same-order harmonic signal. This is indeed not the case, as can be verified from the graph, where for each order the harmonic signals appear more intense than the corresponding mixing ones. This unexpected behavior is probably caused by poor spatial overlap of the foci of the two beams, which decreases the overall efficiency of the mixing processes without affecting the harmonic ones. Indeed, the spatial alignment of the two beams is very sensitive and must be fine tuned before every acquisition.

The FWHM of the mixing signals intensity profile can, in theory, provide information about the true pulse duration. The concept is similar to the one explained before for autocorrelation, with the only difference being that now it is a delay-dependent cross-correlation trace between two distinct beams instead of between two copies of the same beam.

Considering the second-order SFG mixing signal, its intensity trace is a convolution of the instantaneous intensity of the two beams over time, depending on the relative delay between them, following the expression

$$I_{SFG}(\tau) = \int_{-\infty}^{+\infty} I_1(t) I_2(t+\tau) dt \tag{3.10}$$

where I_1 is the instantaneous intensity of the 1300 nm beam and I_2 is the instantaneous intensity of the 1030 nm beam. This expression is equivalent to the one in Eq. 3.9 for the autocorrelation signal, but now each intensity refers to a different beam and wavelength.

Assuming that all the pulses are gaussian shaped, the FWHM of the cross-

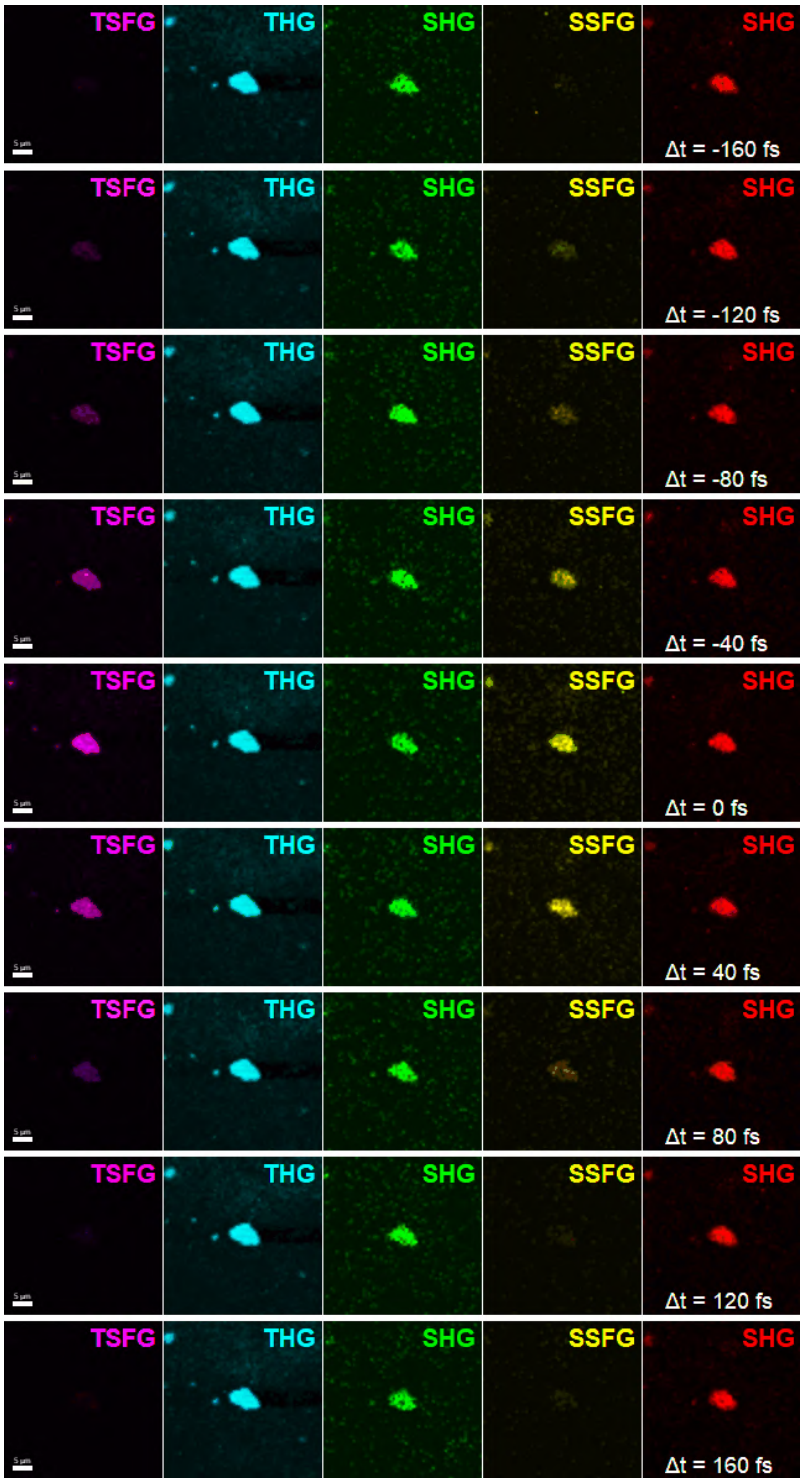

Figure 27: Series of images of the same Li_2NiO_4 nanoparticle acquired at different delays and representing different signals; from left to right the wavelengths are 399 nm, 433 nm, 515 nm, 575 nm, 650 nm; the white scale bar on the left correspond to 5 µm. Graphic realized by Alexandra Latshaw.

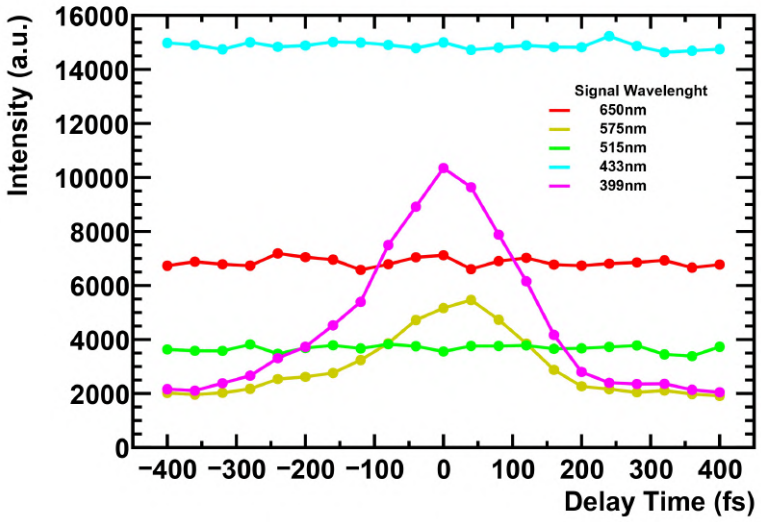

Figure 28: Graph representing signal intensity respect to delay between the pulses for different harmonic and mixing nonlinear signals.

correlation trace depends on the FWHMs of the two excitations as

$$FWHM_{SFG}^2 = FWHM_1^2 + FWHM_2^2 \tag{3.11}$$

where it can again be observed that when the two beams are the same, the cross-correlation FWHM became $\sqrt{2}$ times wider than that of the beam, as expected from the autocorrelation case.

In practice, it is very difficult to obtain a reliable description of the temporal profiles using these methods, as different pulse shapes can lead to similar cross-correlation traces. Moreover, the longer duration of the 1030 nm pulse tends to dominate in Eq. 3.11, hiding the shorter 1300 nm pulse. Thus, in this case, even in the best scenario, only an estimate of the duration of the longer pulse can be obtained from these data.

3.4.2 Compression of the second beam

An option to enhance the mixing signal is to increase the peak intensity of the secondary beam by shortening its longer pulse duration. Since this beam exits

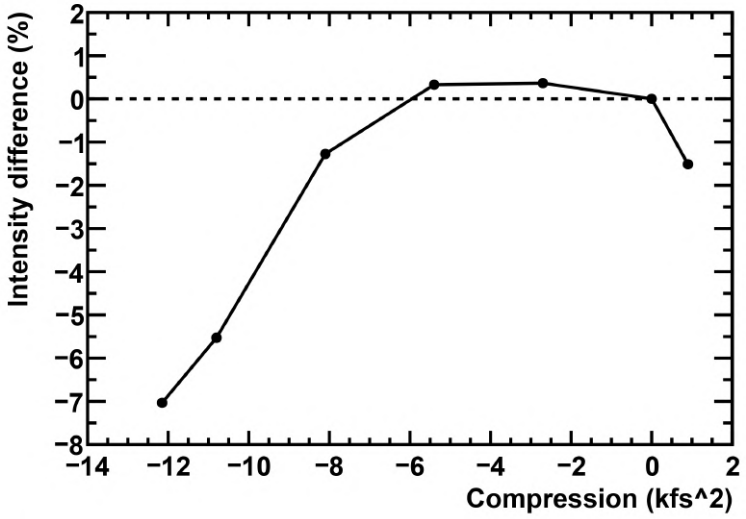

Figure 29: Graph representing the signal intensity variation respect to the GDD pre-compensation, expressed as a percentage respect to the zero compression case.

the laser prior to the internal compressor, it is, in principle, possible to shorten its duration at the sample plane by introducing some GDD pre-compensation via an external compressor placed along the delay line. However, the relatively narrow spectral bandwidth of the pulse, on the order of only 10 nm, makes it intrinsically less sensitive to GDD. As a result, the dispersive components in the optical path may be insufficient to induce a significant temporal compression of the pulse.

To explore this approach regardless, a standalone BOA pulse compressor module produced by Swamp Optics was mounted at the beginning of the delay line, and the signal intensity generated at the sample was registered for different compression values. The results are reported in Fig. 29.

From the graph, it is possible to see how the maximum signal intensity, related to the maximum pulse peak power and therefore to the minimum pulse duration, is found for a compression value between $-3\,\mathrm{kfs}^2$ and $-4\,\mathrm{kfs}^2$. This is consistent with the ideal value of $-3.6\,\mathrm{kfs}^2$ already found for the main beam, as expected, since the two beams pass through more or less the same optical

elements.

However, even at its maximum value, the intensity enhancement achieved through compression is only approximately 1% higher than in the case without compression, owing to the limited spectral bandwidth of the pulse that reduces the effect of GDD. Moreover, transmission through the pulse compressor reduces the beam average power by roughly 30%. For these reasons, the compressor was removed from the system, as the combined effect of modest pulse shortening and substantial power loss ultimately leads to a reduction in overall signal intensity.

4. System Operation and Imaging Experiments

Following the successful implementation of the new frequency-mixing protocol into the existing acquisition system and the comprehensive characterization of its performance, as described in the preceding chapter, the setup is now suitable for the imaging of real samples.

As stated in the introduction, the ultimate objective of this study is to enhance the selectivity of the system and to expand its explorable parameter space by broadening the spectrum of accessible signals through the utilization of wave-mixing effects.

In this chapter, the images obtained by applying the developed system to both inorganic and organic samples will be presented and discussed.

4.1 Harmonic Nanoparticles

Harmonic nanoparticles (HNPs) are nanoparticles capable of producing nonlinear optical signals, usually formed from metal oxide non-centrosymmetric nanocrystals. Such crystals lack an inversion symmetry center and therefore present an efficient second-order nonlinear response [20]. Moreover, their third-order nonlinear response has been shown to be directly related to the second-order one [21]. The magnitude of the nonlinear susceptibility depends on the nature of the material, with efficient materials for harmonic generation commonly presenting large band gaps to avoid re-absorption of the generated wave [4]. Moreover, since the nonlinear response comes from the bulk of the nanocrystal, unlike other types of metallic nanoparticles, such as plasmonic ones, where it is a surface effect, the signal from HNPs scales with the volume of the particles as V^2 [20].

A particularly notable characteristic of HNPs is their minimal sensitivity to

the excitation wavelength. In fact, unlike bulk nonlinear materials, they are not subject to phase-matching constraints, as the nanocrystal size is much smaller than the coherence length of the radiation. Due to this, signals generated at different points inside a particle do not interfere destructively with one another, making HNPs adaptable to a wide range of excitations [20].

In nonlinear bioimaging applications, harmonic nanoparticles are commonly adopted as labels due to their strong nonlinear response and high photostability. Compared to standard fluorescence labels, the fact that nonlinear signals do not involve resonant transitions makes HNPs largely resistant to photobleaching. Moreover, the multi-order nonlinear response of HNPs is preserved even when the particles are embedded inside biological samples [21]. However, the yield of nonlinear processes is lower compared to fluorescence sources, so the nanoparticle size needs to be larger to obtain a sufficiently strong signal, possibly affecting the biological processes under study [4].

4.1.1 Lithium Niobate Nanoparticles

Lithium Niobate $LiNbO_3$ (LNO), a perovskite, is known for its particularly high nonlinear susceptibility and is therefore commonly used to produce HNPs for nonlinear imaging applications [4].

In Fig. 30, some images obtained from LNO nanoparticles of around 160 nm in size using the developed system are reported. As in the previous chapter, to account for the optics transmittance and detectors sensitivity, only the second- and third-order SFG mixing signals, at 575 nm and 399 nm respectively, were acquired; together with SHG and THG (650 nm and 433 nm) from the 1300 nm beam and SHG (515 nm) from the 1030 nm beam. All signals were acquired at the same time using a combination of the detectors available in the system, described in the previous chapter, in both forward and backward directions, since the signal from HNPs is intense enough to allow for easy detection in both directions.

This time, instead of scanning the delay between the two beams, two additional acquisitions were performed after the initial one, first turning off the 1030 nm beam and then the 1300 nm one. In this way, by checking when each

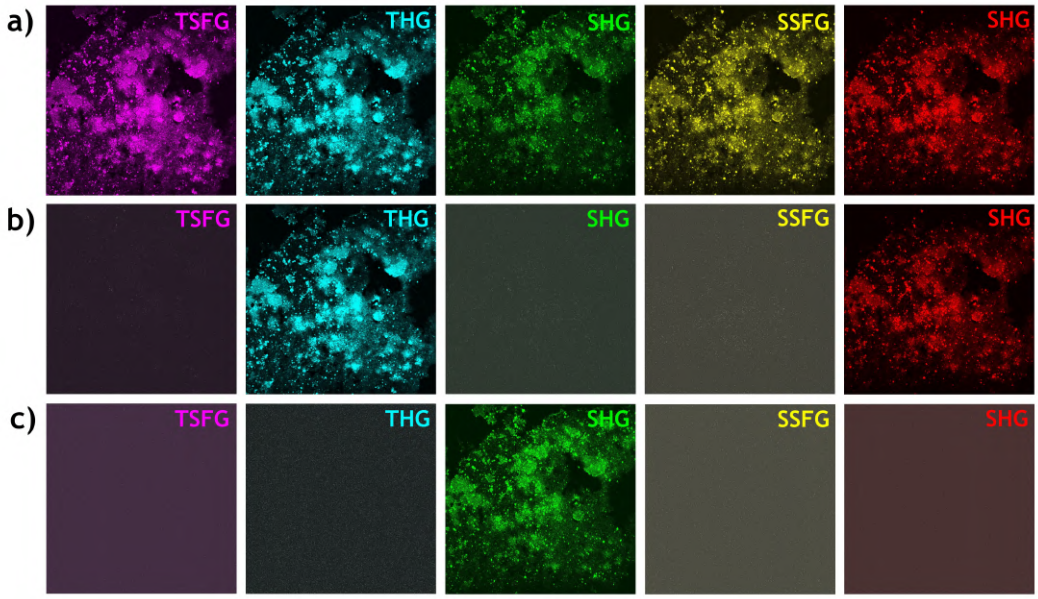

Figure 30: Series of 200x200 µm images of 160 nm LNO nanoparticles on coverslip, each column represents a different signal; from left to right the wavelengths are 399 nm, 433 nm, 515 nm, 575 nm, 650 nm; (a) acquisition performed with both beams on, (b) acquisition performed with the 1030 nm beam off, (c) acquisition performed with the 1300 nm beam off.

signal disappears, it is possible to determine from which specific excitation beam each signal originates. All signals behaved as expected, as can be seen from Fig. 30, where the mixing signals in particular disappear when either one of the beams is off.

4.1.2 Breast Cancer Cells with LNO nanoparticles

HNPs are commonly used as nonlinear labels in biological systems. In this case, a culture of breast cancer cells infused with LNO nanoparticles was imaged. The NPs get adsorbed by the cellular membrane and can be used to identify and segment the various cells.

Only the second-order SFG (575 nm) and the two SHG (515 nm and 650 nm) signals were acquired. This time, instead of turning off the beams, a second acquisition was performed with both beams still on, but with the delay between

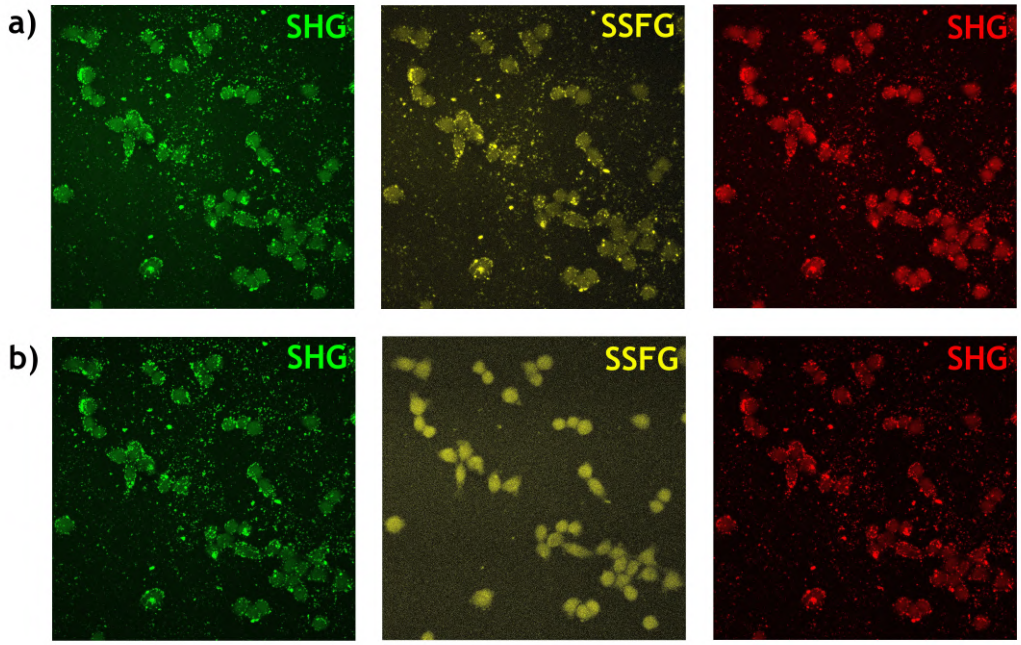

Figure 31: Series of 200x200 µm images of breast cancer cells on petri dish infused with LNO nanoparticles, where each column represents a different signal; from left to right the wavelengths are 515 nm, 575 nm, 650 nm; (a) acquisition performed with temporal overlap between the two pulses, (b) acquisition performed with no temporal overlap between the two pulses.

the two pulses substantially increased so as to avoid any temporal overlap and beam-beam interaction. In this way, it is possible to selectively exclude only the signals that originate from the mixing between the two beams, without changing the stimulus that the sample receives. The images obtained are reported in Fig. 31.

It can be seen that, for each frequency channel, the signal originates from both the nanoparticles, which appear brightest in the images, and the cell volumes. More importantly, the signal from the cell volumes remains visible in the mixing channel even when the two pulses are not temporally synchronized and no mixing signal is expected. The comparison between the signal at 575 nm acquired in the mixing channel for the two acquisitions is reported in Fig. 32. The permanence of signal in the mixing channel indicates that the emission

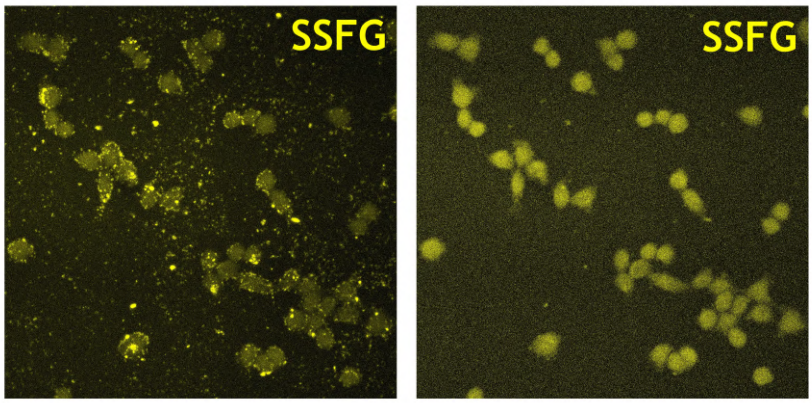

Figure 32: Comparison of the signal acquired in the mixing channel at 575 nm for the two pulses temporally synchronized (left) and not temporally synchronized (right).

from the cell volumes is probably due to auto-fluorescence. In fact, both the two-photon fluorescence spectrum from the 1030 nm beam and the three-photon fluorescence spectrum from the 1300 nm beam overlap with the SFG mixing signal at 575 nm.

Being fluorescence a resonant, nonparametric process, its emission spectrum is far broader than those of the parametric nonlinear interactions treated until now. For this reason, and due to the fact that the integration of a second beam for the mixing protocol has increased the number of generated signals, which are now less spectrally separated than before, it is important to be aware of possible signal contamination and light leaks from undesired fluorescence excitations when imaging biological samples.

To mitigate this issue, one possibility is to use very narrow band-pass filters in the acquisition channels, centered on the desired harmonic or mixing signal frequency, so that most of the fluorescence signal is filtered out, but with the drawback of losing some signal intensity. Another possibility is to acquire a background image using the two beams without temporal synchronization, as was done here. This solution preserves all the signal, but is applicable only to mixing signals that are influenced by pulse synchronization.

4.2 Biological Samples

A key property of nonlinear signals for bioimaging applications is that they can originate directly from the biological samples without the need to rely on HNPs or other labeling techniques. As stated in the previous chapters, second-order nonlinear signals originate from non-centrosymmetric molecules packed in organized structures, mainly collagen and myosin fibers, whereas third-order signals tend to originate from cellular interfaces or water-lipid solutions.

Furthermore, it has been demonstrated very recently that frequency-mixing signals acquired from live specimens can be employed to probe blood oxygenation in a fast and non-invasive manner. This capability arises because the ratio between third-order SFG and THG signals is sensitive to the oxygenation state of hemoglobin, owing to resonant interactions with its electronic energy levels [22].

However, due to the limited time available for this work, the focus was directed mainly at testing the developed mixing protocol on different samples, comparing the newly accessible mixing signals with the harmonic ones. In the following, the images acquired from three different unstained biological samples will be presented and discussed.

4.2.1 Mouse Heart Muscle

Muscle tissue from a mouse heart fixed on a petri dish was imaged, looking at both harmonic and mixing signals. Due to the nature of the sample, a strong second order nonlinear response is expected from the muscle myosin fibers.

Two acquisitions were performed: the first collected the second-order SFG (575 nm) and the two SHG (515 nm and 650 nm) signals, while the second, on a different section of the sample, investigated the third-order SFG (399 nm), DFG (853 nm), and THG (433 nm) signals. The DFG signal, in particular, is at the limit of the detectors' sensitivity range. The images obtained are reported in Fig. 33

As expected, the second-order signals are far more intense than the third-order ones. To obtain a strong enough signal from the third-order channels,

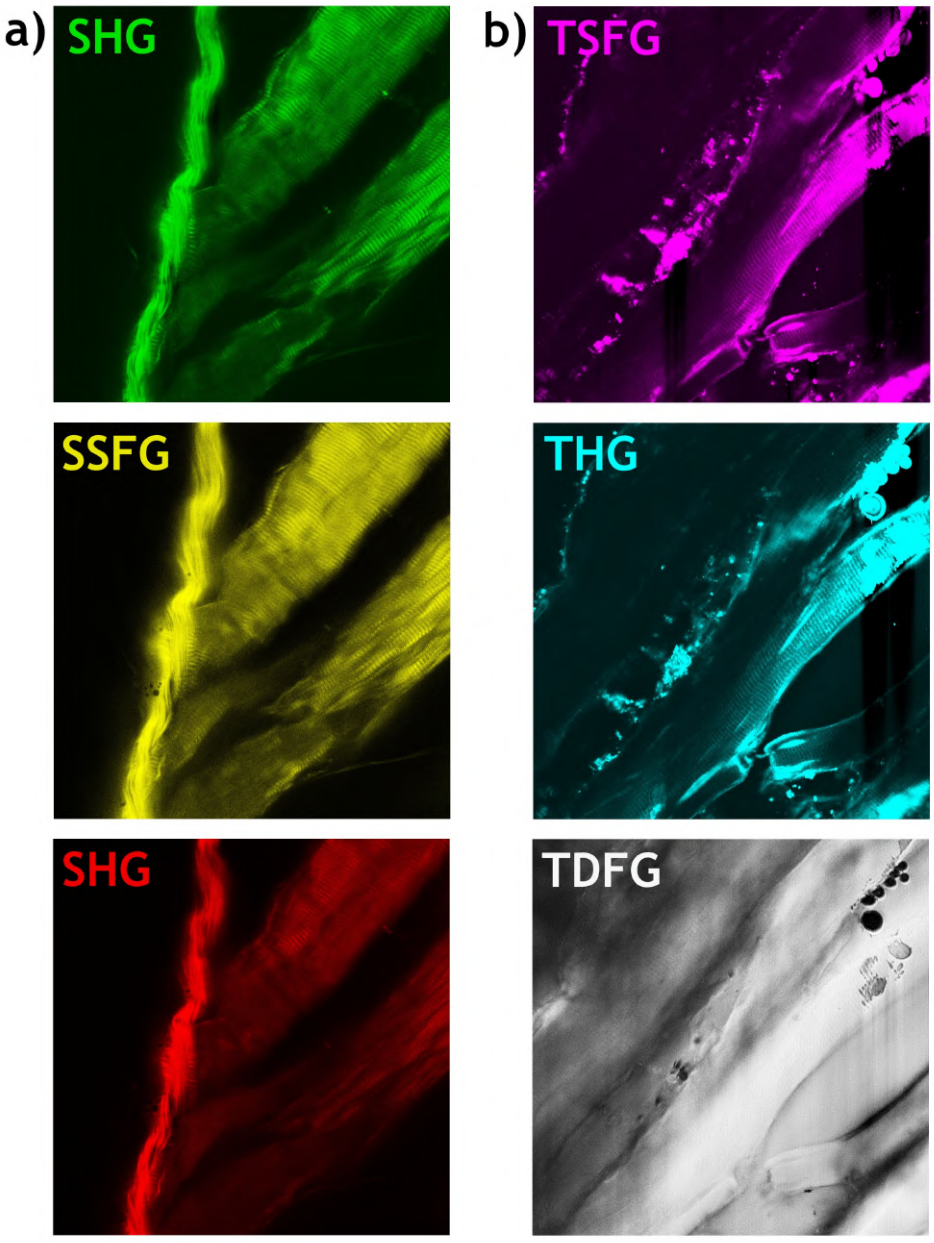

Figure 33: Series of 200x200 µm images of mouse heart's muscle tissue on petri dish; column (a) second-order signals at wavelengths 515 nm, 575 nm, 650 nm from top to bottom, column (b) third-order signals at wavelengths 399 nm, 433 nm, 853 nm from top to bottom.

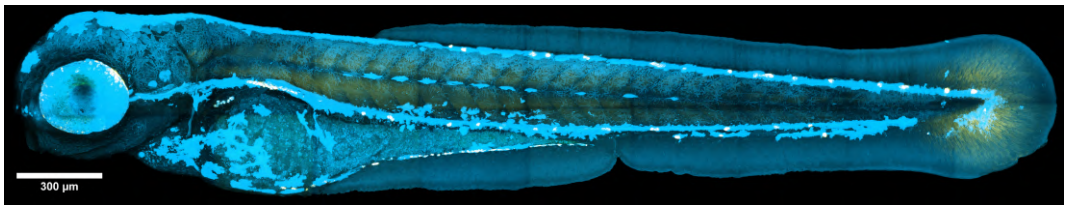

Figure 34: Image of a zebrafish larva obtained from 1300 nm excitation, the THG signal is displayed in blue and the SHG signal is displayed in yellow, the white scale bar on the left correspond to 300 µm. Images acquired by Thomas Kraehenbuehl, courtesy of Bonacina Group at University of Geneva.

the average power of the two laser beams was raised, ultimately resulting in photo-damage to the sample. In fact, it is possible to observe bubbles in the top-right corner of the images in column (b) of Fig. 33, resulting from the thermal effect of the laser on the sample.

4.2.2 Zebrafish Larvae

Zebrafish are commonly used in microscopy research because they are transparent, can be easily labeled, and there are many different genetic strains that can be sourced. A complete image of a zebrafish larva, obtained with the same microscope used in this thesis, but before the implementation of frequency mixing, is reported in Fig. 34 as a reference.

Since zebrafish larvae are highly transparent, only signals in the forward direction can be acquired, limiting the acquisition to two channels. For this reason, only second-order SFG (575 nm) and SHG (650 nm) were acquired, in order to compare the efficiency of the two signals. In fact, as expressed many times in the first chapter, under ideal conditions the mixing signal is expected to be four times more intense than the harmonic one, since it derives from two different beams.

Different parts of the larva were imaged. In Fig. 35, a section of the dorsal muscles is shown, where most of the second-order signal comes from the muscle fibers. In Fig. 36, an image of the tail fin is presented, and this time the signal is generated mainly from the collagen structures that form the fin.

As expected, the images from the mixing channel appear brighter and more

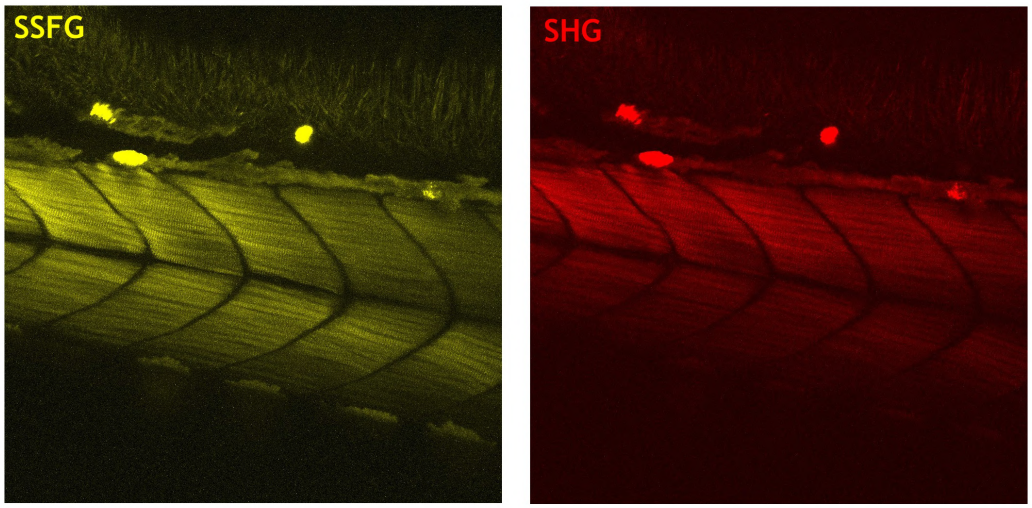

Figure 35: Images of zebrafish larva's dorsal muscles respectively at 575 nm (left) and 650 nm (right); each image is 380x380 µm.

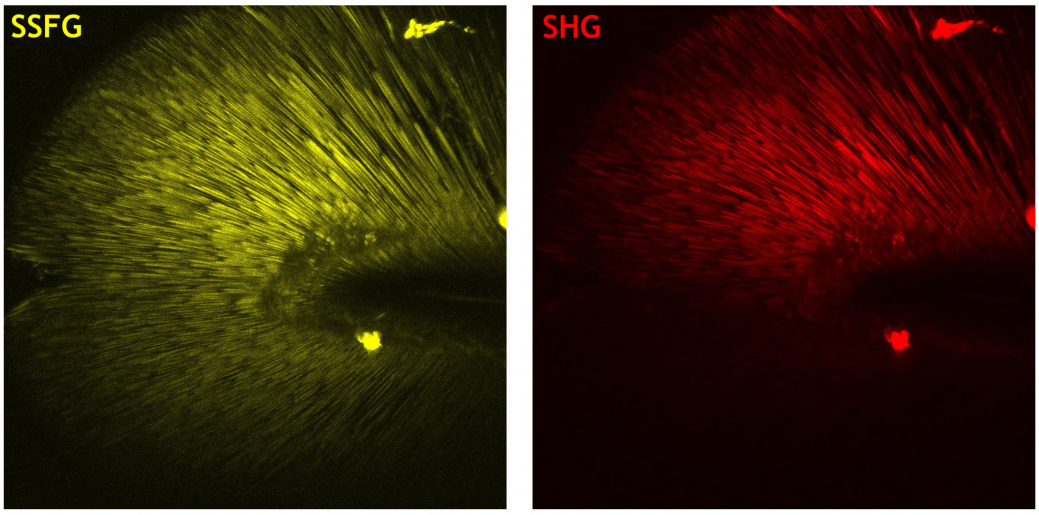

Figure 36: Images of zebrafish larva's dorsal fin respectively at 575 nm (left) and 650 nm (right); each image is 380x380 µm.

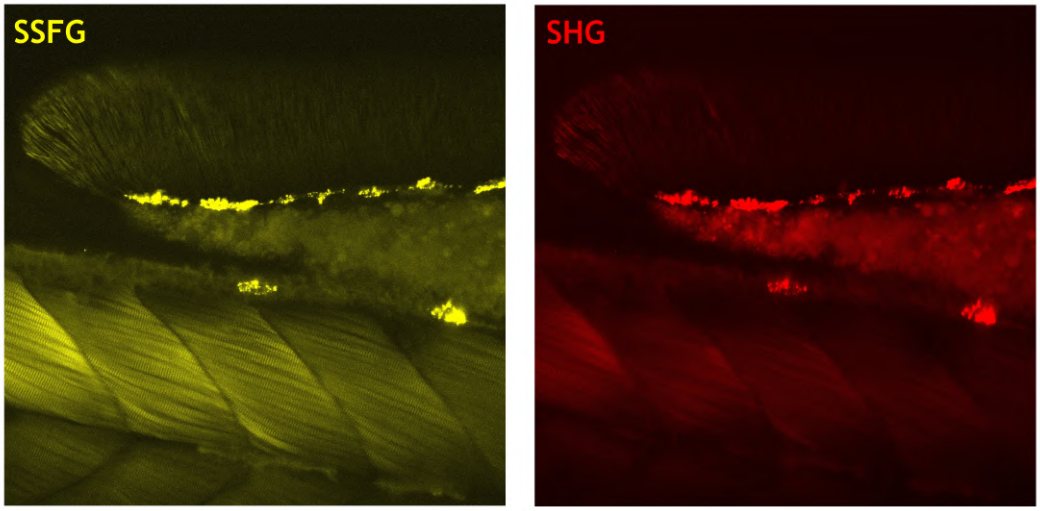

Figure 37: Images of zebrafish larva's dorsal muscles and yolk sac respectively at 575 nm (left) and 650 nm (right); each image is 380x380 µm.

defined compared to those from the SHG channel, because of the higher intensity of the mixing processes in comparison to standard harmonic emissions.

Images from another section of the larva are shown in Fig. 37. In this case, in the top part of the frame it is possible to observe the last section of the yolk sac, just above the dorsal muscles. Interestingly, this structure appears to be brighter in the SHG 650 nm channel, as can be seen more easily in Fig. 38, where the two channels are superimposed. As before, this discrepancy in the detected signal is most likely attributable to two-photon auto-fluorescence generated by the 1030 nm excitation, whose emission spectrum overlaps with that of the SHG signal produced by the 1300 nm beam.

4.2.3 Arabidopsis Thaliana Seeds

Arabidopsis thaliana, commonly known as mouse-ear cress, is a small plant widely spread across many continents and is commonly considered a weed. It is a popular model organism in plant biology and genetics, as it was the first plant to have its genome sequenced and is an important tool for understanding the molecular biology of many plant traits. Its seeds, usually less than half a

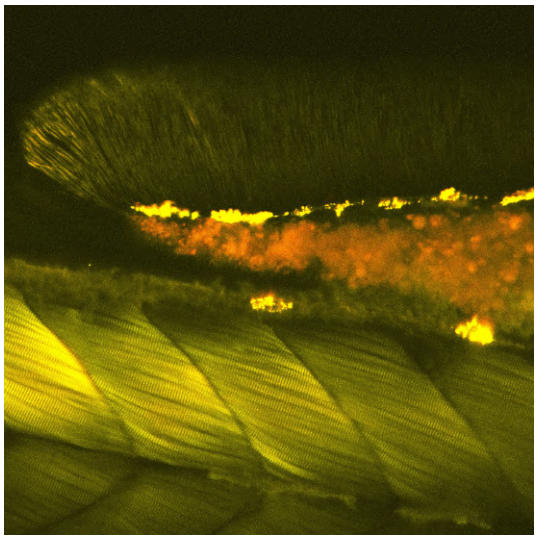

Figure 38: Image of zebrafish larva's dorsal muscles and yolk sac obtained by superimposing the two acquisition channels shown in Fig. 37; SFG at 575 nm is displayed in yellow and SHG at 650 nm is displayed in red.

millimeter in size, have been imaged inside a water solution with the aim of reconstructing how their surface changes when exposed to humidity, as in the first steps of the plant life cycle.

A three-dimensional scan of the seeds was performed by composing multiple images taken at different positions on the z-axis, acquiring for each image the second- and third-order nonlinear sum frequency signals at 575 nm and 399 nm, and the second- and third-order harmonic signals from the 1300 nm beam at 650 nm and 433 nm. It was thus possible to compare the results obtained from the mixing signal with the standard harmonic ones. Due to the thickness and opacity of the sample, this time all signals were acquired in the backward direction. In Fig. 39, 3D renders of the same seed obtained from the two second-order channels are reported, while Fig. 40 reports the 3D renders for the third-order signals.

Unlike previous cases, this time the harmonic channels give a sharper and more contrasted image, particularly for the second-order signals. This is probably caused by a resonance effect between the energy levels of the sample and the 1300 nm excitation, which specifically enhances the harmonic signals.

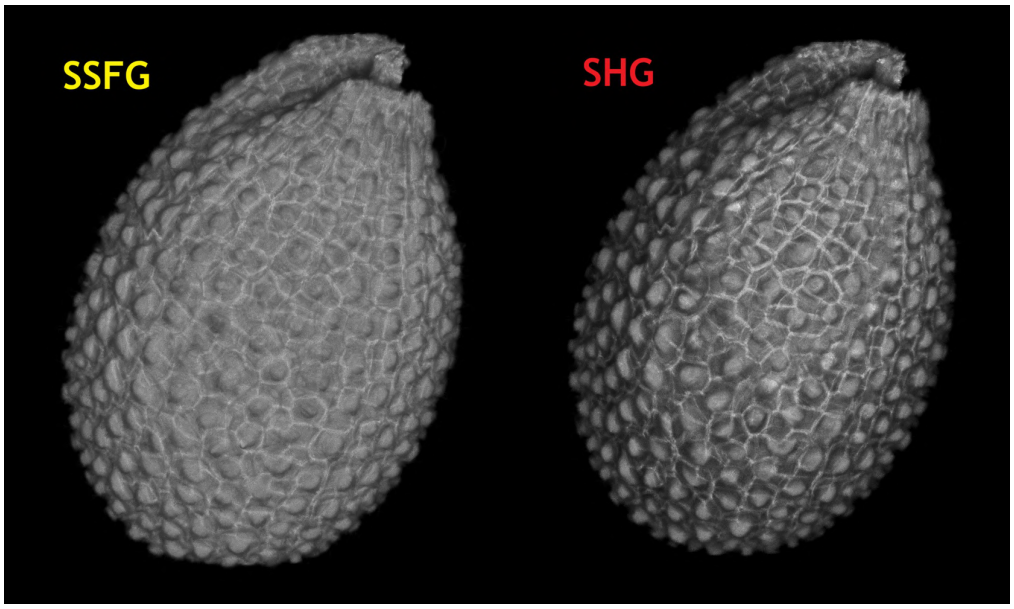

Figure 39: Three dimensional renders of a arabidopsis thaliana seed obtained from second-order mixing and harmonic signals at 575 nm (left) and at 650 nm (right); each image is 400x400 µm.

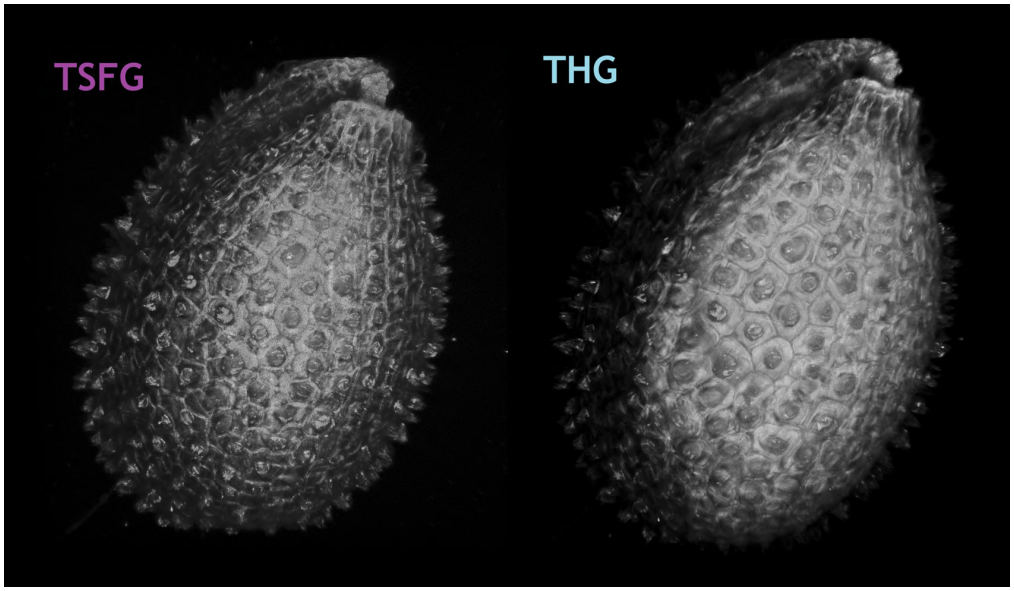

Figure 40: Three dimensional renders of a arabidopsis thaliana seed obtained from third-order mixing and harmonic signals at 399 nm (left) and at 433 nm (right); each image is 400x400 µm.

4.3 Images Analysis and Post-Processing

The numerous additional frequency components generated by nonlinear mixing can be exploited to extract further information from the samples, thereby enhancing the overall selectivity of the imaging system. In fact, although both harmonic and mixing signals arise from the same microscopic structures within the sample, depending on their nonlinear order, their generation efficiencies can differ due to the specific energy levels and resonances of the sample, even when comparing signals of the same order. For example, while all second-order signals may originate predominantly from collagen-rich regions, certain structures can exhibit a higher efficiency in SFG radiation than SHG. This occurs when the wavelength of the mixing signal lies in closer proximity to a real energy level of the medium, leading to resonant enhancement of the corresponding nonlinear susceptibility. Consequently, the intensity ratio between two second-order signals can be used to distinguish regions that would otherwise produce comparable SHG signals under standard harmonic imaging. An analogous situation holds for third-order effects, where an even larger variety of mixing signals is available.

More generally, the introduction of a second excitation field and the resulting nonlinear mixing processes enable the sampling of the spectral region of interest with a denser and more finely tunable set of generated frequencies. This expanded spectral coverage improves the access to resonantly enhanced spectral bands associated with different specific microenvironments within the sample. As a result, regions that differ in fine structural organization or local surroundings exhibit distinct resonance frequencies and therefore can be discriminated and probed more effectively. This strategy has already been demonstrated to be effective for probing blood oxygenation in live zebrafish, as the resonant frequencies of hemoglobin exhibit oxygenation-dependent variations according to whether the heme group is bound to molecular oxygen or not, which can be quantitatively resolved through different third-order SFG signals [22].

Another viable strategy for exploiting the newly generated mixing signals is to superimpose all acquisitions and, for each image pixel, construct a vec-

tor whose components correspond to the intensities of the different channels. These vectors reside in a space whose dimensionality equals the number of signals acquired; thus, the implementation of frequency mixing effectively enlarges the portion of signal space accessible to the system. This high-dimensional space can subsequently be explored using modern clustering algorithms or other automated classification techniques to identify distinct pixel classes and, ideally, enhance the selectivity of the system to fine variations inside the sample. However, for this approach to be practically applicable, all signals must be acquired simultaneously so that they can be meaningfully superimposed. The achievement of this condition may be challenging and is strongly dependent on the specific characteristics of the sample, as well as on the set of available optical filters.

Unfortunately, due to the limited time available for this work and the constraints imposed by the resources present in the laboratory, it was not possible at this stage to test the image analysis protocols just described. However, further testing and implementation of these methods are planned as part of the future development and optimization of the system.

Conclusions and Future Developments

In this master's thesis, after an extensive initial introduction to nonlinear optics with a particular focus on microscopy applications, the design and implementation of a frequency-mixing protocol on a multiphoton microscope was presented. To endow the existing microscope with the capability to generate and detect nonlinear frequency mixing signals, a delay line was designed and integrated into the optical setup, the two available excitation beams were spatially aligned and temporally synchronized, and a new detection module containing a tunable monochromator was developed and installed, allowing for the simultaneous acquisition of multiple spectral components. Subsequently, the upgraded system was first characterized and then tested on a variety of samples, and the corresponding experimental results reported.

The integration of the new frequency mixing protocol was successful, as the system is now capable of generating and detecting mixing signals in addition to conventional harmonic ones. However, a comprehensive analysis of the collected data for the samples tested could not be completed within the available time frame. Nonetheless, two possible analysis strategies are outlined in this thesis and are intended to be implemented and evaluated in the near future.

In addition to this, another potential future development of the system, aimed at further expanding the accessible parameter space, is the implementation of a protocol for polarization-resolved measurements. To achieve this, it will be necessary to install $\lambda/2$ and $\lambda/4$ waveplates before the objective, as well as a polarization analyzer placed after the sample and before the detectors. In this configuration, it will be possible to exert full control over the polarization state of the incident beams and to simultaneously detect the polarization state of the radiation emerging from the sample. Consequently, it will be possible to assess how different regions of the samples respond to and modify different incident polarizations.

The additional polarization-resolved information, processed using the same

analysis protocol proposed for the mixing signals, has the potential to increase the selectivity of the system even more by enabling the extraction of additional and detailed information on the optical properties of different regions within the sample. In fact, since parametric processes are coherent, the generated radiation is, in principle, expected to exhibit the same polarization as the excitation. However, subtle structural features within the sample can distort or alter the polarization state of the generated signals. Furthermore, the efficiency of nonlinear signal generation can be strongly polarization-dependent. For instance, second-order emission is typically enhanced when the polarization of the incident beam is aligned with the fiber structures that mediate the generation of new radiation components, whereas third-order processes, depending on the consider molecule, can exhibit an opposite behavior.

These further improvements to the system have already been designed and will be implemented and tested in the near future.

Bibliography

[1] R. W. Boyd, *Nonlinear Optics*, 4th ed. Academic Press, 2020, ISBN: 978-0-12-811002-7.

[2] X. Chen and P. J. Campagnola, "Shg microscopy and its comparison with thg, cars, and multiphoton excited fluorescence imaging," in *Second Harmonic Generation Imaging*, ser. Series in Cellular and Clinical Imaging, CRC Press, 2013, ch. 4, pp. 81–97, ISBN: 978-1-4398-4914-9.

[3] L. D. Landau and E. M. Lifshitz, *Electrodynamics of Continuous Media* (Course of Theoretical Physics), 1st ed. Pergamon Press, 1960, vol. 8, ISBN: 978-0-08-009105-1.

[4] L. Bonacina, P.-F. Brevet, M. Finazzi, and M. Celebrano, "Harmonic generation at the nanoscale," *Journal of Applied Physics*, vol. 127, no. 23, p. 230 901, 2020. DOI: 10.1063/5.0006093.

[5] D. A. Kleinman, A. Ashkin, and G. D. Boyd, "Second-harmonic generation of light by focused laser beams," *Phys. Rev.*, vol. 145, pp. 338–379, 1966. DOI: 10.1103/PhysRev.145.338.

[6] M. Gouy, "Sur une propriété nouvelle des ondes lumineuses," *Comptes Rendus de l'Académie des Sciences*, vol. 110, pp. 1251–1253, 1890.

[7] R. Hellwarth and P. Christensen, "Nonlinear optical microscopic examination of structure in polycrystalline znse," *Optics Communications*, vol. 12, no. 3, pp. 318–322, 1974. DOI: 10.1016/0030-4018(74)90024-8.

[8] Y. Guo et al., "Second-harmonic tomography of tissues," *Opt. Lett.*, vol. 22, no. 17, pp. 1323–1325, 1997. DOI: 10.1364/OL.22.001323.

[9] A. C. Millard, P. J. Campagnola, W. Mohler, A. Lewis, and L. M. Loew, "Second harmonic imaging microscopy," in *Biophotonics, Part B*, ser. Methods in Enzymology, vol. 361, Academic Press, 2003, pp. 47–69. DOI: 10.1016/S0076-6879(03)61005-0.

[10] R. Gauderon, P. B. Lukins, and C. J. R. Sheppard, "Three-dimensional second-harmonic generation imaging with femtosecond laser pulses," *Opt. Lett.*, vol. 23, no. 15, pp. 1209–1211, 1998. DOI: 10.1364/OL.23.001209.

[11] A. Aghigh, S. Bancelin, M. Rivard, M. Pinsard, H. Ibrahim, and F. Légaré, "Second harmonic generation microscopy: A powerful tool for bio-imaging," *Biophysical Reviews*, vol. 15, no. 1, pp. 43–70, 2023. DOI: 10.1007/s12551-022-01041-6.

[12] P. Campagnola and C.-Y. Dong, "Second harmonic generation microscopy: Principles and applications to disease diagnosis," *Laser & Photonics Reviews*, vol. 5, no. 1, pp. 13–26, 2011. DOI: 10.1002/lpor.200910024.

[13] J. A. Armstrong, N. Bloembergen, J. Ducuing, and P. S. Pershan, "Interactions between light waves in a nonlinear dielectric," *Phys. Rev.*, vol. 127, pp. 1918–1939, 1962. DOI: 10.1103/PhysRev.127.1918.

[14] N. Olivier, D. Débarre, and E. Beaurepaire, "Thg microscopy of cells and tissues: Contrast mechanisms and applications," in *Second Harmonic Generation Imaging*, ser. Series in Cellular and Clinical Imaging, CRC Press, 2013, ch. 3, pp. 51–80, ISBN: 978-1-4398-4914-9.

[15] S. Harris, "Tunable optical parametric oscillators," *Proceedings of the IEEE*, vol. 57, no. 12, pp. 2096–2113, 1969. DOI: 10.1109/PROC.1969.7495.

[16] J. Mertz, *Introduction to Optical Microscopy*, 2nd ed. Cambridge University Press, 2019, ISBN: 978-1-108-42830-9.

[17] J. A. Armstrong, "Measurement of picosecond laser pulse widths," *Applied Physics Letters*, vol. 10, no. 1, pp. 16–18, 1967. DOI: 10.1063/1.1754787.

[18] W. Denk, J. H. Strickler, and W. W. Webb, "Two-photon laser scanning fluorescence microscopy," *Science*, vol. 248, no. 4951, pp. 73–76, 1990. DOI: 10.1126/science.2321027.

[19] R. Fabbri, "Caratterizzazione di un tubo fotomoltiplicatore hamamatsu r760 utilizzato per il rivelatore plume nell'esperimento lhcb," Bachelor's thesis, Alma Mater Studiorum - Università di Bologna, 2023.

[20] A. Rogov, Y. Mugnier, and L. Bonacina, "Harmonic nanoparticles: Noncentrosymmetric metal oxides for nonlinear optics," *Journal of Optics*, vol. 17, no. 3, p. 033 001, 2015. DOI: 10.1088/2040-8978/17/3/033001.

[21] G. Campargue et al., "Multiorder nonlinear mixing in metal oxide nanoparticles," *Nano Letters*, vol. 20, no. 12, pp. 8725–8732, 2020. DOI: 10.1021/acs.nanolett.0c03559.

[22] J. Ferrer Ortas et al., "Label-free imaging of red blood cells and oxygenation with color third-order sum-frequency generation microscopy," *Light: Science & Applications*, vol. 12, no. 29, 2023. DOI: 10.1038/s41377-022-01064-4.